# TECHNICAL FEASIBILITY OF RECOVERING DEGRADED GTD 111 BLADES IN SERVICE THROUGH HEAT TREATMENT AND ADDITIVE MANUFACTURING

## Henry León Henao

# TECHNICAL FEASIBILITY OF RECOVERING GTD 111 BLADES DEGRADED IN SERVICE THROUGH HEAT TREATMENT AND ADDITIVE MANUFACTURING

**M.E. Henry León Henao**

In Partial Fulfillment of the Requirements for the Degree

Master of Mechanical Engineer


Advisor:

**M. Eng. Jorge Enrique Giraldo Barrada**

Department of Materials and Minerals

Co-Advisor:

**PhD. Alejandro Toro**

Department of Materials and Minerals


Research Groups:

*Grupo de Soldadura*
*Tribology and Surface Group* (GTS)

**Universidad Nacional de Colombia**
Facultad de Minas – Área Curricular de Ingeniería Mecánica
Medellin, Colombia

2022

# TABLE OF CONTENTS

# LIST OF TABLES

# LIST OF FIGURES

# Acronyms

Additive Manufacturing (AM)

American Society for Testing and Materials (ASTM)

American Welding Society (AWS)

Analysis of variance (ANOVA)

As-built (AB)

Body centered tetragonal (BCT)

Columnar dendrites (C.D)

Computer aided design (CAD)

Computer numerical control (CNC)

Design of experiment (DOE)

(DOE)

Directionally microstructure (DS)

Electrical Discharge Machining (EDM)

Electron Backscatter Diffraction (EBSD)

*Empresas Públicas de Medellín* (EPM)

Energy density (ED)

Energy Dispersive Spectroscopy (EDS)

Equiaxed (EQ)

Equiaxed dendrites (E.D)

Face centered cubic (FCC)

Face-entered cubic (FCC)

Gamma prime (γ')

Gas Tungsten Arc Welding (GTAW)

General Electric (GE)

Heated Affected Zone (HAZ)

Inverse pole figure (IPF)

Lack of fusion (LOF)

Laser Beam Welding (LBW)

Laser Powder Bed Fusion (L-PBF)

Laser Powder Directed Energized Deposition (LP-DED)

Optical Emission Spectroscopy (OES)

Optical Microscope (OM)

Particle Size Distribution (PSD)

Post-weld treatment (PWHT)

primary dendrite arm spacing (PDAS)

Scanning Electron Microscope (SEM)

secondary dendrite arm spacing (SDAS)

Stainless Steel (SS)

The Ohio State University (OSU)

Topologically Closed Packed (TCP)

Tribology and Surfaces Group (GTS)

## ABSTRACT

Repair components of the hot gas path is crucial for economic reasons in gas turbine engines. In this work, a characterization of deposits applied by Laser Powder Bed Fusion (L-PBF) and Laser Powder Directed Energized Deposition (LP-DED) on a 1st stage blade made of GTD 111 DS superalloy were carried out. The 1st stage blades are damaged in operation due to collision of external objects, development of thermal fatigue cracks and high-temperature erosion, which drastically reduces their lifetime. The process parameters for L-DED and L-PBF were established as a function of the integrity and geometry of the deposits. René 65 powder was used for both processes without preheating. Visual inspection and macro etching were used to evaluate the weld metal deposits soundness. Optical microscopy and scanning electron microscopy were used to examine the microstructure of the deposited layers in the cross-section and EBSD allowed studying the crystallographic texture. Compared to conventional processes, L-PBF and LP-DED provide crack-free deposits and better control of shape and dimensions, reducing machining time. In particular, the L-PBF process has greater precision, which makes it ideal for replicating the blade's cooling holes. The study demonstrates the feasibility to restore dimensions of a tip blades and illustrates the significant potential of Additive Manufacturing (AM) utilizing powders of high γ' avoiding hot cracking.

**KEY WORDS:** Additive Manufacturing, GTD 111, L-PBF, L-DED, Gas turbine

# FACTIBILIDAD TÉCNICA EN LA REPARACIÓN DE ÁLABES DE GTD 111 DEGRADADOS MEDIANTE TRATAMIENTO TÉRMICO Y MANUFACTURA ADITIVA

La reparación de los componentes de la ruta del gas caliente es crucial por razones económicas en las turbinas a gas. En este trabajo se realizó una caracterización de los depósitos aplicados por *Laser Powder Bed Fusion* (L-PBF) y *Laser Powder Directed Energized Deposition* (LP-DED) sobre un álabe de primera etapa fabricado con la superaleación GTD 111 DS. Al deteriorarse en funcionamiento debido a la colisión de objetos externos, el crecimiento de grietas por fatiga térmica y la erosión por alta temperatura, se reduce drásticamente su vida útil. Los parámetros del proceso para L-DED y L-PBF se establecieron en función de la integridad y la geometría de los depósitos. Para ambos procesos se utilizó polvo René 65 sin precalentamiento. Se utilizó inspección visual y análisis metalográfico para evaluar la solidez de los depósitos de manufactura aditiva. Se usó microscopía óptica y microscopía electrónica de barrido para examinar la microestructura de las capas depositadas en la sección transversal y el análisis de EBSD permitió estudiar la textura cristalográfica. En comparación con los procesos convencionales, L-PBF y LP-DED proporcionan depósitos sin grietas y un mejor control de la forma y las dimensiones, lo que reduce el tiempo de mecanizado. En particular, el proceso L-PBF tiene una mayor precisión, lo que lo hace ideal para replicar los orificios de enfriamiento de la hoja. El estudio demuestra la viabilidad de restaurar las dimensiones de los álabes en el borde chirriante e ilustra el importante potencial de la fabricación aditiva (FA) que utiliza polvos de alto contenido de γ' evitando el agrietamiento en caliente.

**PALABRAS CLAVES:** Manufactura Aditiva, álabes GTD 111, L-PBF, L-DED y turbinas a gas.

# CHAPTER 1: INTRODUCTION

Great economic interests have had power electrical companies during several decades to restore damaged components of gas turbine to reduce maintenance costs (Wilson, 2014) (Clader, 2006). Nickel base superalloys are selected mainly for hot path gases due to great properties such as corrosion, creep and tensile at elevated temperatures. In particular, blades are the most critical part due to high pressure and temperature operations, additionally often suffer the impact to foreign object and wear against vane that lead in surface damages and cracks developing a reduce in the lifetime.

The use of nickel alloys and complex geometry to manufacture makes the blade especially expensive. The cost of substitution a turbine blade is truly pricey, generally more than $15000 for a first stage gas turbine blade (Chen, 2008). Remanufacturing worn blades consumes a fraction of material, energy and time of the total replace cost (Jones, 2005) being an emerging market from industry and research communities (Yilmaz, 2010) (Unal-Saewe, 2020) (Keshavarz, 2021).

In the past, different welding processes have been carried out for turbine blade damage repair such as plasma welding (Saltzman, 1992), Gas Tungsten Arc Welding (GTAW) and brazing applied manually been a tedious operation and involved high skills from the operator. Even if the operation is performed in the most correct way, metallurgical and mechanical properties are inferior due the selection of a dissimilar alloy for the filler metal that facilitate application (with more ductility). However, some studies related to Laser Beam Welding (LBW) were found in 90´s but it was not a continuous practice (Ross, 1992), (Gandini, 1997). Due to high heat input several cracks occurred therefore, a typical solution for those techniques is to preheat and then repair with welding processes.

In the recent years, processes for additive manufacturing (AM) have improved its technology, cost and maintenance (DeBroy, 2017). This fact has driven the use for repairs in areas such as automotive, energy, medical and aerospace. AM build three-dimensional (3D) components stacked layers of materials. It is a rapid deposition guided by a digital model which permit manufacture complex or customized components eliminating the use of expensive tooling used in conventional processes. The AM of alloys was originated based on the existing knowledge in metal powder technology, high-energy beam welding, cladding and prototyping (DeBroy, 2017). Interesting metallurgy features creating an emerging possibility in turbine repair, increasing service life reducing repair cost and the carbon footprint of its components. This research will focus on two processes: Laser-Powder Bed Fusion (PBF) and Laser-Directed Energy Deposition (DED) which use laser such as energy source and can achieve deposit with low heat input, distortion, good roughness and almost without the need to do a huge post-machining.

Colombian thermoelectric generation industry represents 30.7% of the total national integrated system, producing about 47,735 MW (Acolgen, 2021). The central component of a thermoelectric plant is the turbine (see Figure 1), which has multiple mechanical elements capable of withstanding the demanding operating conditions such as high temperatures (~ 1000 ° C), corrosion, pressure (~ 130 psi), gas outlet of 2.5 Mach and a rotation speed of

3600 rpm. Gas turbines convert the heat produced in the combustion process into mechanical energy and, later, into electrical energy through the Brayton cycle (GE, 2010). This process is made up of the compression, combustion and expansion stages. In expansion stage there are three sub-stages, each one with a set of 92 blades manufactured in nickel-based alloy. This research is focused on the GTD 111 alloy used in the first stage.
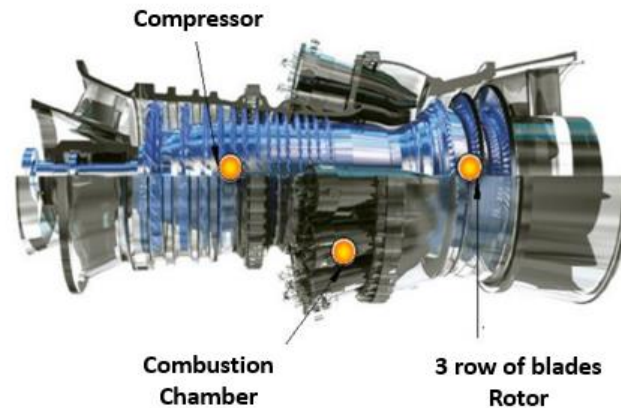


Figure 1. Representative zones of a gas turbine GE7FA (General Electric Company, 2010)

When turbine components are damaged by corrosion / oxidation or cracking due to service conditions, they must be repaired and this typically requires the use of thermal processes that deposit metal to restore nominal dimensions. Some of the typical defects presenting in degraded blades are showing in Figure 2. The most susceptible regions are the contact surfaces that are exposed to centrifugal loading and oscillatory vibrations causing erosive wear. Additionally, the corrosive environment is severely crucial to form oxidation, corrosion and sulphidation that tends to crack and spall. The main wear mechanism on the turbine blades is fretting wear (Pauzi, 2016)

The integrity of joining components depends on the absence of cracks and / or fissures. Therefore, both the initial manufacture and any repair must be done with procedures that guarantee defects free. The disadvantage of Ni alloys is that they present serious weldability problems, some of them are: solidification cracking, constitutional liquation and strain-age cracking.

In particular, the *Termoeléctrica de La Sierra* in *Puerto Nare*, Antioquia is owned by *Empresas Públicas de Medellín* (EPM) and use 7FA gas turbine. They carry out corrective maintenance of Ni components in specialized companies abroad, which have the knowledge and infrastructure required to carry out repair processes. They restore dimension through GTAW manually. This is expensive and delayed due to logistics issues (export, import, and long maintenance times). Current strategy of EPM is to carry out repairs to thermoelectric turbine components in its workshops and they have a research project underway with the Tribology and Surfaces Group (GTS) of the *Universidad Nacional de Colombia* to achieve this goal.

Figure 2. Some typical defects in degraded blades

Nevertheless, the repair of Ni alloys first requires a conditioning of the parts involved. The blades suffer a microstructural degradation due to the working conditions that must be restored by a solution heat treatment before repairing by AM, which favors the microstructural similarity of the molten metal to the base metal. In the case of nickel-based alloy, the most relevant properties of the microstructure are the grain structure such as size, orientation and the characteristics of strengthening phase (distribution, size and area fraction). On the other hand the existence of defects such as cracks or discontinuities (pores or lack of fusion) could highly reduce mechanical properties. High angles between deposited layer could produce stray grains that imply a peak of thermal stresses that produce hot cracks. Thus, there are several challenges to face in the repair of degraded blades of GTD 111.

This thesis seeks to explore the dimensional restitution of nickel-based alloy parts at the local level and have in-depth knowledge of their metallurgy, which eventually will allow repairs of critical components through thermal processes. Therefore, the aim of this research is to determine the feasibility to repair non-weldable nickel alloys after service period with crack-free. Blown powder L-DED and L-PBF processes will be used to deposit the Ni alloy onto GTD 111 substrate without preheat. Microstructure characterization is carried out using Optical Microscope (OM), Scanning Electron Microscope (SEM), microhardness and Electron Backscatter Diffraction (EBDS).

# CHAPTER 2: THEORETICAL BACKGROUND

## 2.1 Nickel-based alloys

Nickel-based alloys are characterized by having a high percentage of nickel in their composition and the ability to dilute a high amount of elements. With the appropriate addition of compositional elements, these materials are endowed with excellent properties such as resistance to corrosion, oxidation, creep, among others, which make nickel-based alloys one of the most important classes of engineering materials, having applicability in the areas of power generation, petrochemicals, chemical processing and aerospace (Davis, 2000).

As there is no systematic classification system for these types of alloys, they are generally classified by their chemical composition. Figure 3 shows the four categories into which nickel-based alloys are divided and their corresponding classes. Other way to be known is by the commercial name of their manufactures (DuPont, 2009).
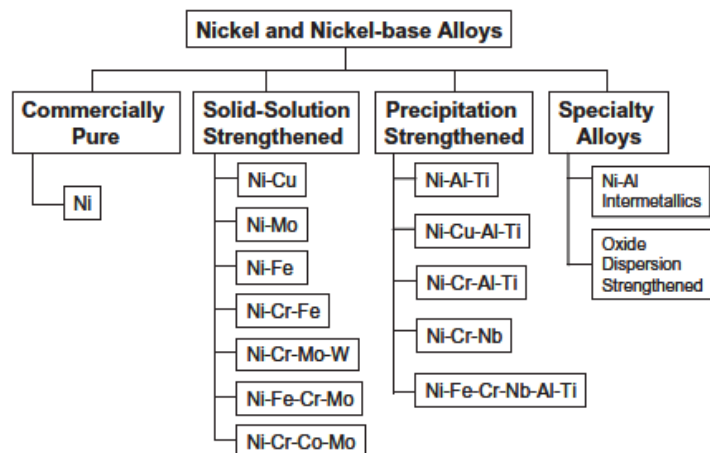
Figure 3. Classification of nickel alloys (DuPont, 2009)

The first category is the pure metal which contains >99% of Ni, it is composed of two families of alloys 200 and 201. In general terms, it is used in caustic environments and possesses low strength and hardness.  On the other hand, the second category is the solid solution hardening alloys which occurs when one or more elements are added to the nickel matrix to form a homogeneous composition. Generally, they contain a variety of substitution elements such as Cr, Fe, Mo, Cu, and W. These types of materials can be work hardened and are often used in applications where a combination of moderate mechanical strength and excellent corrosion resistance are desired (DuPont, 2009). The maximum values of tensile strength in these alloys reach 120 ksi (830 MPa) and for yield strength are in the range of 50-70 ksi (345-480 MPa). If higher levels of mechanical strength are required, precipitation hardened alloys should be chosen. Solid solution hardened alloys can be categorized according to their chemical composition as shown in Figure 3. These added elements produce an expansion in the Ni matrix, causing a hardening of the austenitic matrix (DuPont, 2009).

Precipitation or aging hardened alloys contain Ti, Al and/or Nb which form precipitates coherent with the Ni matrix. The precipitates that are formed are called gamma prime (γ'), which are compounds of the type [$Ni_3Al$, $Ni_3Ti$ and $Ni_3(Ti, Al)$] and the double gamma prime (γ''), which are of the type ($Ni_3Nb$). With the appropriate combination of thermal cycles, these alloys can reach ultimate tensile strength values that exceed 200 ksi (1380 MPa) and yield strength greater than 150 ksi (1035 MPa) (DuPont, 2009).

They are known as superalloys, due to their excellent mechanical properties and resistance to corrosion at high temperatures. This term has been extended to other alloys, but it is mainly used for materials that are hardened by gamma-prime and double-prime precipitates (DuPont, 2009).

Specialty alloys have impressive creep strength, oxidation resistance at high temperature due to the precipitation hardening and fine dispersion hardening particles. They do not maintain their properties after conventional fusion welding techniques due high hardness, low ductility and melting range in their phases (DuPont, 2009).

## 2.1.1 Alloying elements

The physical metallurgy of these Ni alloys is complex due to their chemical composition, in which an intentional mixture of chemical elements predominates. Nickel-base alloys have a face-centered cubic (FCC) matrix or γ matrix. Some elements have the function of hardening by solid solution: Cr, Co, Fe, Mo, W and Ta; and others by precipitation: Ti, Al and Nb; Cr, Al and Ta favor resistance to oxidation; Cr, La, and Th improve resistance to hot corrosion and B, Mo and W increase creep strength due to their low diffusivity in the matrix.

In Table 1 the general effect of various alloying elements in Ni base alloys is summarized. In general terms, elements with similar atomic radio, crystal and electronic structure relative to Ni are most likely to remain in solid solution.

Table 1. The effect of some alloying elements in Ni-base alloys (ASM International, 1982)

| Effect | Element |
|---|---|
| Solid solution Strengthener | Co, Cr, Fe, Mo, W, Ta |
| γ' $Ni_3(Ti, Al)$ Former | Al, Ti |
| Solid solution Strengthener of γ' | Cr, Mo, Ti, Si, Nb |
| γ''-$Ni_3Nb$ Former | Nb |
| Carbide Formers: | |
| MC and M(C,N) | W, Ta, Ti, Mo, Nb |
| $M_7C_3$ | Cr |
| $M_{23}C_6$ | Cr, Mo, W |
| $M_6C$ | Mo, W |
| TCP Phase (σ, P, μ, Laves) | Ti, V, Zr, Nb, Ta, Al, Si |

| Surface Oxide ($Cr_2O_3$/$Al_2O_3$) Former | Cr, Al |
| --- | --- |

On the other hand, Al and Ti improve strength by precipitation of the Ý´- $Ni_3$(Ti, Al) phase with low coarsening rates due to the good crystallographic matching between Ý and Ý´ in superalloys (Lifshitz, 1961). Increasing yield strength when temperature is up to 800°C (Thornton, 1970). Nb is a γ''-former of $Ni_3$(Nb) a body centered tetragonal (BCT) phase with high coherency in the matrix developing great mechanical properties to many commercial alloys. Although is a metastable phase that transforms with long exposure time at elevated temperatures in orthorhombic δ phase with $Ni_3$(Nb). δ is a detrimental phase due to its incoherence with the Ni matrix (DuPont, 2009).

Some elements that are added to give beneficial effects in many Ni-base alloys could combine with carbon to form various types of carbides. MC-type carbide has an FCC crystal structure and it is formed at the end of the solidification by eutectic-type reactions with the matrix locating along the interdendritic and grain boundary regions (DuPont, 1988). M (CN) carbonitrides are promoted by the segregation of C, N to the liquid during solidification. MC could be replaced during thermal processing or service conditions by $M_{23}C_6$ and $M_6C$. The main element of $M_{23}C_6$ is Cr that is developing at 760-980°C forming on grain boundaries if these are discrete carbides they could restrict grain boundary sliding improving creep strength (DuPont, 2009).

The $M_6C$ is formed when the amount of Mo and W is greater than 6-8 atomic percent in the range from 815-980°C. Topologically Closed Packed (TCP) phases such as σ, P, μ and Laves can be developed in alloys with high amount of elements by long terms at elevate temperatures forming complex crystal structures. It has low strength and can propitiate a failure (DuPont, 2009).

The metallurgy of welding is closely linked to the physical metallurgy of materials. Therefore, elements added with a beneficial purpose can lead the formation of eutectic constituents and secondary phases during solidification (DuPont, 2009). These phases can cause different types of cracking such as solidification, liquation of grain boundaries and aging deformation (Pollock, 2006). The relationship between the chemical composition of the alloys and the susceptibility to cracking is shown in Figure 4. The materials belonging to the "Non-weldable" category are the most difficult to carry out their manufacture, the "difficult to weld" category are susceptible to cracking in the Heated Affected Zone (HAZ). Alloys that are classified as "moderately-weldable" offer difficulties in post-weld treatment (PWHT) operations.
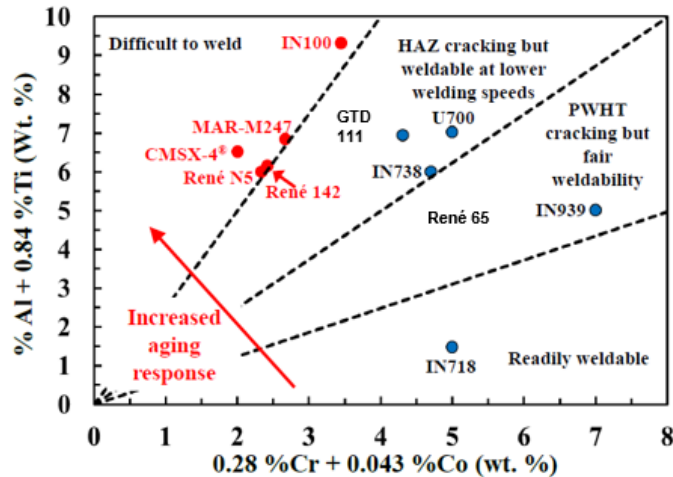
Figure 4. Chart for weldability prediction of Ni-based superalloy (Pollock, 2006).

On the other hand, there are some detrimental elements and phases to degrade mechanical properties of nickel-base superalloys. Sulphur is one of the most detrimental elements promoting segregation to the grain boundaries forming a low melting-point eutectic which initiates a crack propagation route. Other elements that affect the material in the same manner are Si, P, Pb, Bi, Te, Se and Ag.

## 2.1.2 Microstructure

The physical metallurgy of the precipitation-strengthened Nickel-based superalloys consists mainly of two-phase system: the γ matrix is the austenitic phase of Ni with a face-centered cubic (FCC) crystallographic structure which contains the other alloying elements. The most important phase is an intermetallic precipitate known as gamma prime (γ') that is formed by the addition of Al and Ti. It is a highly ordered $L1_2$ structure whose composition is $Ni_3(Al,Ti)$, also a FCC structure. The crystal structure of both γ and γ' phases are shown in Figure 5. It can be seen that the upper and lower planes consist of a Ni atom surrounded by Al or Ti atoms at each corner of the square. This pattern is extended in all directions in an ordered plane of Ni and Ti atoms.

Other alloys that are not considered in this research can also be strengthened by the formation of gamma-double prime γ'' which is of stoichiometry $Ni_3NB$. Morphology of the precipitate phase can vary from cubic, cuboidal, spherical and amorphous shape. Initially depends on the elemental content of aluminum and titanium and its heat service. Cubic γ' often appear in alloys with higher Al than Ti, spherical γ' appears with higher content of Ti than Al. It is also possible to obtain systems containing a dual morphology such as a primary cuboidal γ' surrounded by finer, secondary γ' which are typically spheroidal (Johnson, 1966).
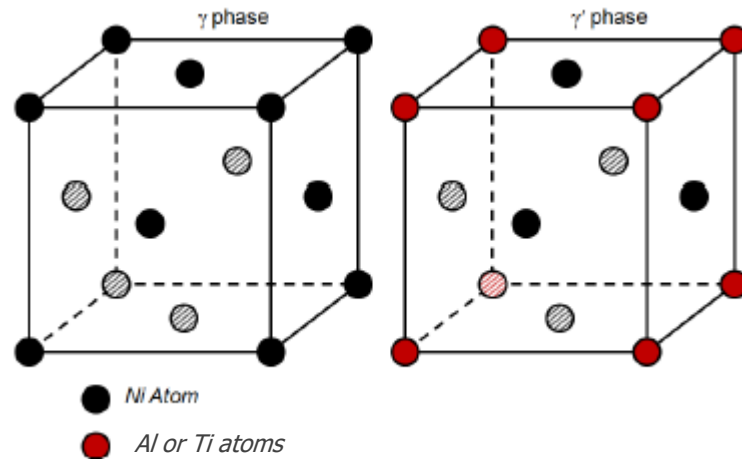
Figure 5. Diagram of γ and γ' FCC structure (Donachie, 2002)

On the other hand, carbon has affinity to formation of carbides with many elements such as Cr, Co, Mo, Ti, W and Zr resulting in MC, $M_{23}C_6$ or $M_6C$ (where M is representative of a metallic element). Almost all of them form at or along grain boundaries and are considered grain boundary strengtheners when are properly formed. Carbides form at high temperature in the form of MC carbides, $M_{23}C_6$ and $M_6C$ being formed at lower temperature under aging or in service conditions (Donachie, 2002).

Sims stablished that the larger MC carbides which break down into "blocky" $M_{23}C_6$ carbides at the grain boundaries, improve material properties by inhibiting sliding following the next reaction:

$$\gamma + MC \rightarrow M_{23}C_6 + \gamma' \text{ (Sims, 1966)}$$
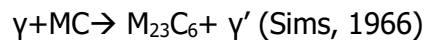
Figure 6a shows how the carbide typically surrounded the grain boundaries and Figure 6b represents a micrograph showing the carbide formations of MC and $M_{23}C_6$ (Bor, 2000). However, $M_{23}C_6$ can be a nucleation site when the material fails (Sims, 1966) (Engler-Pinto, 1996)



A) Diagram of grain boundary carbide structure (Sims, 1966)

B) Micrograph of typical carbides structure (Bor, 2000)

Figure 6. Carbide structure

There are some detrimental phases promoted from the addition of the minor beneficial elements such as μ phase, rhombohedral structure; laves phases, hexagonal structure and formed after long periods at high temperature and σ phase, tetragonal structure formed after extended exposure between 540° C and 980° C (Donachie, 2002).

## 2.2 GTD 111 DS

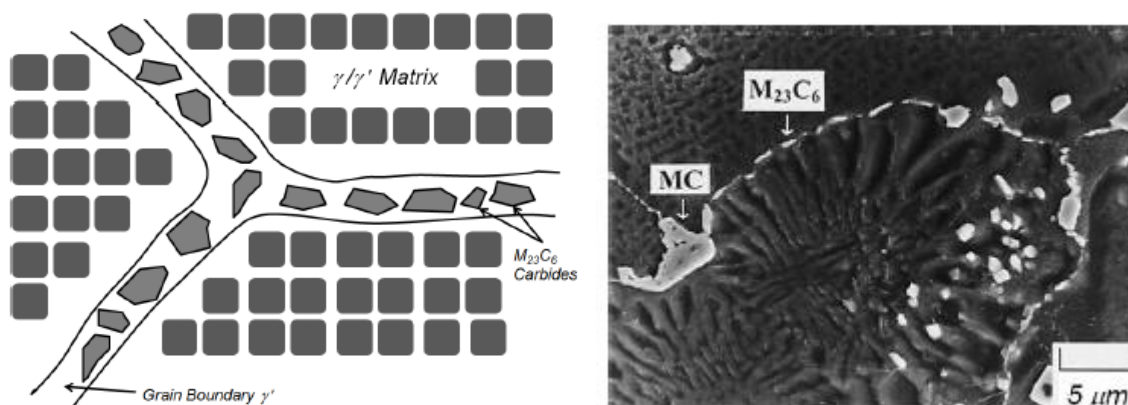The superalloy GTD 111 DS is a precipitation hardenable alloy that was developed in 1987 as a first stage bucket material derived from René 80 (Li, 2006). It is commonly used in gas turbine applications (Schilke, 2004). General Electric uses the material on the first stage in MS7F/MS9F, MS3002 and MS5002C units (Schilke, 1992). Chemical composition in weight percent of GTD 111 is shown in Table 2 (Daleo, 1998). Its relevant the high amount of Ti+Al that promote the gamma prime precipitate and the cracking susceptibilty in welding processes.

Table 2. Chemical composition of GTD 111 (%wt) (Daleo, 1998)

| Ni | Cr | Co | Ti | W | Al | Ta | Mo | C | B |
|----|------|------|---------|---------|---------|---------|---------|------|------|
| Bal. | 13.7-14.3 | 9-10 | 4.7-5.1 | 3.5-4.1 | 2.8-3.2 | 2.5-3.1 | 1.3-1.7 | 0.12 | 0.02 |

The particular microstructure has been found to produce enhanced creep life, impact strength, corrosion and thermal fatigue resistance compared to equiaxed components (Daleo, 1998) (Viswanathan, 1998) (Sajjadi, 2001). GTD 111 has multiple phases, the primary γ' cuboids are produced during solidification under 1200°C and the secondary γ' spheroids are produced during aging heat treatment after partial solution (Sajjadi, 2001). The γ-γ' eutectics are promoted in the last stages of solidification and are located at dendrite boundaries and near to pores (Daleo, 1998). The lifetime of a first stage blade is approximately 70 000 hours of service.

Figure 7 shows a 3D microstructural reconstruction (Villada, 2019), along the Z direction displays a dendritic growth with a typical directional solidification (DS) according to (Davis, 1997). The dendrite grows in the <001> producing columnar crystals, improving the creep and fatigue resistance compared with the equiaxed structure.
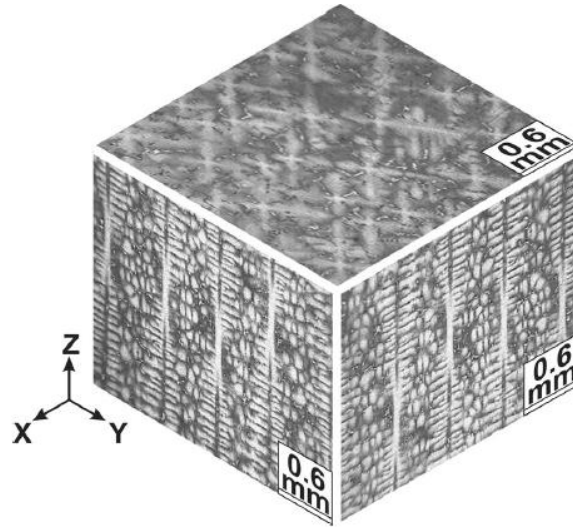
Figure 7. 3D microstructural reconstruction GTD 111 (Villada, 2019)

The turbine blades are typically fabricated using investment casting, and depending on the casting complexity, they generally display one of the three common microstructures shown in the Figure 8 (i.e., equiaxed or polycrystalline, directionally solidified, and single crystal). Figure 8a shows a polycrystalline or equiaxed (EQ) microstructure that are prone to failure due grain boundaries that are transverse to the loading direction reducing creep strength (Donachie, 2002). To obtain a stronger microstructure directionally solidified (DS) was implemented to avoid the transverse grain boundaries and oriented grain structure to the major axis improving its mechanical properties (Figure 8b). Single-crystal (SX) blades (Figure 8c) have a microstructure that contains no grain boundaries and removal the percent of C and B omitting the reduce of melting temperature and the fatigue life in those alloys. Its cost of manufacture is higher than the others (Tien, 2012).



Figure 8.  Different forms of manufacturing blades (Roll-Royce, 1996)

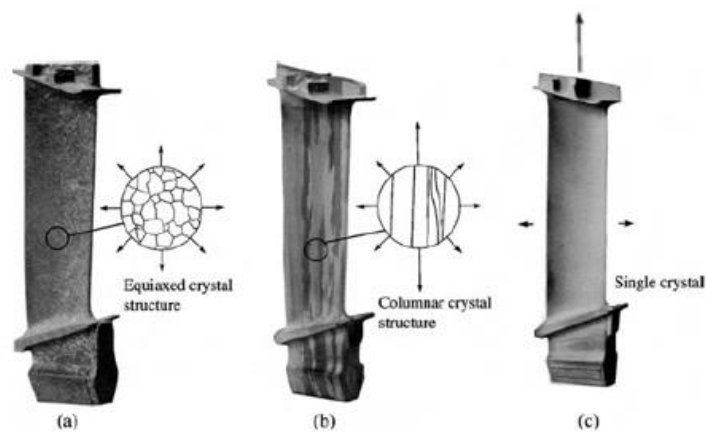Blades manufacturing method of GTD 111 is a controlled casting, see Figure 9, that use an induction heating that provides a homogenous thermal gradient in advance of the liquid-solid interface (Smallman, 1999). A cold mold extracts the heat forming a columnar-grained structure in Z direction. The long grains reduce the Young´s modulus in <001> increasing elastic strain and reducing thermal stresses. This characteristic enhance strength, ductility and the time before rupture compared to equiaxial GTD 111 (Stewart, 2009).
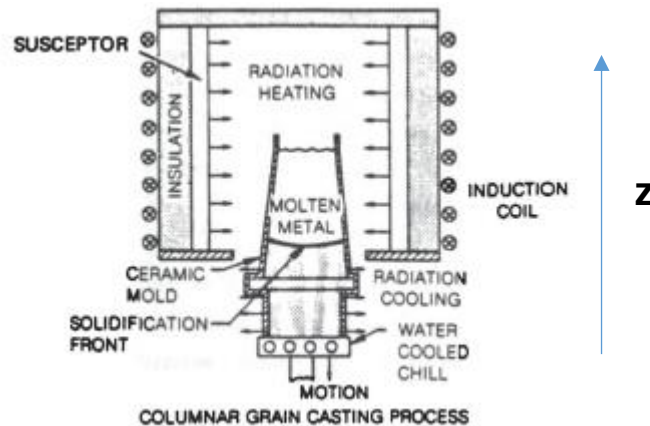


Figure 9. Manufacture method directional solidification (Smallman, 1999)

Since superalloys are hardenable by aging, the parameters of the heat treatments affect the distribution of the constitutional elements, and the distribution and morphology of the precipitates. The heat treatment consists of two stages: dissolution and aging.

The dissolution causes a homogenization of the alloying elements in the microstructure, in addition to decrease some precipitates (Svensson, 1981). If the dissolution is carried out at 1200 °C it is known as complete dissolution or homogenization. This treatment can have negative effects such as local fusion of eutectic components and the reduction of the percent of γ', which leads to changes in the mechanical properties of the blades. To avoid this, there is another possibility called partial dissolution (1120 °C), in which a lower temperature is used in order to prevent the formation of harmful phases such as etta, tao or Laves (Sajjadi, 2003).

The aging treatment in Nickel-based superalloys is applied to generate nucleation and growth of precipitates. Balikci proposes two growth mechanisms of γ': coalescence of small particles to larger ones or by the extraction of dissolved elements such as Al and Ti of the saturated solid solution matrix, in addition to the precipitates (Balikci, 1993). Over-aging causes an increase in the size of the particles. Therefore, a reduction in the number of particles and a greater spacing between them. Resulting in a decrease in yield strength in Nickel superalloys. Long term aging could be emulated by the service conditions. The Y´coarsening and microstructural transformation occurred having detrimental effect in mechanical properties (Donachie, 2002).
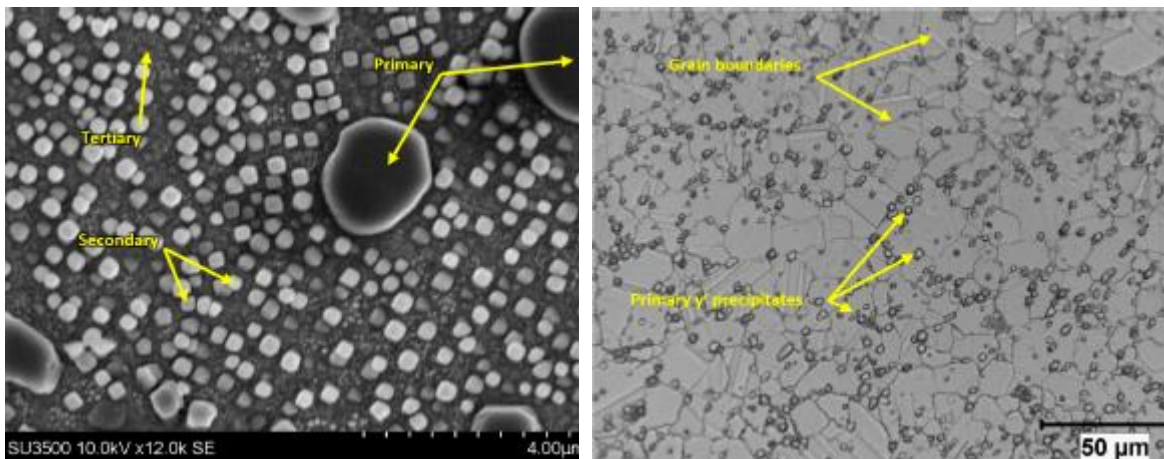
## 2.3 René 65

René 65 is a precipitation hardenable nickel superalloy strengthened by gamma prime with around 40% area fraction (Hardy, 2020). Chemical composition is derivate of the powder metallurgy superalloy Rene 88 DT, and this alloy has been recently introduced into service in turbine engines by General Electric (GE) Aviation, the composition is shown below (Table 3) (Groh, 2014).

Table 3. Chemical composition René 65 (Groh, 2014)

| Ni | Al | B | Co | Cr | Fe | Mo | Nb | Ti | W | Zr |
|------|-----|-------|----|----|----|----|-----|-----|---|------|
| Bal. | 2.1 | 0.016 | 13 | 16 | 1 | 4 | 0.7 | 3.7 | 4 | 0.05 |

René 65 has great mechanical properties, similar to cast alloys used for gas turbine blades (Heaney, 2014). The microstructure is mainly formed of a Ni matrix γ and $Ni_3$(Al,Ti) γ' precipitates. There are present three different sizes of gamma prime, primary, secondary and tertiary, as can be seen from Figure 10A. The primary precipitates are located at the grain boundaries (Figure 10B) preventing grain coarsening while other precipitates are along the matrix such as strengthening agents (Olufayo, 2019).



A) Scanning electron microscopy (SEM) image showing different γ'   B) Optical image of γ' along boundaries

Figure 10. Microstructures of René 65 (Olufayo, 2019)

The extensive use of additive manufacturing (AM) in the aerospace and power energy industry has motivated the development of some research in mechanical properties such as tensile properties, creep behavior, low-cycle fatigue performance, that have shown this alloy as a capable material for AM for turbine components applications analogous to the cast and wrought versions of this alloys (Heaney, 2014) (Wessman, 2016) (Gorelik, 2017) (Wessman, 2020).

In this studio, Rene 65 is used in powder format obtained from gas atomization process. It has a particle size distribution (PSD) around 15-45 μm. It is noteworthy that this type of fine

particles is normally used in AM processes of L-PBF due to high resolution and works with lower powder levels. In contrast, in LP-DED higher particles sizes are used providing better productivity.

## 2.4 Solidification Modes

The different morphological forms that can occur in metals solidification are called solidification modes and are illustrated in Figure 11. The combination of temperature gradient ($G_L$) and solidification growth rate (R) influences solidification mode. A high $G_L$ combined with a low R produce a planar growth mode. As R increases, the solidification mode shifts to cellular and then dendritic. When $G_L$ is significantly low equiaxed dendritic growth is possible. A high combination of $G_L$R develops finer structure. Planar mode is not stable in practice, and the two most common solidification modes are the cellular and cellular/columnar dendritic modes (Lippold, 2014).
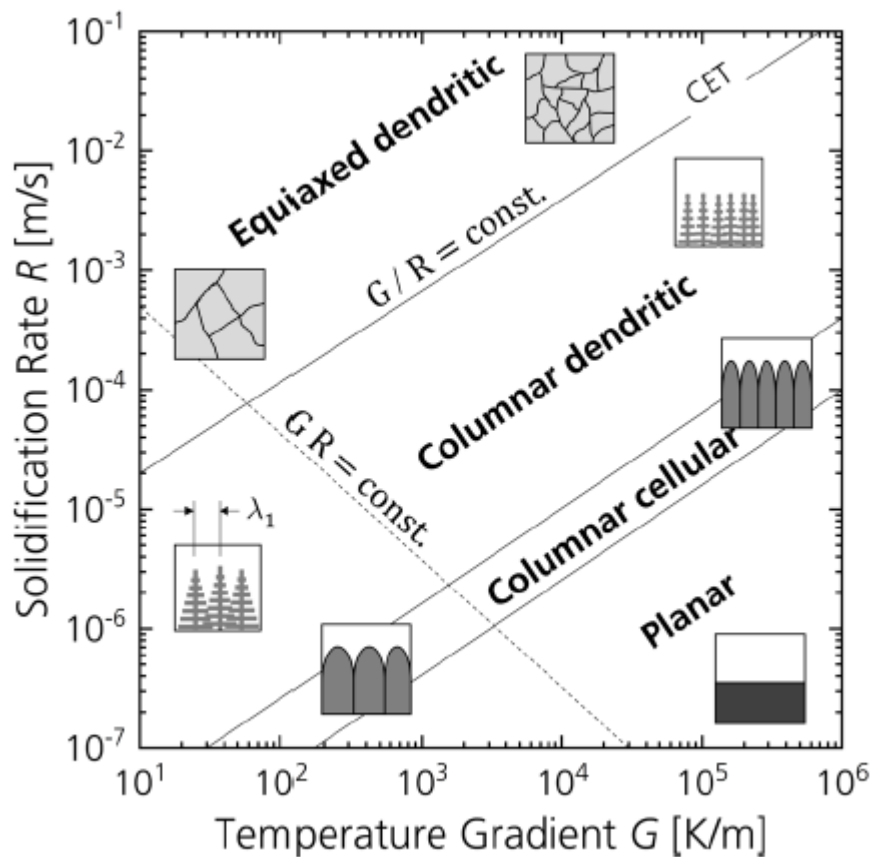


Figure 11. Solidification modes. Temperature gradient (GL) VS Solidification rate (R). (Sindo Kou, 2009).

Composition also has an effect on solidification mode. Most alloys will solidify in dendritic or cellular modes. Cooling rate has a significant influence on the size of the solidification structure, varying the distance between the axial centers of the dendrites. The primary dendrite arm spacing (PDAS) and secondary dendrite arm spacing (SDAS) are often used to

define the solidification substructure size. In large castings PDAS can be several millimeters and in laser processes few microns (Lippold, 2014).


## 2.5 Weldability of Superalloys


The metallurgical characteristics that affect the weldability of non-ferrous alloys at high temperatures basically consist of the precipitates used to increase the strength of the alloy (γ' and γ") and those associated with solidification and segregation, such as carbides and Laves phases. The first tends to cause reheating cracking problems, while the carbides and Laves phase can create liquidation cracks in the HAZ, as they have lower melting points (Thompson, 2005).

Solidification cracking:

As in other systems, these cracks form in the final stages of solidification, when liquid films are distributed along the grain boundaries and, in some cases, at interdendritic sites. At this stage, the shrinkage of the already solidified regions generates tensile stresses, and if the liquid distributed in the boundaries forms a continuous film, the stresses will not be able to be accommodated and the grain boundaries will separate to form a crack.

According to Henderson et al. (2004), the solidification crack occurs in the newly formed bead, when there is still a liquid-solid biphasic region exposed to stresses and the high solid fraction (usually above 90%) restricts the flow of liquid metal to the interdendritic regions. Due to the stresses present caused by welding, separation occurs in these regions.

Alloys with wide solidification intervals and with the presence of impurities are more susceptible to the occurrence of this defect. Henderson also mentions that low welding speeds promote the formation of this type of crack, since it generates higher stresses in the weld bead. However, the same mentions that, for thin sheets, a common defect associated with solidification cracking is the formation of a continuous grain boundary that **forms along the center of the weld bead** when using intermediate to high heat input processes. and with high welding speeds.

Reheat Crack:

This type of crack normally occurs in alloys with γ'-phase precipitation, Ni3(Al, Ti), during post-weld treatment or even during high-temperature service, due to the presence of residual stresses or the loading exerted during operation. This defect is characterized by the presence of intergranular microcracks both in the HAZ and in the weld, which form as a result of precipitation and hardening of the alloy during high temperatures, combined with the solidification stresses that act on the grain boundaries. These cracks usually start in carbides present at the grain boundaries, which act as stress concentrators (Henderson et al, 2004).

The occurrence of this type of crack is directly related to the Al and Ti contents in the alloy, which are responsible for the precipitation of the γ' phase, in addition to elements such as carbon, sulfur and boron. In this way, the weldability of nickel alloys and the susceptibility to reheating cracks can be qualitatively evaluated as a function of the amounts of Al and Ti.

According to DuPont (2009), reheating cracks occur during heating up to the solubilization temperature due to the simultaneous presence of precipitation and stresses applied to the grain boundaries. They usually occur in the HAZ and are intergranular, and in some cases, they reach the partially melted zone. The material stresses can come from welding, from differences between the coefficients of thermal expansion between the base metal and the filler metal, or even due to dimensional variations caused by the precipitation.

<u>Liquation cracking:</u>

Liquation cracking is associated with the formation of liquid films along the grain boundaries, in the partially melted zone and in the HAZ (Dupont, 2009). Thompson (2005) mentions that phases that form during solidification, such as MC carbides and Laves phase, have the potential to initiate melting at the grain boundaries. When this melting is accompanied by sufficient thermal stresses, cracks can form along the grain boundaries of the HAZ and extend into the melt zone.

Metallurgically, liquation cracking occurs when an alloy containing a second phase susceptible to the phenomenon is heated at a certain rate that the second phase cannot dissolve before the alloy reaches a solidus system, causing its melting, which will invariably occur at the interface. The molten liquid may spread along the grain boundaries if its solute is also soluble in the matrix, or if there are enough impurities to cause wettability (Thompson, 2005).

Alloying elements and the presence of impurities, such as sulfur, phosphorus, boron and lead (Thompson, 2005), significantly influence the formation of liquidation cracks, which can change the liquation mechanism (formation and composition of liquid films), the degree of of liquation (amount of liquid formed), the temperature range in which the liquid film occurs and its distribution (wetting). The grain size also influences this phenomenon, which is reduced in the presence of refined grains (Dupont, 2009).

## 2.6 Additive Manufacturing (AM)

Additive manufacturing (AM), also known as 3D printing, is an emerging technology that has revolutionized manufacturing in the last years. By using the addition of metals and not subtraction, it is possible to manufacture parts with complex geometries. The use of AM is diverse such as built a new component, repair, remanufacturing, and property improvement of existing objects.

AM is a process that uses a heat source (laser, electron beam, electric arc or ultrasonic energy) and feedstock (powder, wire or thin sheet) to produce a physical object form, using a computer aided design (CAD) model that fully describes the geometry. The CAD is sliced into several equal layers, producing a toolpath to print the individual layers, uploading these

data into the computer, and then, building the part layer-by-layer. This fact avoids the need to use different tools, dies or molds having a substantial time reduction in design and production of low volume parts (Pires, 2021).

There are several technologies based on the general concept of multi-layer slicing explained previously. In 2009, the American Society for Testing and Materials (ASTM) established standards for AM technology. ASTM F2792-12A classifies AM processes in eight categories as is shown in Table 4 (ASTM F2792-12a, 2012), (ISO/ASTM52900, 2015), with a brief description of them (Charalampous, 2020). PBF and DED are the most commonly used technologies for metal AM. Figure 12 shows different ways that are known both processes based on the heat source, feedstock and commercial machine suppliers (Lewandowski, 2016).

Table 4. Additive Manufacturing processes (Charalampous, 2020)

| 3D printing process | Description | Utility in metal AM |
|---|---|---|
| Material extrusion | Material is extruded through a heated nozzle | – |
| Material jetting | Deposition of build material droplets by an inkjet print head | – |
| Binder jetting | Deposition of liquid bonding agent droplets to a powder bed | ✓ |
| Sheet lamination | Sheets of material are bonded to form an object | ✓ |
| Vat photopolymerization | Selective curing of liquid photopolymer using light activated polymerization | – |
| Powder bed fusion (PBF) | Selective thermal fusion of powder bed using a laser or an electron beam | ✓ |
| Directed energy deposition (DED) | Wire or powder is extruded from a nozzle and completely melted by an electron beam or a laser | ✓ |
| Cold spraying | Powder is blown at high velocity from a nozzle in order to cause adhesion and form an object | ✓ |
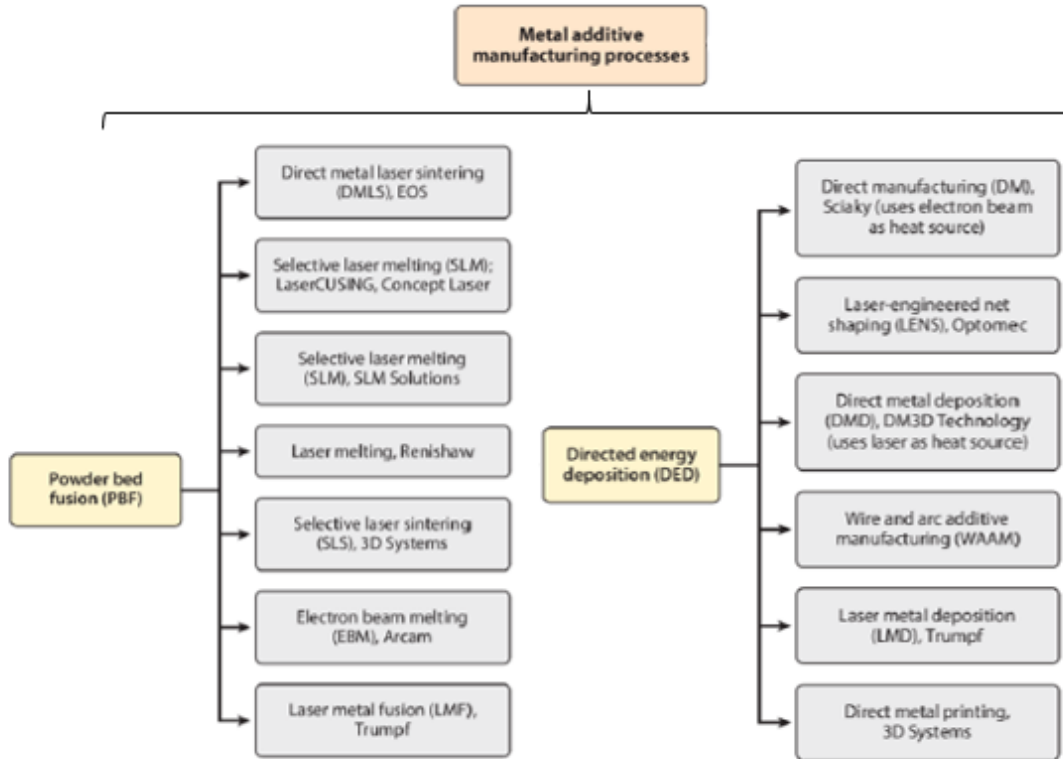
Figure 12. Metal additive manufacturing processes and their commercial machine supplier names (Lewandowski, 2016)

## 2.6.1 Directed Energy Deposition (DED)

DED processes involve a concentrated thermal energy source that melts the feedstock (powder or wire) protected by an inert gas at the precise time that is being deposited into the substrate. Figure 13 displays the general schematic of L-DED process and a classification based on type of feedstock and energy source (Kladovasilakis, 2021). Comparing wire and powder-based L-DED (LP-DED), wire provides lower resolution, higher efficiency and higher deposition rate (Dass, 2019). Movement is controlled by a CNC and in some cases a robot is used to deposit material.

This process is summarized in four stages (Dutta, 2019): (i) a target component is placed on the work table with different degree of freedom; (ii) 3D model is uploaded and the toolpath set; (iii) a melt pool is created by the energy source melting the feedstock, then the melt pool solidifies and forms layers of metal; and (iv) printing subsequent layers until build the whole component. This studio is focused on the powder based DED system with laser as energy source.

It is important to understand that each set of equipment (DED machine, laser source, powder feeder, and nozzle) combined to a specific set of materials (substrate, filler metal

characteristics and shielding gas) have a particular result, even using the same combination of parameters (Thiesen Junior, 2021).
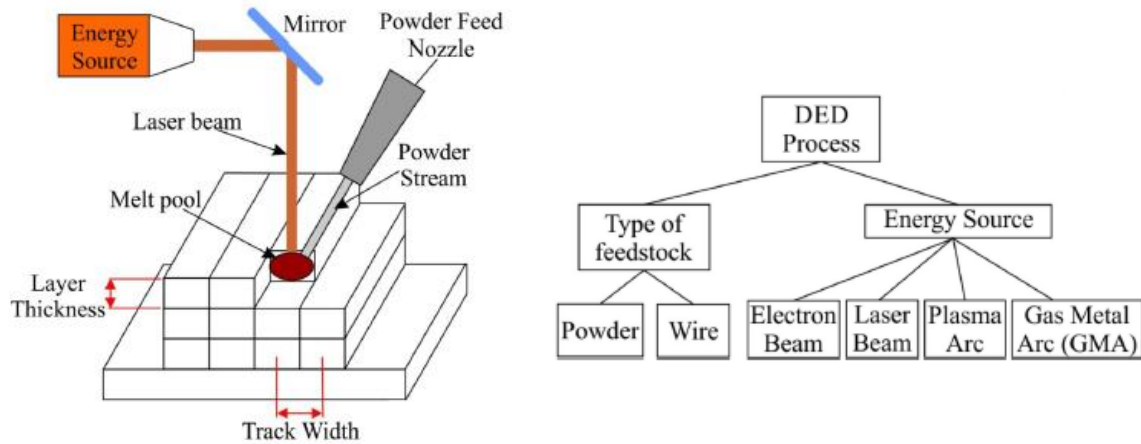


A) Schematic Layout L-DED          B) Classification L-DED processes

Figure 13 Schematic layout and classification of L-DED processes (Kladovasilakis, 2021)

LP-DED process has a huge technical capability such as functionally graded components composed of multi-material printing, to repair and refurbish high-tech components, such as turbine blades (Babuska, 2021).

Nevertheless, the resolution is limited by coarser powder and lower cooling rates relative to other laser-based techniques as such as L-PBF (Melia, 2020). L-DED processes is not able to manufacture complex structures due to the fact that larger melt pools result in a reduced capacity to produce small-scale features (Gibson, 2015). It is difficult to produce tight tolerance as closed cooling passages and wide overhangs (Dutta, 2019). Other disadvantage is the high distortion in printed parts. Besides, porosity is one of the most significant defect, that affect directly the mechanical properties of DED components (Dass, 2019). Regardless, it is a developing industry that is evolving by leaps and bounds in recent years.

L-DED is a non-equilibrium process that possess fast cooling rates around $10^3$ to $10^5$ K/s (Gu, 2012) (Gibson, 2015). Main process parameters for L-DED are laser beam spot size, feed rate, travel speed, feedstock properties, laser power, carrier gas flow rate and layer thickness (Dass, 2019). The high number of variables involved makes L-DED a complex process. A brief explanation of the most relevant factors is presented (ASTM, 2016):

o Travel speed (s): According to ASTM F3187 the relative speed between the headstock and the component is called travel speed, also known as traverse rate or scanning speed. Control speed it is essential since influences distortion and thermal history. Usually the unit used is millimeter per minute (mm/min).

o Laser power (P): It is the optical power output of the laser beam, typically a continuous wave (CW) laser is used. The unit of P is Watts (W).

- Spot size (Ø): This factor is related to the intensity of laser that means the diameter of the laser on the part.
- Hatch spacing (D): It is an equal lateral distance between beads typically measured in the middle of the center of passes.
- Feed rate ($\dot{m}$): It is the quantity of powder delivered per unit of time. The unit is grams per minute (g/min).
- Carrier gas (g): The main objective is to transport the powder to the melt pool, typically used an inert gas.
- Shielding gas (G): As such as a welding process it is a protective gas to reduce atmospheric contamination.
- Dilution: According to AWS A3.0 standard it is the percentage of substrate or previous weld metal in the bead. It is basically the change in chemical composition of a molten metal caused by the mix of materials. Figure 14 shows a representation of calculation of base metal dilution from cross-section view (AWS, 2010).



CALCULATION OF BASE METAL DILUTION FROM CROSS-SECTIONAL AREA OF WELD BEAD

$$\% \text{ DILUTION} = \frac{B}{A + B} \times 100$$
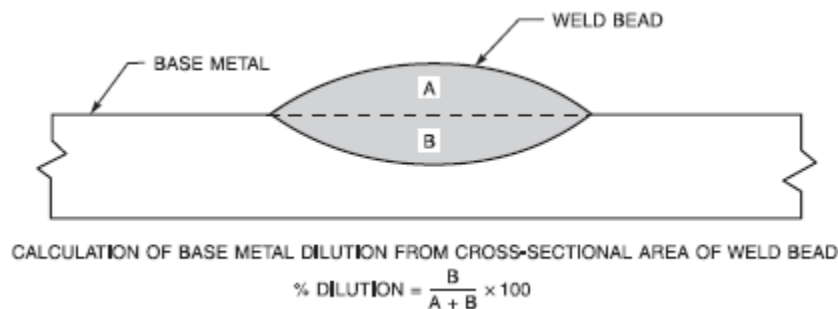
Figure 14. Dilution scheme and calculation according to AWS A.30

- Layer thickness (t): it is the programmed distance between the last layer and the next. This is in length units (µm).
- Delivered energy (E): It is defined as the parameter which provides a measure of the total laser energy delivered in the process, it is expressed in terms of J/mm$^2$.

$$E = \frac{P}{S\text{Ø}} \quad (1)$$

- Energy density (ED): the input in additive manufacturing can be quantified by energy density (Liu, 2018), which is defined as a function of energy beam power P, scanning speed V, beam diameter D or hatch spacing H, and layer thickness t. Several researchers (Jia, 2014) (Popovich, 2017) showed that ED has a great impact on microstructure, porosity, and mechanical properties of the additive manufactured components since it will determine the heating/cooling rate and the thermal dynamic behavior and the shape of the melt pool.

$$ED = \frac{P}{vHt} \quad (2)$$

## 2.6.2 Laser Powder Bed Fusion (L-PBF)

According to ASTM 52900 powder bed fusion is an additive manufacturing process that use thermal energy to fuse selective regions of a powder bed (ASTM, 2015). This process has the same steps of the printing process of samples summarized in Figure 15. L-PBF machine have a container filled with the powder material. The metal powder is initially spread on a plate or substrate moving a re-coater blade. Then a laser beam melts the powder and create a new layer. The build platform moves down by the thickness of a single layer. The previous action is repeated and the process goes on until the object is complete manufacture. Finally, the printed object is removed to the substrate in almost every case except in repair or remanufacture parts.
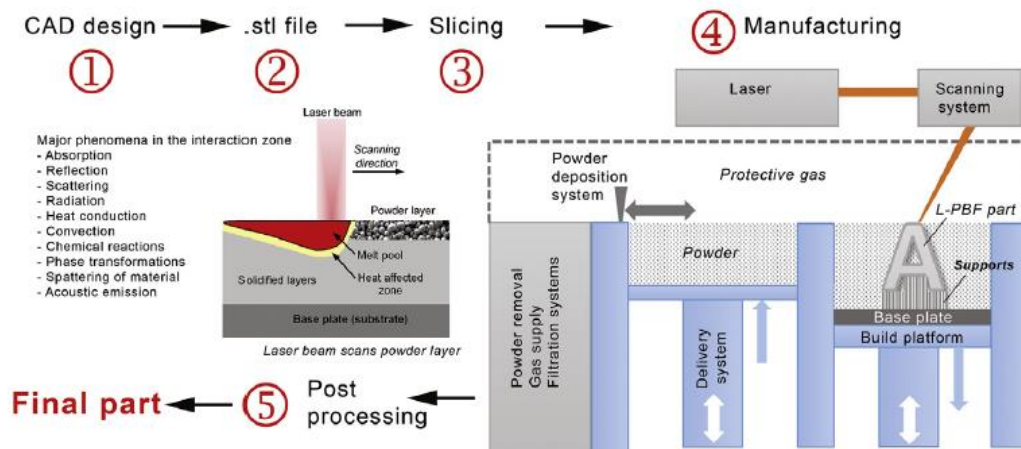


Figure 15. Schematic process of L-PBF (Debroy, 2018)

Almost all the parameters described previously in 2.5.1 are used in L-PBF. Rehme and Emmelmann indicated more than 100 input parameters that affect the L-PBF process (Rehme, 2005). Parameters are affected by different topics: material (density, thermal conductivity, melting point, PSD, etc.), machine (wavelength, power capacity, etc.), process-parameters (focal spot diameter, scanning speed, oxygen level, layer thickness, etc.), and post-treatments parameters (time, temperature, etc.).

L-PBF process has different technical capabilities as high resolution, create various mechanical properties combine lattices with macrostructures, manufacture complex geometries, in small batches. Otherwise, common disadvantages found are: need to use supports, a high rough surface finish, comparatively slow manufacture process, powder could be explosive and equipment is expensive.

## 2.6.3 Deposits characteristics

Typically, the process of developing suitable parameters in an additive manufacturing or welding process starts from the most basic geometric analysis: the single bead. Depending on the combination of some variables of the process, it is possible to get different bead geometries. Figure 16a shows the most important characteristics to measure on a single bead. Characterize all dimensions is important to describe dilution, the wettability angle that is related to stresses and to prevent the appearance of pores and voids. A common measurement is the aspect ratio (R) that is the ratio between height and width (h/w), as seen in Figure 16b (Ion, 2015).



A) Single bead dimensions          B) Bead-cross section. Wettability angle
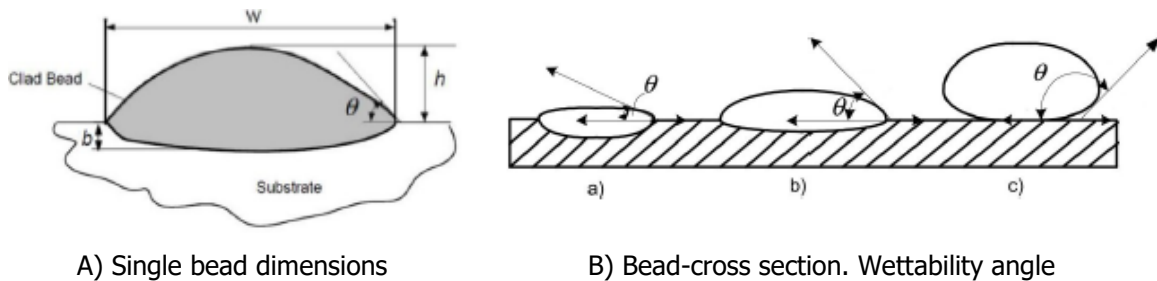
Figure 16. Beads characteristics (Toyserkani, 2005)

Apart from bead geometry, quality is related avoiding any interruption of the material structure. This concept is called discontinuity (AWS, 2001). To identify any discontinuities on deposits produced by process parameters it is an important activity to develop a correct procedure specification. Standard specification for AM procedures has not yet been developed, for this reason, acceptance criteria are specified by the end-user (Thiesen Junior, 2021). According to the ASTM E1316, a defect is defined as a group of undesirable discontinuities that not meet specified acceptance criteria and are rejectable (ASTM, 2014). The most found discontinuities are summarized below:

- o Lack of fusion (LOF): Lack of fusion is a kind of discontinuity that is often observed with high aspect ratio beads, producing crevices at the toes of layers with irregular shape (Dass, 2019). Mechanical properties may be negatively affected in the presence of this discontinuity that in some cases leads to part rejection (Debroy, 2018). Proper selection of process parameters could avoid the appears of LOF. Figure 17 shows the difference in geometry between LOF and porosity.



Lack of fusion porosity          Keyholing porosity
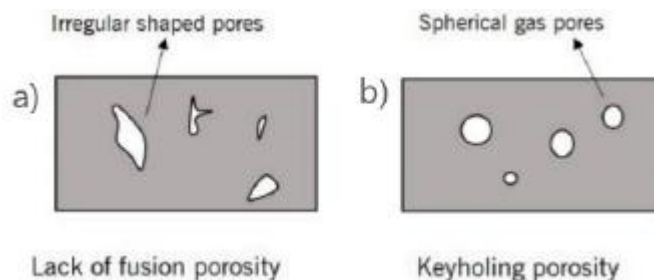
Figure 17. Geometry of lack of fusion and porosity (Dass, 2019)

- Porosity: There are three different kinds of porosities that are represented in Figure 18 (Lawrence, 2017). Figure 18a represents inter-bead porosity that happens near to the base of beads. Figure 18b shows a schematic of inter-layer porosity due to incomplete fusion between layers. Finally, intra-layer porosity is caused by trapped gas inside the bead having a spherical shape typical of gases vaporized (Figure 18c).
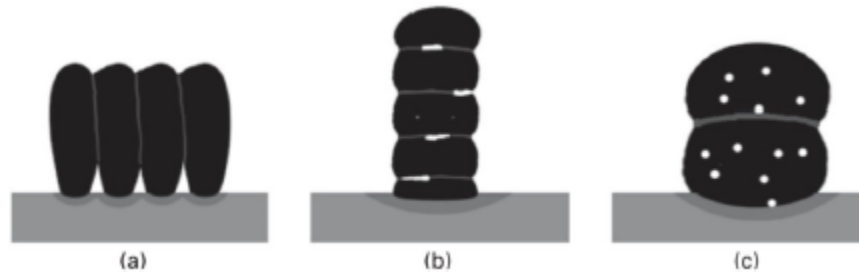


Figure 18. Types of porosity (Lawrence, 2017)

- Cracks: The susceptibility to crack is highly dependent of chemical composition. An important fact is to assure the correct selection of filler metal and adequate process parameters to avoid hot cracking. Post Weld Heat-treatment (PWHT) is another source of cracking.
- Distortion and residual stress: successive layers of metal molten produce complex residual stresses due to a huge cycle of contraction and expansion. Mechanical properties such as tensile or fatigue could be affected by those stress state. High thermal stresses may cause rejectable distortion (Ion, 2005).

## 2.7 Literature Review

Literature review is divided in two parts: characterization of GTD 111 and additive manufacturing methods to repair blades. First part, it is an extensive exploration about microstructure, heat treatments, properties and performance of GTD 111 alloy. On the other part, AM studies are focused on L-PBF and L-DED processes repairing blades.

Parameters to manufacture a cast GTD 111 alloy is defined in US 9322089 patent (Biondo, 2016). Having excellent casting properties, low density and good stability to negate the formation of topologically close packed phases (TCP). This author establishes a standard heat treat of the alloy with the following steps. First, a solution heat treatment at 2050° F (1120° C) ± 25° F (4° C) for 2h ± 15 min was defined, followed by a cooling gas quench to below 1100° F (600° C), preferably carry out in a controlled atmosphere. This step has an objective to dissolve γ' phase, heating close to the γ' solvus (Biondo, 2016).

Subsequently, the alloys were elevated to 1975° F (1080° C) ± 25° F (4° C) and aged during 4 h ± 15 min followed by a gas quench cooling. The last step is elevating temperature to 1550° F (845° C) ± 25° F (4° C) stabilizing for 24 h ± 30 min and cooling at room temperature. It will cause a controlled formation of γ' to precipitate with the correct amount

and distribution of γ′ precipitates. Following these parameters with the correct chemical composition, it is possible to obtain 180 Ksi at 1200° F in ultimate tensile strength (Biondo, 2016).

Knowledge of the microstructure alloy is fundamental to understand the mechanical properties and material behavior in service condition. For the fact that superalloys never reach a state of equilibrium, several authors studied the microstructure in different conditions (original, in services and after heat treatments). As original, there is evidence to suggest that there are two different precipitates shapes: primary γ′ precipitates mostly cubic shape and secondary γ′ precipitate with spherical shape (Kountras, 2004) (Daleo, 1996).

Some of the first researchers who published property data of GTD 111 were Daleo and Wilson, who identified some of the basic mechanical and metallurgical properties. Determining the microstructural stability of the material and confirmed that the extensive published data base for René 80 could be used in GTD 111 (Daleo, 1998). The standard heat-treated condition consists of a duplex gamma prime precipitate distributed in the face centered cubic (FCC) gamma matrix with a thin discontinuous carbide layer of $M_{23}C_6$ and $M_6C$ at the grain boundaries (Sajjadi, 2002).

In service condition the coarsening of γ′ appeared and complex carbide reactions occur (Daleo, 1998) (Sajjadi, 2002) (Wangyao, 2008). A carbide layer of $M_{23}C_6$ continued growth due to a degeneration of MC carbides into $M_{23}C_6$ + γ′ in the matrix and at the grain boundaries (Daleo, 1996) (Turazi, 2015). At 900° C the secondary gamma prime is dissolved and affects the mechanical properties before and after thermal exposure (Daleo, 1996) (Sajjadi, 2001). There are fluctuations in ductility and tensile strength with respect to temperature, after 800 ° C an abrupt decrease in yield strength and the elongation occurred , presenting a constant value at 500 ° C (Sajjadi, 2002) (Sheibel, 2018). The mechanical properties of GTD 111 are superior to those of IN738LC (Sajjadi, 2002).

Generally speaking, the elastic interaction energy plays a role in the distribution and shape of precipitates (Berahmand, 2013). The smallest precipitates usually have spherical shape and when they become coarse transform into cubic shape (Berahmand, 2012). Villada et al showed that there are clear evidences that γ′ phase exhibit significant changes in shape and size, in specific, into the trailing edge tip occurred the coalescence and coarsening of the γ′ (Villada, 2019).

Other research topic is to define a correct rejuvenation thermal treatment that could be use in blades refurbishment (Wangyao, 2006). Several authors established that the rejuvenating treatment reduce the size of γ′ and recovered hardness values, having more uniform microstructural characteristics results the solution treatments executed insajj the range of 1175-1200° C (Turazi, 2015) (Wangyao, 2010). In constrast, the solutioning treatments below to 4 h do not dissolve the previous coarse γ′ particle (Wangyao, 2015). It has been reported that full solution of γ′ is about 1180-1235° C (Balikci, 1997) (Hale, 1994). At 1200° C local melting of γ-γ′ eutectics occurs, and its effects could be negative as reduction of percentage of γ′. For that reason, a partial solution is introduced using 1120° C to avoid nucleate harmful phases (Sajjadi, 2006).

The existing literature on GTD 111 showed severe cracking issues, strongly suggesting that there are many problems associated with the weldability of this alloy (Athiroj, 2018). For that reason, the use of low power processes is recommended to avoid that kind of defects.

Several works were found around AM repair into blades using L-DED and L-PBF. The following table describes the selected studies that are classified by process and material. All research has a brief description. L-DED process is more commonly used to repair blades due to facility to print into medium or large pieces. However, L-PBF has demonstrated tremendous qualities to manufacture and repair blades.

The main researchers working on blades using LP-DED are following described. Li et al. were focused on GTD 111 alloy, obtaining successfully deposits with directional solidification (DS) and applying Rene 80 and IN 625 powder (Li, 2006). Some issues as microfissuring and stray grains are solved by adding multiple pulses and 25% of overlap (Li, 2012). Others authors studied René 80 substrate, acquiring soundness in deposits with oriented microstructure (Huarte-Mendicoa, 2019) (Liu, 2010).

IN 738 is highly used in blades, in specific in the first row, there are some cases that preheating is not necessary to avoid defect (Xue, 2000) (Zhang, 2021). However, its high susceptibility to crack is managed by preheating (Chen, 2008). According to previous researches, LP-DED feasibility to repair IN738 was demonstrated and an innovative solution was developed by Zhang et al. using a doped powder of IN 738+ IN718 that improve properties and integrity (Zhang, 2021).

In aero-engine components is common to implement IN 718 in blades. Unal-Saewe et al and Qi et al developed a stable tip reconstruction with good accuracy and non-defects (Qi, 2009) (Unal-Saewe, 2021). Aside from this, it was implemented a methodology to repair a complex geometry, integrating a 3D non-contact digitization, a milling machine, and a L-DED reconstruction in the same machine (Yilmaz, 2010).

Additional researches are presented in Table 5, different materials are printed successfully by LP-DED with the objective of restitution blades shapes (Gandini, 1997) (Bi, 2011) (Jones, 2012) (Wilson, 2014) (Keshavarz, 2021).

Table 5. Selected studies showing AM as an emerging method to repair blades

| Process | Material System | Reported Functionality or developed method | Reference |
|---------|-----------------|--------------------------------------------|-----------|
| LP-DED | GTD 111 | Rene 80 powder was successfully deposited on GTD 111 substrate with a refined and directionally solidified microstructure. Some defects were found such as porosity, microfissuring and stray grains. | Li, 2006 |
| | GTD 111 | Multiple pulses enhanced the presence of microfissures by remelting and healing effects. An optimal overlap of 25% was set to reduce the temperature gradient at bead boundaries and restrict the stray grain | Li, 2012 |

| | | formation. Deposits were achieved crack-free with René 80 and IN625. | |
|---|---|---|---|
| | René 80 | A process window was found to relate parameters (Power, scanning speed and spot size) with microstructure. Energy density governed the formation of a single crystal microstructure. | Huarte-Mendicoa, 2019 |
| | René 80 | Better quality of deposits using fine powder. It was found that a less power mass ratio and linear energy would lead to less crack susceptibility. | Liu, 2010 |
| | IN 738 | Established the use of IN625 for low stress areas having lower hardness than the base metal with deposits crack-free defects. IN 738 is used in high stress areas and preheating a detailed inspections is required. | Chen, 2008 |
| | IN 738 | Reasonable tensile stress and toughness for deposit of IN 738 without preheating. Defects free and grew epitaxial with flipped of growth by laser scan direction in a thin wall. | Ramkrishna, 2019 |
| | IN 738 | Optimized the process parameters displayed epitaxial growth and free cracking (P= 500W, V=0,25m/min and D=2mm). | Sun, 2005 |
| | IN 738 | Thin-wall structures was built correctly without preheating. Deposits of IN738 have directionally solidified (DS) microstructure. Standard heat treatment was carried out without defects and mechanical testing are according to IN-728 baseline data. | Xue, 2000 |
| | IN 738 | Demonstrated superior mechanical properties and suppression of cracks doping IN738+IN718 with respect to IN738. | Zhang, 2021 |
| | Ni Superalloy | Deletion of formation of cracks by the implementation of a closed-loop process control system that controls melt pool temperature. | Bi, 2011 |
| | Udimet 520 | Feasibility to repair a tip is demonstrated and validated by sound welds and mechanical properties using IN 625 as filler metal. | Gandini, 1997 |
| | IN 718 | Developed process to build-up a stable blade tip geometry | Unal-saewe, 2021 |
| | IN 718 | A reliable and cost-time effective repair solution of a tip blade is executed in a hybrid machine (additive and subtractive) and a digitizing system. | Yilmaz, 2010 |

| | | Method deposition with no lack-of-fusion defects and good dimensional accuracy for fabricating and repairing airfoils of aircraft engine. | Qi, 2010 |
|---|---|---|---|
| | IN 718 | | |
| | Rene 142-Merl 72 | Powder blend comprising exposed good weldability without preheating. Being a good alternative for turbine tip repair, showing higher mechanical and oxidation properties than Rene 80 welds. | Keshavarz, 2021 |
| | Ti | Successful remanufacture of turbine blades using additive, subtractive and inspection tools in a single machine. | Jones, 2012 |
| | SS 316 | Efficient method to restore dimensions of a wide range of damaged blade parts. Improve environmental impacts due to reduction of at least 45% carbon footprint when the repair volume is 10% (1.56 Kg). | Wilson, 2014 |
| L-PBF | CMSX-4 | Improved mechanical properties and microstructure due to a finer columnar growth in the <001> plane with a single pass of 1000 um. Reduction of elemental segregation was observed in the deposit region compared to the base metal. | Basak, 2017 |
| | IN 100 | Soundness printed samples were obtained with a thickness between 1000 um to 6000 μm. Determined that power and scan speed are key parameters to reduce pores and a good pool shape | Acharya, 2015 |
| | Titanium Aluminides | L-PBF and L-DED processes are deposited onto TiAl-based alloys used as compressor stator vanes or low-pressure turbine blades. Similar values of hardness and features of microstructure were found. | Rittinghaus, 2020 |
| | Ni and Ti alloys | Siemens has developed a technology that enables repair of turbine blade degraded tips. Providing a new CAD-CAM chain that automatically adapts the shape of repaired tip to each blade. | Siemens, 2020 |
| | NiAl-based | An innovate powder of Ni41Al41Cr12Co6 was used to manufacture a turbine rotor blade models obtaining optimal technological parameters of the L-PBF process. Microcrack-free turbine rotor blades with porosity of 0,94% as built and 0,25% after HIP were obtained. | Kaplanskii, 2020 |
| | IN 718 | A turbine blade is manufactured by L-PBF and is evaluated its anisotropy investigated via tensile at room and elevated temperature. In conclusion, they found that the mechanical properties are similar but the build orientation highly affect to remove supports and surface roughness. | Caiazzo, 2017 |
| | LW 4275. Ni alloy | LW 4275 is used in hot path gases. L-PBF deposits in the as-built condition presents elongated columnar grains with orientation along <100> direction. A heat treatment was carried out obtained increase in hardness and mechanical properties. | Jena, 2021 |

There is less work related to print new blades or in service condition by L-PBF than L-DED. Nevertheless, important researches were developed in Ni and Ti alloys. Generally speaking, improved mechanical properties were obtained due to refiner microstructure and a controlled texture (Jena, 2021) (Basak, 2017). To print onto a blade, it is necessary to customize the traditional L-PBF machine and asset a perfect blade support. All studies related to L-PBF are shown in Table 5.

# CHAPTER 3: OBJECTIVES AND APPROACH

## 3.1 Objectives

### General Objective

To evaluate technical feasibility for the recovery of GTD 111 blades degraded in service by heat treatment and additive manufacturing.

### Specific Objectives

To identify the main degradation evidences of GTD 111 blades in service in a thermoelectric power plant.

To determine microstructural changes of GTD 111 exposed to high service temperatures for a long time produced by heat treatment.

To evaluate the effect of some parameters of LP-DED and L-PBF processes on the integrity and microstructure of the molten metal on the thermally restored GTD 111 substrate.

## 3.2 Approach/ Methodology

Figure 19 shows the methodology carried out in this research. Two different blades (1 and 2) with 22 k and 30 k hours in service respectively were used. First of all, a previous characterization was carried out to determine the degradation status after its service; then, a partial solution heat treatment of 1120 °C/2h plus a furnace cooling was carried out to prepare the substrate to the different AM processes. Some phases were identified through Optical Microscope (OM) and Scanning Electron Microscope (SEM). Hardness testing were done in samples before and after the heat treatment. Optical Emission Spectroscopy (OES) was used to characterize the chemical composition of blades and deposits.
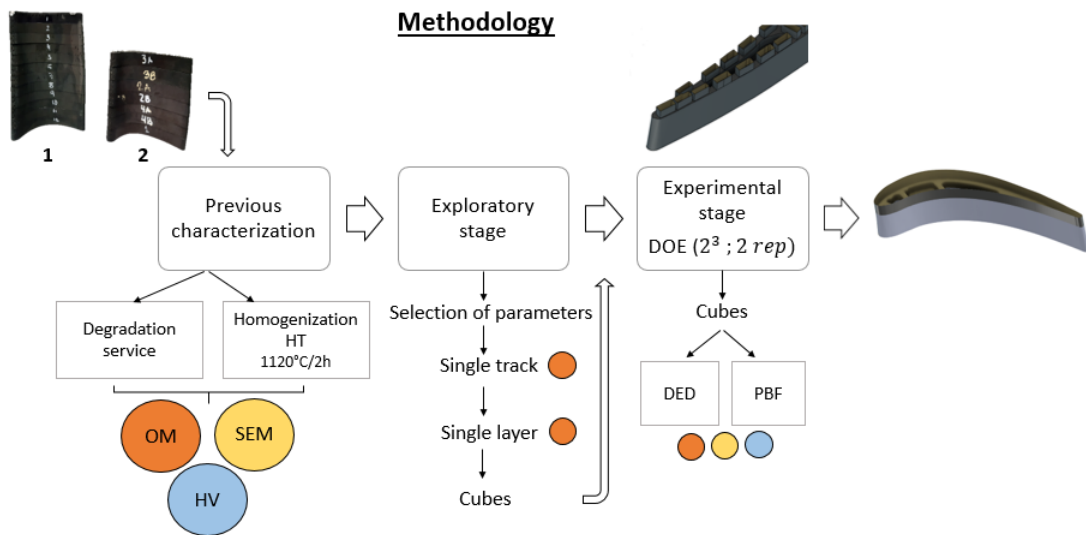
Figure 19. Diagram of research methodology

The second step is an exploratory stage related to additive manufacturing (AM) gathering essential information of parameter ranges already used in the literature. This information is specific for GTD 111 and René 65 and include nominal values of essential variables, possible defects, selection criteria of parameters and predictive diagrams. A range of power laser and travel speed was selected and a spot size and feed rate were fixed by preliminary trials. Experiments of single beads were carried out and several characteristics were identified to classify the parameters tested. Some selection criteria are the with/depth ratio, porosity, wet angle and quantification of number of cracks. The best parameters found for single track were used for single layer experiments. In this part it is important to set an adequate hatch spacing, to permit avoid pores and to have a homogeneous deposit.

In the third stage a design of experiment (DOE) per process was done. The input of this stage comes from the best results of single layer. The samples are parallelepipeds deposited varying a range of power laser, scanning speed and rotation between layers; on the other hand, feed rate, spot size and hatch spacing were kept constant. It is important to have a homogeneous direction of solidification and to keep them defect-free. Microstructural and properties characterization were done in each sample. The buildup of a squealer tip with both processes conforms the last stage of the research.

# CHAPTER 4: MATERIALS, EQUIPMENT AND METHODS

## 4.1 Materials

### 4.1.1 GTD 111

The material used in this research was extracted from a GE7FA turbine, in specific from two different first stage blades as seen in Figure 20A. It was carried out several cross sections cutting by Electrical Discharge Machining (EDM) along the longest axe. Blade 1 has 30 K service hours (almost half lifetime) and blade 2 has 22 k in service. A phase diagram of a binary system Ni-Al is used (Figure 20B). The phase diagram indicates the composition and temperature at which $Ni_3Al$ is formed or developed. Considering a $C_0$ composition of a Ni-8wt%Al alloy, the total solubilization of the Ni3Al phase will occur above 1200°C.

All of them were heat treated in a general furnace (Figure 20C) by a partial solution at 1120°C/ 2h with an argon atmosphere, following the temperature profile showed in Figure 20D. Heating rate was 0.3°C/s with 2 hours of soaking period. For logistic concerns samples were cooled by furnace cooling ~ 1°C/min.
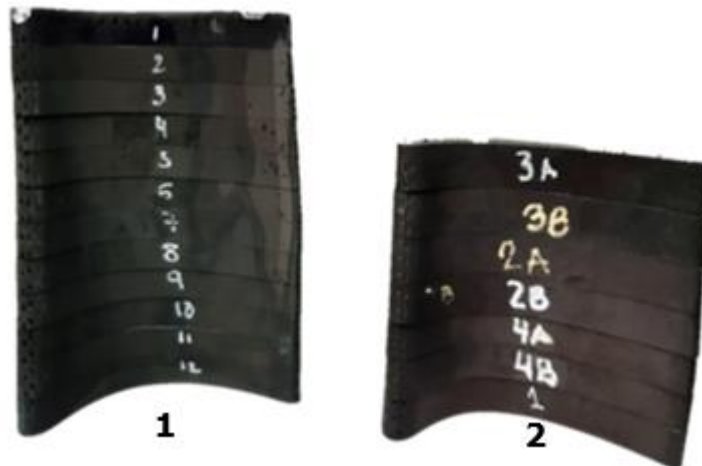


A. First stage blades used in experimental procedure.
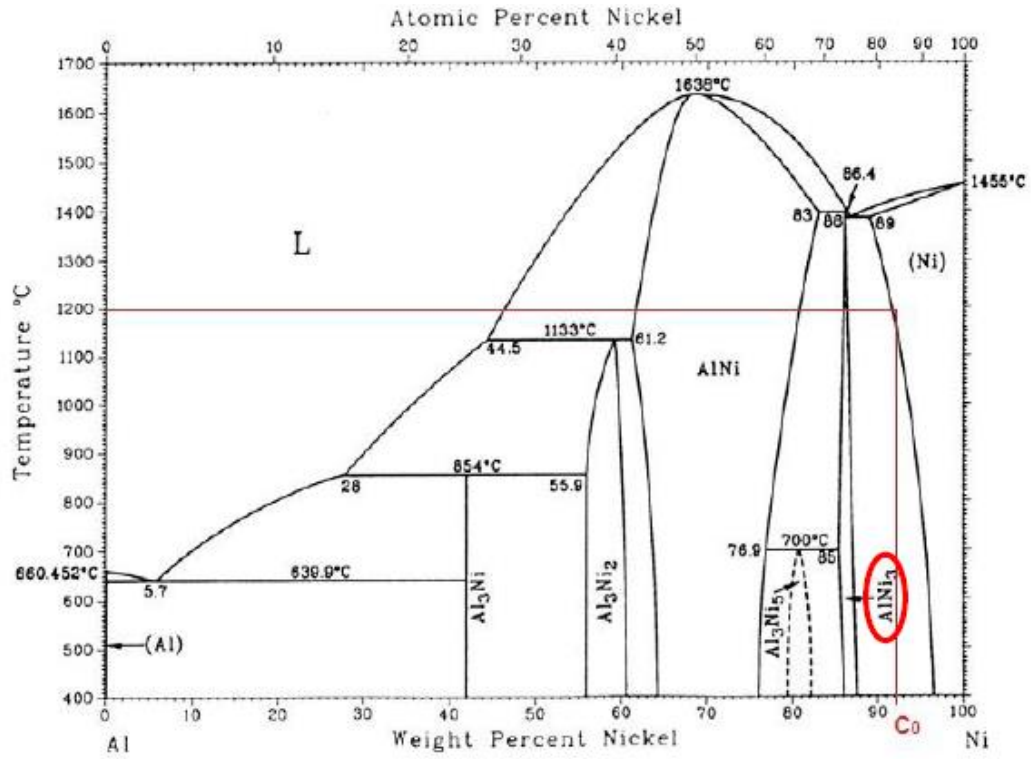
B. Phase diagram of nickel and al content



C. Samples before partial solution heat treatment
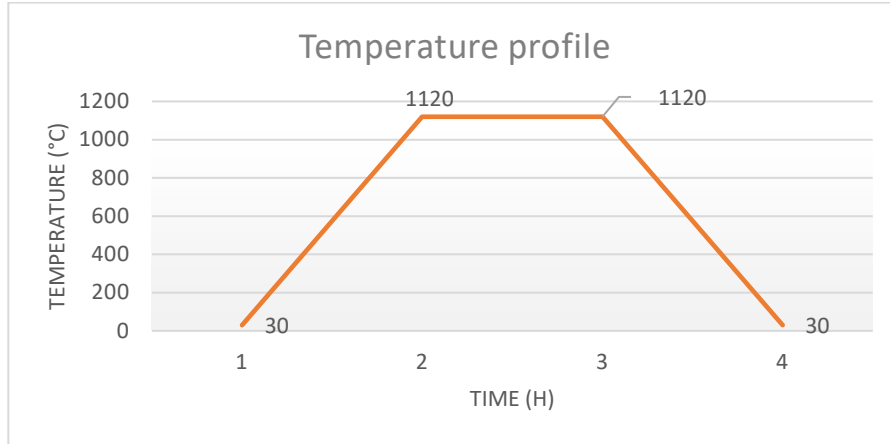
D. Partial solution Heat Treatment

Figure 20. Samples extraction and preparation

The chemical composition of blades investigated is illustrated in the next Table. Five measurements per blade were carried out by Optical Emission Spectroscopy (OES) using a *Ametex-Spectromax* device. Values of W, Al and Ti are slightly higher than the reference chemical composition of GTD 111, however in a general view both results are similar to GTD 111 specifications.

Table 6. Chemical composition GTD 111 blades

| Chemical Composition GTD-111 Superalloy (wt%) Measured by Optical Emission Spectroscopy | | | | | | | | |
|---|---|---|---|---|---|---|---|---|
| Material | C | Cr | Co | Mo | W | Al | Ti | Ta | Ni |
| GTD 111 (Ref) | 0,12 | 14 | 9.5 | 1.5 | 3.8 | 3 | 5 | 3.15 | Balance |
| Blade 1 | 0,11 | 14.11 | 11.03 | 1.59 | 4.51 | 3.48 | 5.13 | 3.21 | 56.4 |
| Blade 2 | 0,09 | 14.15 | 10.59 | 1.58 | 4.22 | 3.36 | 5.11 | 3.16 | 57.71 |

A 3D microstructual reconstruction of GTD 111 was built and is showed in Figure 21. The dendritic growth is columnar in <001> plane, which is shown in the vertical axis. This feature improves the creep and fatigue resistance compared to equiaxed solidification mode (Jovanovic, 1998).



Figure 21. 3D microstructure reconstruction

## 4.1.2 Powder René 65

René 65 powder was obtained from ATI Powder Metals in the standard 15-45 µm of particle size distribution (PSD) (Tin, 2020). Figure 22 shows a metallography analysis of René 65 powder. Figure 22A helps to see the porosity level found in different micrographs and identifies the shape of some of them. Powder has not a huge quantity of porosity and has a microstructure typical of solidification (Figure 22B).
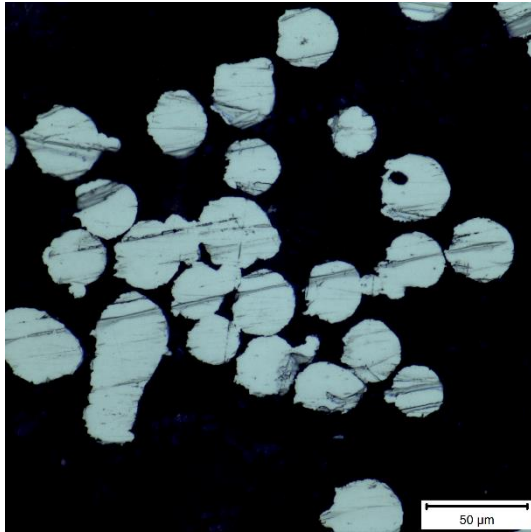


A) Porosity and amorphous shape 500X        B) Etchant powder 1000 X
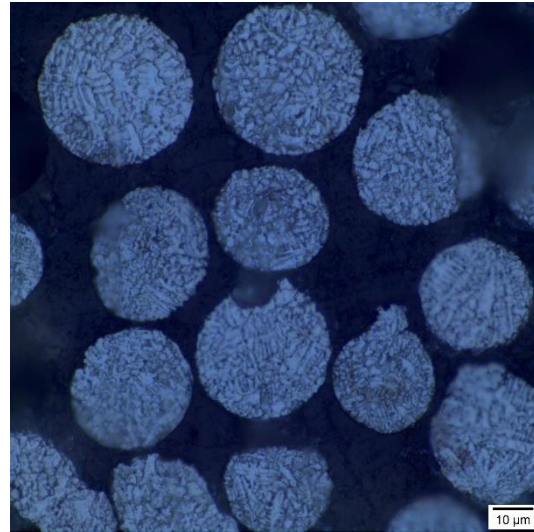
Figure 22. Metallographic René 65 powder

SEM images (Figure 23) show a general view of the René 65 powder morphology. It reveals that almost all are spherical particles with some elongated forms (yellow arrows). The presence of satellite particles is notable (white arrows). In some cases, it is observed agglomeration of particles (orange arrows). All of those characteristics can affect the powder flowability in the AM processes in special LP-DED.
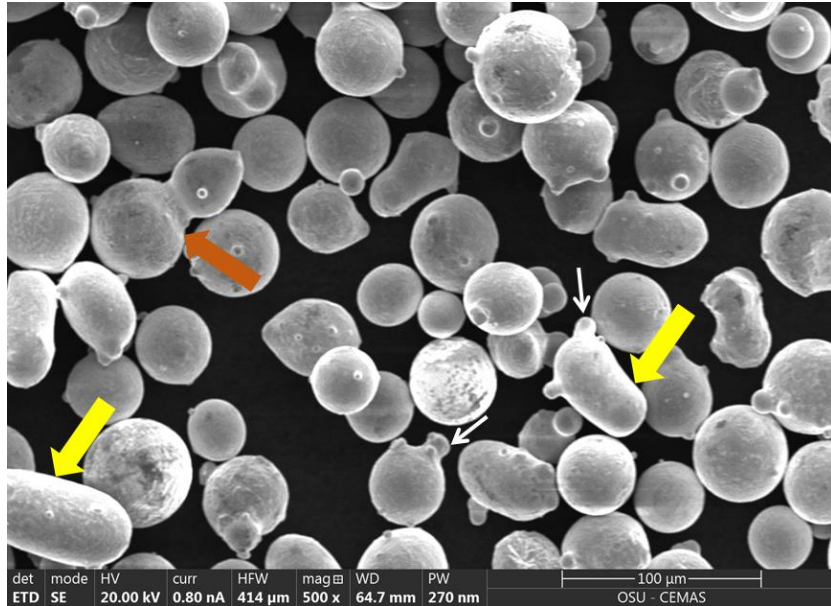
Figure 23. SEM images Rene 65 powder

Particle size distribution (PSD) was measured using image analysis, as seen in Figure 24, aided by MIPAR (Sosa, 2017). It was measured 5 different images showing that almost all of the particles are between 30-60 μm according to the PSD reported by ATI ±15-45 μm. That kind of powder is specialty for using in L-PBF.
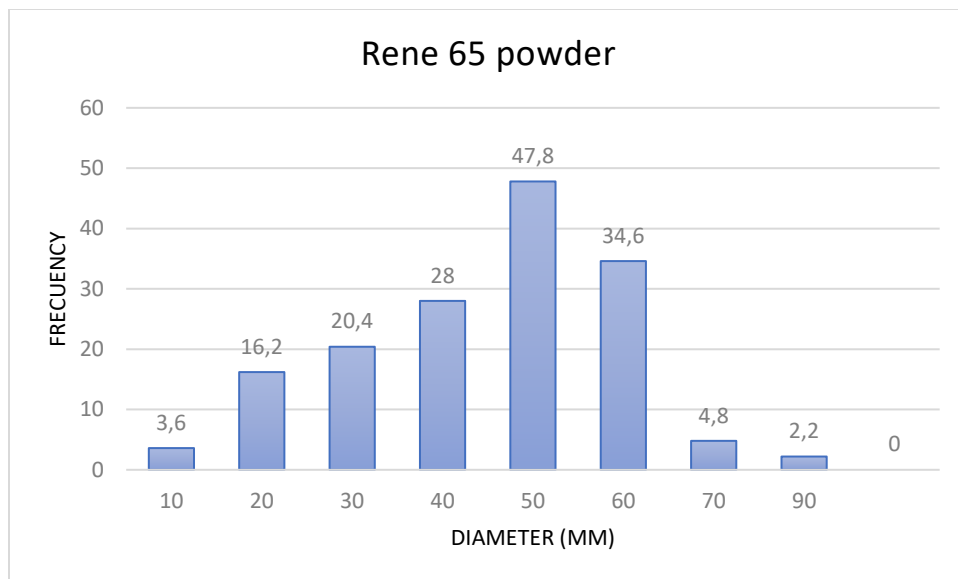

Figure 24. Particle size distribution of Rene 65 powder

## 4.2 Additive Manufacturing Processes

## 4.2.1 LP-DED

Laser Powder Directed Energized Deposition experiments were carried out in a *TrumpF TruLaser Cell 3000* machine from *TRUMPF* company owned by The Ohio State University. It is a CNC machine with 5-axis for cutting and welding operations, with a modular design integrated of a gas system, compressor, hopper powder feeders, chiller and laser source *(TruDisk 2000)*. A schematic diagram of LP-DED process is shown in Figure 25. Argon is used as such as carrier gas and shield gas with 9 L/min and 20 L/min, respectively. The laser source is supplied by *TruDisk 2000* device using a solid-state laser with a wavelength of 1030 nm and 2000 W max, a Ø spot of 1 mm was selected. The powder was fed coaxially by a three-jet powder nozzle working a distance of 12 mm with 12% of amplitude powder. Technical data of *TruLaser Cell 3000* machine is possible to find in Appendix I.

Programming codes can be done through CAD/CAM programs or by numerical control (NC). In this work, all codes were manually programmed using NCs. All programs developed for LP-DED impressions are compiled in Appendix VI. *Trumpf* technology has some specific commands however, it is basically G-code programming.
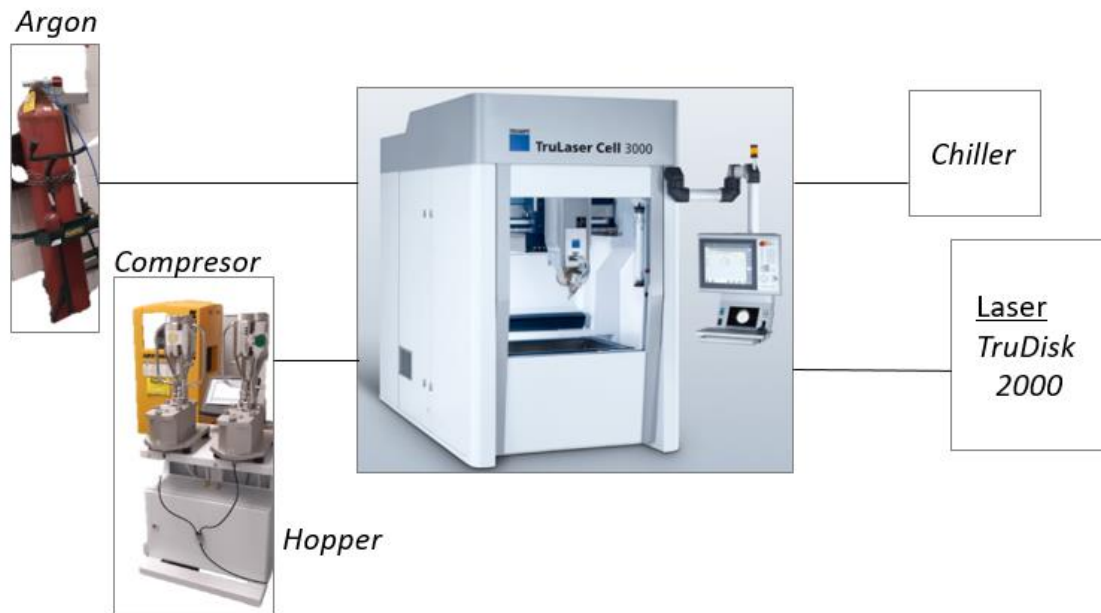


Figure 25. Experimental setup of LP-DED process

The powder was heated for 10 hours in an oven at 100°C to remove any moisture present. It is important to characterize previously the followability of powder. Hopper powder feeder was activated during 2 minutes with steps of 10% of amplitude powder and then measured the weight of powder, the results are plotted in Figure 26. It is noticed that its behavior is similar to a line with some imperfections due to PSD. PSD recommended by TrumpF is 45-90 μm.
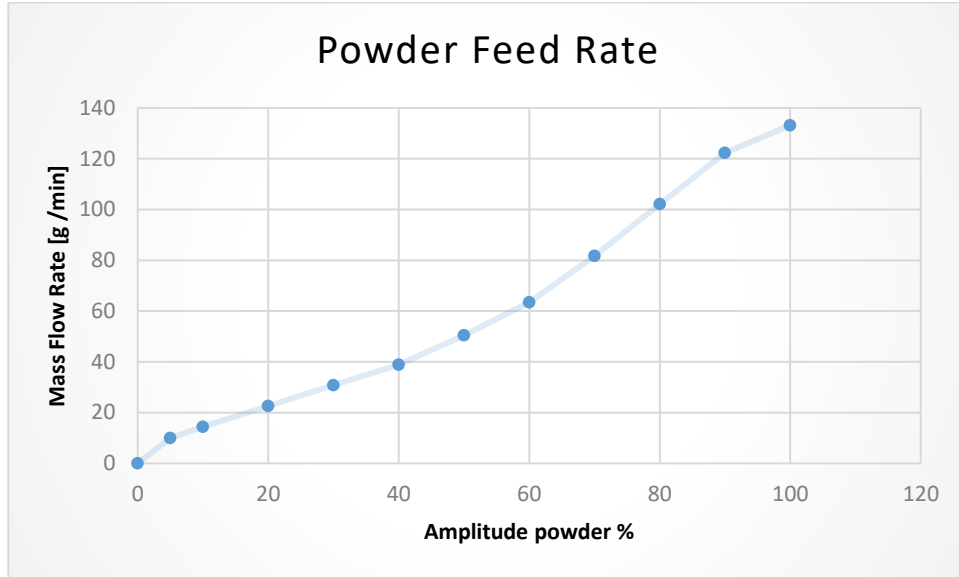
Figure 26. Powder Feed Rate of René 65

## 4.2.1.1 Methodology

Figure 27 shows the methodology used for LP-DED process based on the geometrical needs of thin blades wall. This method is structured into four stages: previous characterization, exploratory stage, experimental stage and rebuild. Previous characterization is a common stage for all AM samples, basically consists in a microstructural characterization. The exploratory stage begins with some combination of parameters in the single beads deposition, due to a geometrical characterization (cross and top view) and visual inspection some parameters were selected to try in single layer deposition.

A fixed hatch spacing of 0.7 mm was selected and a combination between power and travel speed was used, specific deposition features were analyzed such as discontinuities, dilution, layer slope, height, width and the parameters refined are the input of experimental stage. Multilayer depositions are made in this stage combining power, travel speed and rotation sequence each one with two values. Finally, the best parameter is used for rebuilding a wall on a sample of GTD 111 with each process.
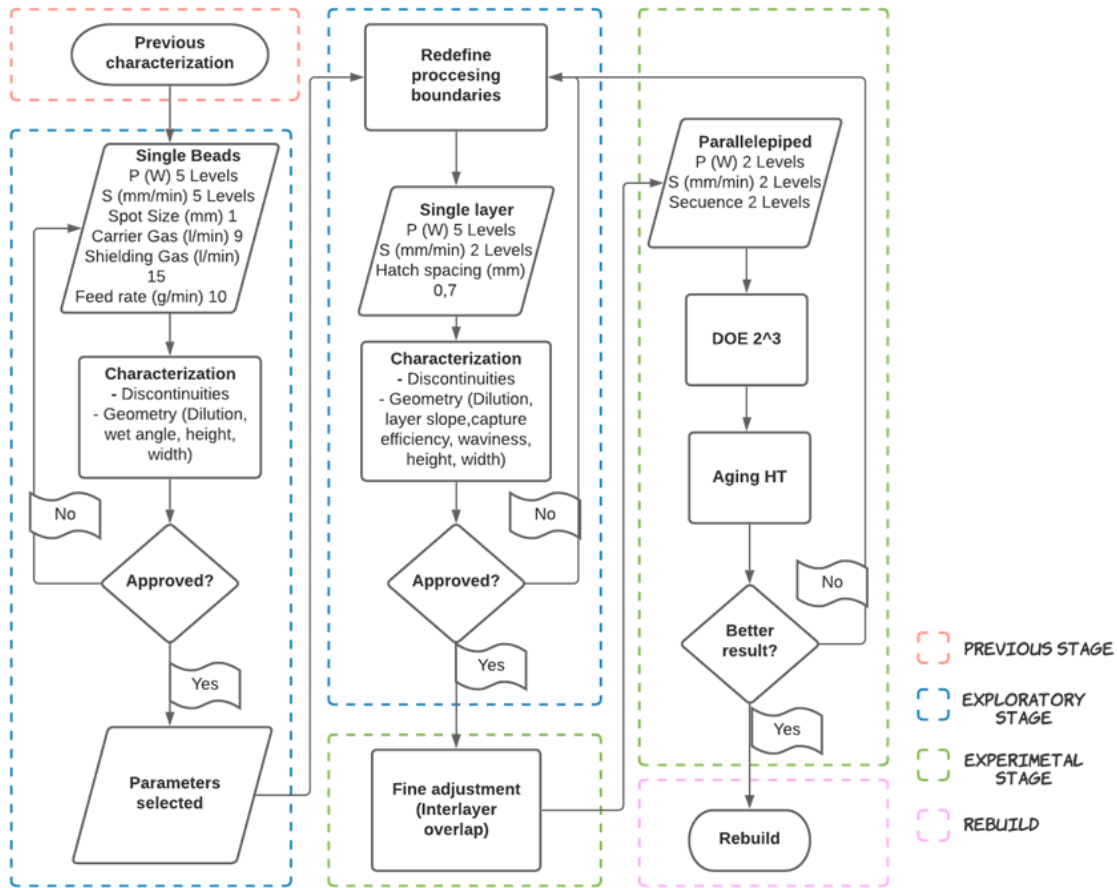
Figure 27. Flowchart methodology L-DED

## 4.2.2. L-PBF

Laser Powder Bed Fusion (L-PBF) experiments were carried out in a Concept Laser Mlab machine owned by The Ohio State University (OSU). Figure 28 shows the experimental setup, a cabinet where is done the AM process has a controlled atmosphere connected to Argon cylinder. Laser system is a fiber laser with 100 W maximum, max. travel speed of 7 m/s and a fixed layer thickness of 25 μm. This device has a build dimensions of 90 x 90 x 80 mm this indicates that the parts to be printed are small in size. Technical data is reported in appendix II.

The 3D design is loaded into a software called Magic, where the orientation of the part, the addition of supports and other adjustments are made before configuring the Mlab concept. Since the machine is not designed to carry out repairs, it was necessary a customized build plate. The 3D drawing must be overlapped to the build-plate manually. The dimensions of build plate must be rectified to ensure the correct alignment of the blade used to spread material.

Figure 28. Experimental Set-up L-PBF at Ohio State University


Figure 29 shows the inner of the machine with three different volumes from left to right are the powder reservoir, build plate, and excess powder collector. It is appreciated that the customized build-plate was made to be able to print on the specimens of the first stage blades.


Figure 29. Inside of L-PBF machine at OSU

## 4.2.2.1. Methodology


A similar methodology used in LP-DED was done for L-PBF. The exploratory stage has the objective to develop parameters that will be used in later stages. Top view and cross-section

analysis were carried out to find stable depositions, after that a porosity measurement was done for selecting the parameters to use in exploratory stage. In this part, the variables of power, travel speed and rotation between layers are combined with two different values for building parallelepipeds. After a visual inspection, microstructure analysis and microhardness testing was selected the best combination of parameters to perform the rebuild stage. In the last stage, two different printing were carried out: 1) restoration of a thin wall of squealer tip and 2) printing a complete first stage blades with René 65 powder.

## 4.3. Materials Characterization

### 4.3.1. Chemical composition

The chemical compositions were measured using optical emission spectroscopy (OES). The OES instrument was an *AMETEK SPECTROMAX*. Sample preparation was done with 60-grit aluminum oxide abrasive paper. All chemical composition measurements are an average of three testing.

### 4.3.2. Phases and microstructure

Metallographic samples were prepared by sectioning using an *Allied Techcut 5,* a linear precision sectioning saw. The saw was set to 3000 rpm and a feed rate up to 0.25 in/min. Each sample was mounted in Bakelite using a *Leco Instrument PR36* compression mounting press and grinding in successive steps using 240, 400, 600, 800, and 1200-grit SiC abrasive paper. Samples were polished until 1 μm using a *Pace Technologies Nano 1000T* machine and for EBSD testing were placed on a vibratory polisher using 0.05 μm colloidal silica.

The polished samples were etched with Marble´s etchant (50 ml HCl, 50 ml $H_2O$ and 10 g $CuSO_4$) for a few seconds to reveal the microstructure. OM is conducted using an *Olympus ® GX53* inverted microscope with PAX-it!™ 2 V1.5.1.0 software*.* To characterize geometrical features of deposits and microstructures is used an image analyzer software called *MIPAR.* SEM testing were carried out on a *Thermo Fisher Scientific Quattro S* equipped with EDS. Electron backscattered diffraction (EBSD) utilized an *EDAX® high-speed Hikari* camera and using *EDAX OIM DCv7.3.1 software*. The samples were positioned at a 70° tilt from horizontal. The working distance was 20 mm, 0.5 mm step size, the accelerating voltage was 20 kV, and the beam current was set to 13 nA.

### 4.3.3. Microhardness

Microhardness measurements are performed using an auto-microindentation hardness indenter *Leico AMH55*. A load of 300 Kgf is applied smoothly and a spacing of 2.5 times of indentation is maintained between indentations according to ASTM E 384. Some hardness samples were selected to do a mapping plot in MATLAB.

# 5. RESULTS AND DISCUSSION

## 5.1 Characterization of blades degraded in service

Microstructural characterization of degraded samples was performed near to the squealer tip of the blades at the center of the sample because it is the area of greatest repair. This section is divided in: (i) OM analysis, to characterize microstructural features such as carbide segregations, eutectic phases, pores and solidification mode in as-cast condition; (ii) SEM was used to identify size, distribution and shape of the precipitate γ'. Area fraction measurement was carried out for each blade before and after heat treatment; and (iii) EDS analysis was performed on different carbides found to detect their main components and identify what kind of carbide is.

### 5.1.1 Light Optical Microscope (LOM) and Hardness Characterization

The blade results were similar for both components (Blades 1 & 2) and are presented below. Figure 30 shows a series of LOM images. Figure 30A displays a polished sample (unetched) with the presence of carbides (C) and pores (P) characteristic of the casting condition. Figure 30B shows a primary carbide in high magnification with blocky shape. It is noteworthy the high number of microstructural defects such as composition inhomogeneities (eutectic γ/γ' phase) and pores at the matrix. Figure 30C provides a representation of the different phases observed in all the samples. Eta phase ($Ni_3Ti$, $D0_{24}$ crystalline structure) platelets were found intragranular, presumably following a decomposition sequence from MC and $M_{23}C_6$ carbides (Choi, 2008). Pores and carbides are found mostly at the interdendritic zones. Figure 30D shows blocky and other script-like carbides, according to Li et al. the transformation of carbides is induced by increasing the carbon content and cooling rate (Li, 2014).

Hardness measurement of Blades 1 and 2 after service have similar values around 400 HV.
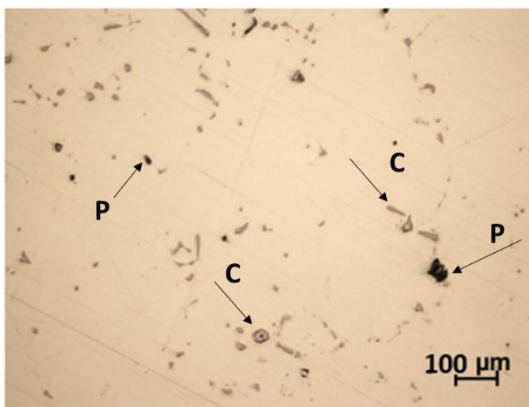


A) Pores and carbides present in matrix
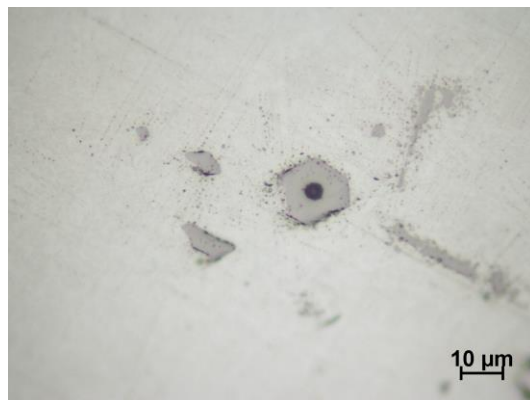


B) Blocky shape of carbide
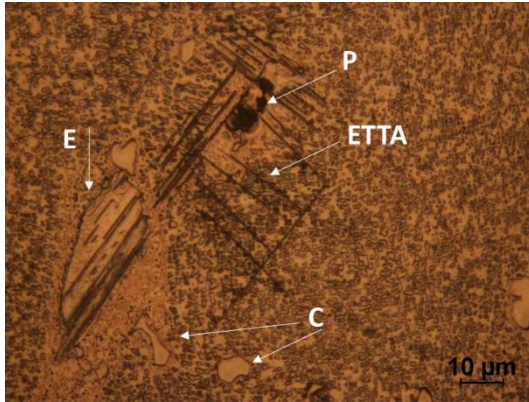
C) Carbides, eutectic phase and, eta phase      D) Some carbides
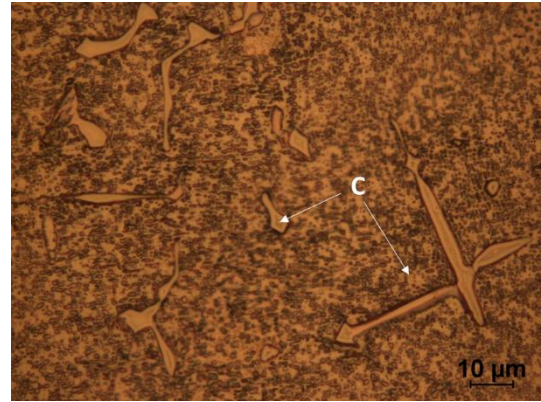
Figure 30. Optical microscopy images of blades

## 5.1.2 SEM characterization

In Figure 31, it is possible to observe the dendritic and interdendritic areas at low magnification. Interdendritic area has more fraction of γ' and dendritic arms are spaced approximately 50 µm between them due to the slow cooling rate in its manufacturing process, this fact affects the segregation rate, and it is an explanation of the high number of carbides in the microstructure. The elements added to the alloy typically show a preference to which phase they partition during solidification. Co, W and Re have been shown to partition to the dendrite core, while Ni, Ta, Ti, and Al tend to segregate to the interdendritic region (Fela, 2000) (Durand-Charee, 1997).

γ' dendrites are the first solid to form, typically at temperatures just below the liquidus temperature, and the solid that forms in the interdendritic region is the last to solidify at a temperature below the solidus due to elemental segregation during solidification (Gell, 1987) (Willis, 1991).
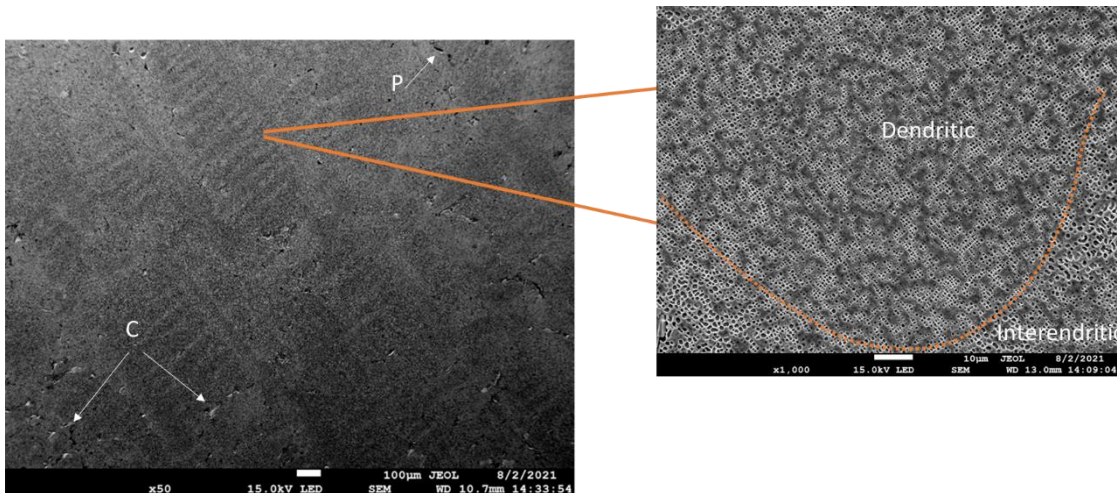
Figure 31. Dendrites in GTD 111

Figures 32A and 32B represent the typical scenario found at the grain boundaries: the islands of eutectic phases are concentrated in the borders as well as the carbides. This makes them a weak zone where premature failure can occur due to a lower melting point. Figure 32C shows the detail of an eutectic region and the distribution of γ' precipitates into the γ matrix can be seen in figure 32D. The larger rectangles are the primary γ' precipitates and the smaller ones are secondary γ'.
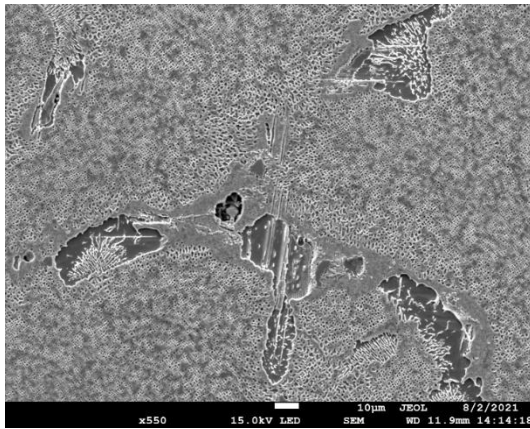


A) Eutectic islands
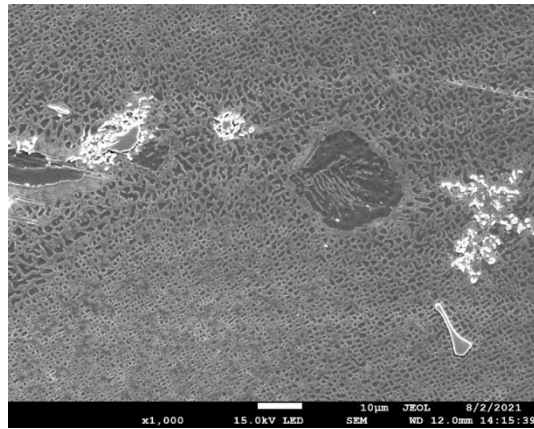


B) Grain boundaries
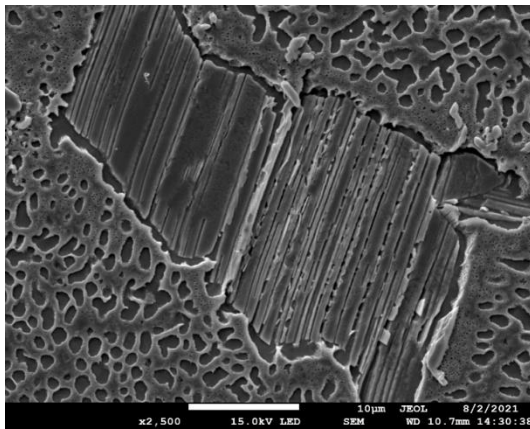


C) Eutectic phase
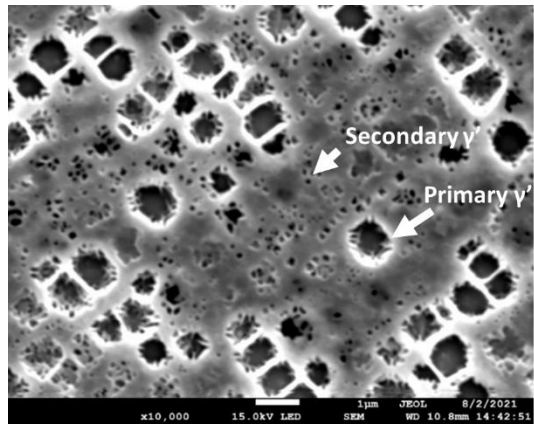


D) Gamma prime and matrix gamma

E)

Figure 32. SEM images of blade after service

## 5.1.3 EDS characterization and percent of Gamma prime

The mapping of chemical composition in Figure 33 shows that eutectic phase is enriched in Ni and Ti and depleted of Cr, which is consistent with its stoichiometry formula ($Ni_3Ti$). The MC carbides, on the other hand, are rich in Ti and W. The eutectic phase found in Figure 33C shows that the elementary elements are the same as that found in Figure 33a. In this

case, script carbides or "Chinese script" are observed with long arms along to the grain boundaries enriched to Ti and Ta, which could promote the nucleation of cracks due to impaired mechanical properties (Sun, 1999).
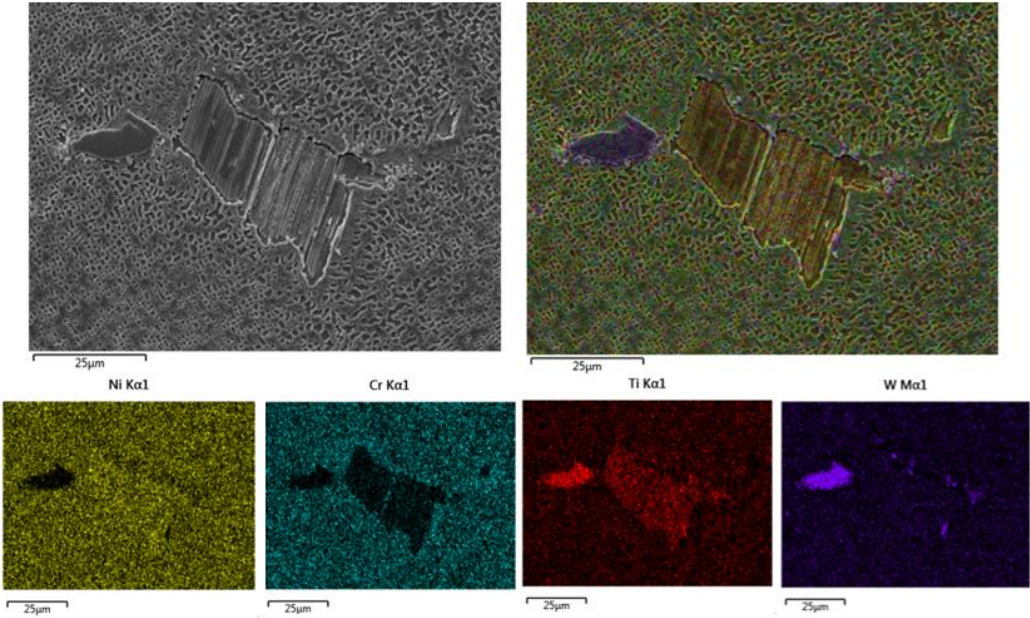


A)
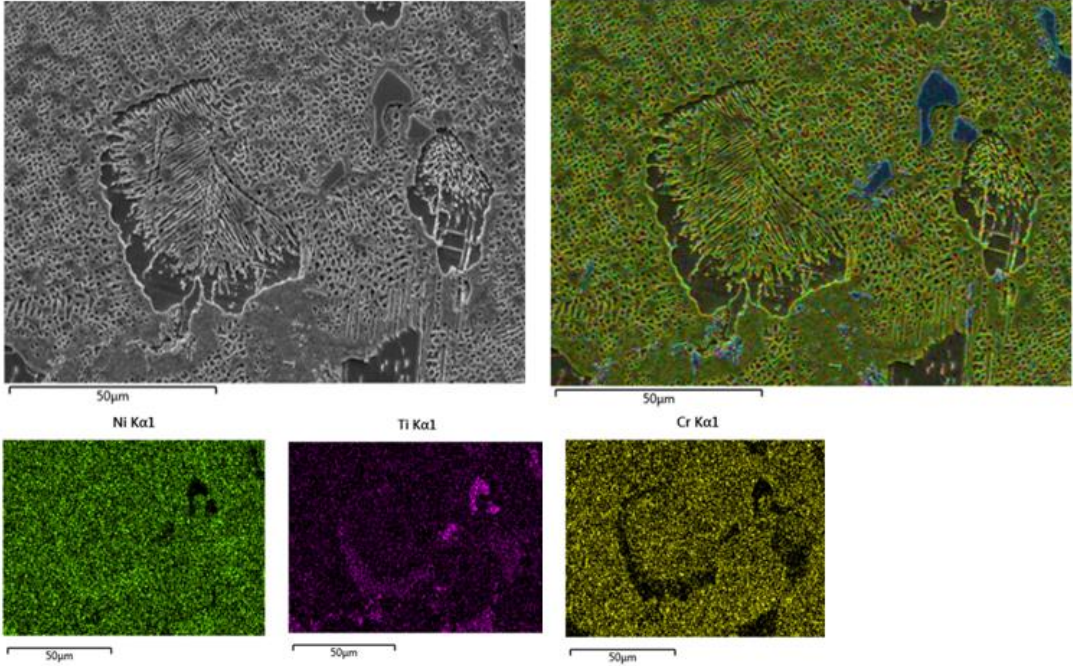


B)
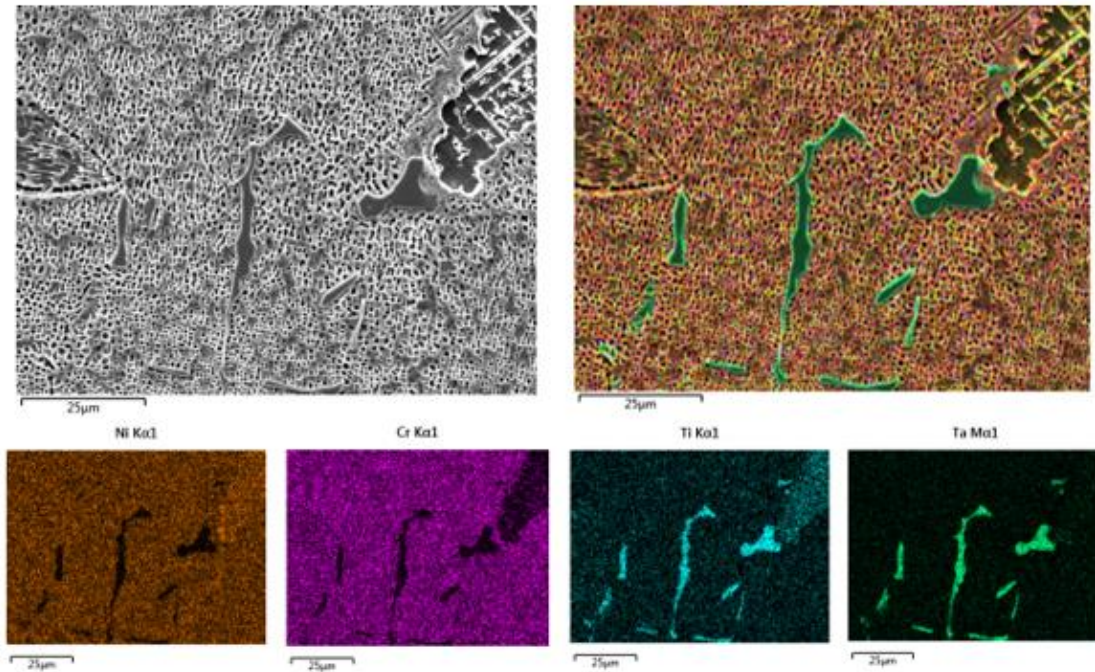
C)

Figure 33. EDS compositional maps of the microstructure of a degraded blade

An analysis of the spectrum was carried out to know the proportion of elements in the script carbides, the results are shown in Figure 34 and indicate that the typical elongated shape is consistent with TiC and TaC stoichiometry.

| Element | Weight% | Atomic% |
|---------|---------|---------|
| C K     | 11.31   | 49.62   |
| Ti K    | 24.69   | 27.17   |
| Cr K    | 1.47    | 1.49    |
| Co K    | 1.02    | 0.91    |
| Ni K    | 4.89    | 4.39    |
| Ta M    | 43.48   | 12.66   |
| W M     | 13.14   | 3.77    |
| Totals  | 100.00  |         |
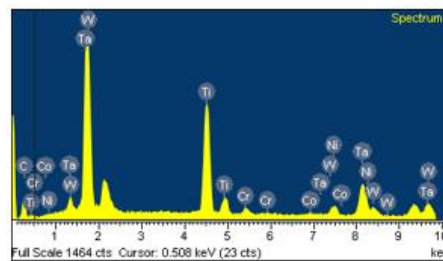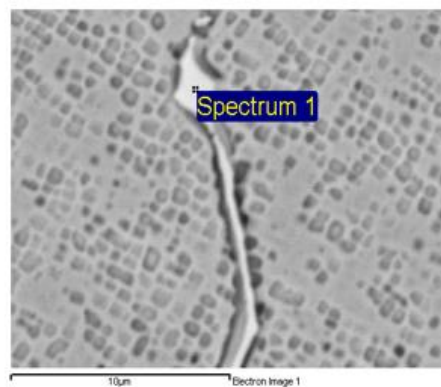
Figure 34. Micro-chemical composition of script carbide

Area fraction of gamma prime measurements were performed by MIPAR software (Figure 35). The average of area fraction in blade 1 was 30.91 ± 1.13% and 33.93 ± 1.56% in blade 2. The average size was similar in both blades, 0.32 µm$^2$ and 0.35 µm$^2$, respectively. The increase in the fraction of area and size are justified due to the greater number of hours in service of blade 2.



SEM X5500 SE                              Threshold gamma prime
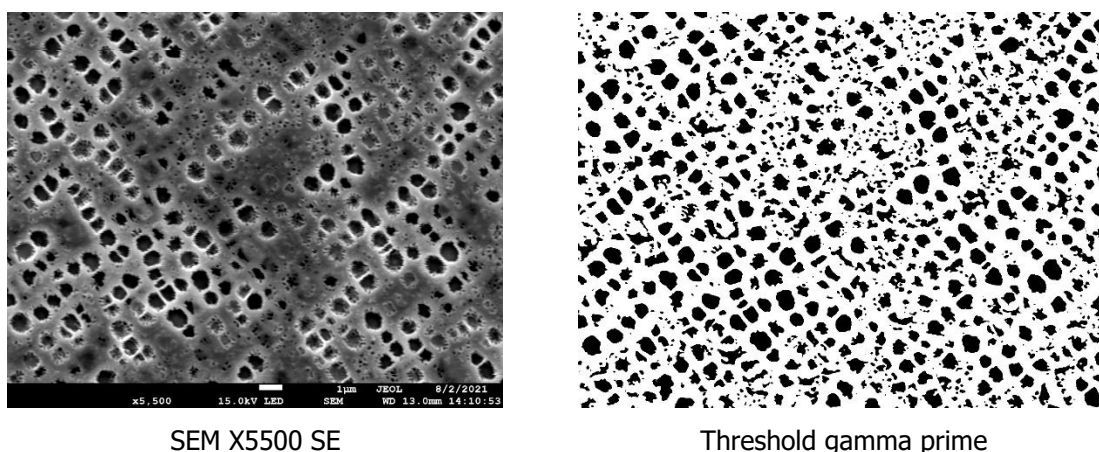
Figure 35.  Gamma prime area fraction measurement

Table 7 summarizes the area fraction of gamma prime and the average size of gamma prime obtained for the Blades 1 and 2, respectively. For each image was calculated the average size of all γ' precipitates presented. The averages and standard deviations are calculated for eight images analyzed.

Table 7. Area fraction of Gamma prime in degraded blades

| Image | Blade 1 | | Blade 2 | |
|---|---|---|---|---|
| | Area Fraction (%) | Size (um$^2$) | Area Fraction (%) | Size (um$^2$) |
| 1 | 30.08 | 0.28 | 35.51 | 0.32 |
| 2 | 31.01 | 0.27 | 33.63 | 0.36 |
| 3 | 29.80 | 0.28 | 31.80 | 0.31 |
| 4 | 32.30 | 0.32 | 34.36 | 0.34 |
| 5 | 28.22 | 0.34 | 30.72 | 0.36 |
| 6 | 27.85 | 0.37 | 29.29 | 0.38 |
| 7 | 33.64 | 0.35 | 36.67 | 0.38 |
| 8 | 34.38 | 0.31 | 39.48 | 0.39 |
| Average | 30.91 | 0.32 | 33.93 | 0.35 |
| SD | 1.13 | 0.02 | 1.56 | 0.02 |

## 5.2 Effect of heat treatment of degraded blades

Microstructural characterization of heat-treated degraded samples was performed near to the tip of the blades. This section is divided in OM testing, SEM testing and measurement of area fraction for each blade after the partial-solution heat treatment.

### 5.2.1 OM Characterization

Figure 36 shows a series of OM images analyzed from transversal and longitudinal views. Figure 36A and 36B display polished, unetched samples and the presence of carbides and pores is evident. On the other hand, Figures 36C and 36D show the images of etched samples. In both cases it is remarkable the high quantity of carbides along the grain boundaries. In Figure 36D it is possible to see the interdendritic spaces. All the samples inspected were free of cracks.
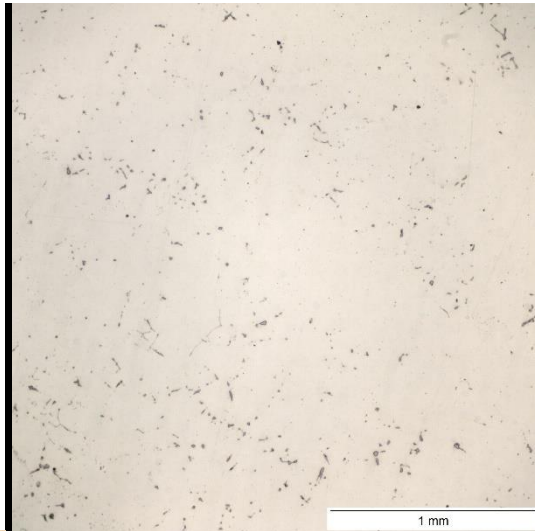


A) Pores and carbides present in the matrix. Transversal view.
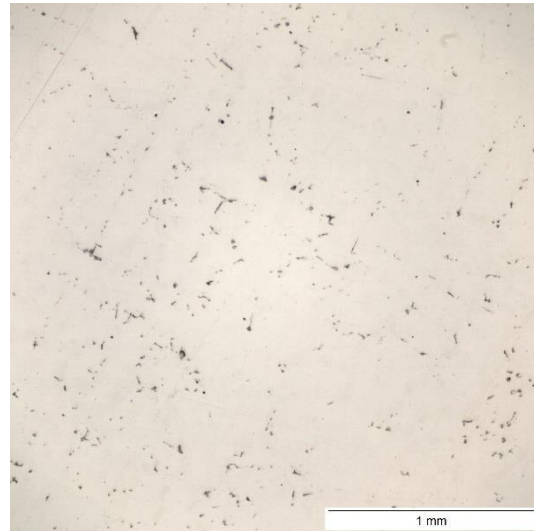
B) Carbides present in the matrix. Longitudinal view.
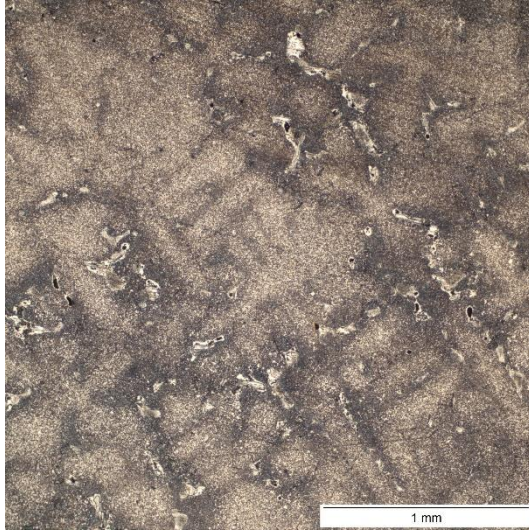
C) Carbides.Transversal view.    D) Carbides. Longitudinal view.
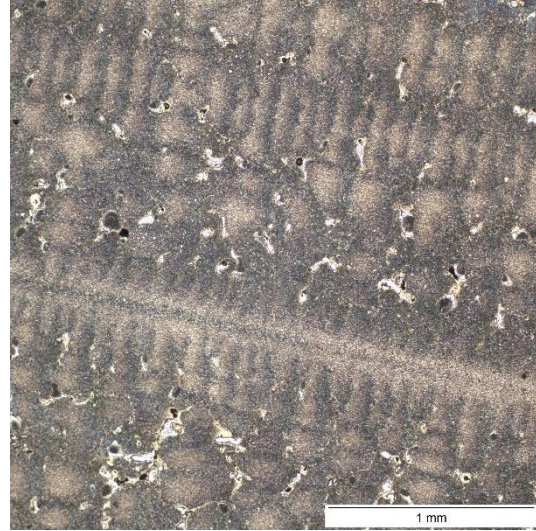
Figure 36. OM images for heat-treated samples

## 5.2.2 SEM characterization and percent of gamma prime

Figure 37 shows the results of a deeper microstructural analysis of blade 1 using SEM. The presence of carbides along grain boundaries is more notable than before of the heat treatment, as shown in Figures 37A and 37B. Size, shape and distribution of carbides and γ' were altered by the slow cooling rate inside the furnace (Figures 37C and 37D). It shows that the morphology changes from cuboids to irregular-shaped flower-like one No cracks were found after thermal cycling, however area fraction of γ' increased to 43.34% with an average size of 0.43 μm. All results are shown in Table 8.
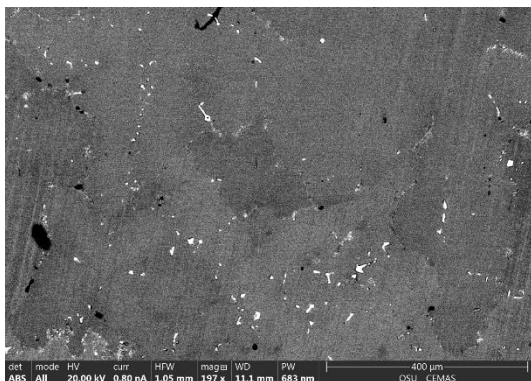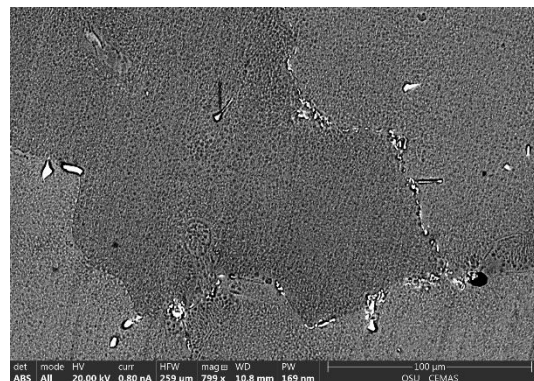


A) SEM 200X    B) SEM 800X
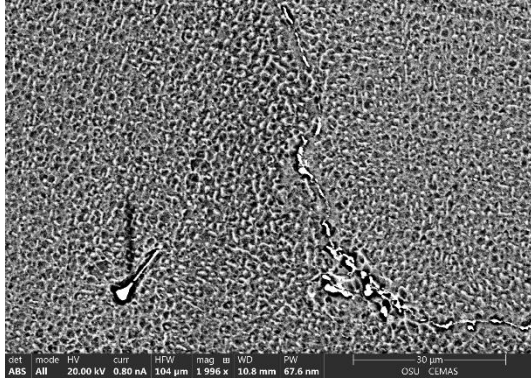
F) SEM 2000 X
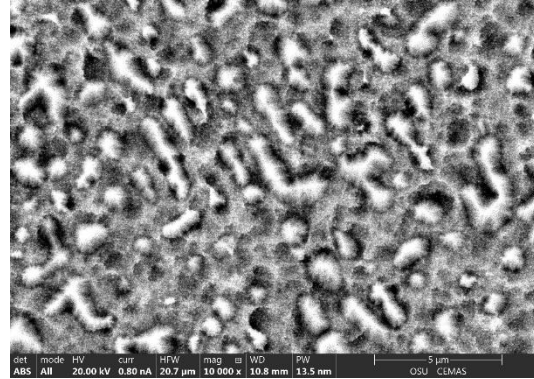


G) Gamma prime and matrix gamma 10000 X

Figure 37. SEM images of heat-treated samples

Table 8. Measurement of gamma prime heat-treated blade

| Image | Area Fraction (%) | Size (um) |
|---|---|---|
| 1 | 45.36 | 0.45 |
| 2 | 41.98 | 0.44 |
| 3 | 39.69 | 0.46 |
| 4 | 46.51 | 0.40 |
| 5 | 43.87 | 0.45 |
| 6 | 45.12 | 0.43 |
| 7 | 40.93 | 0.43 |
| 8 | 43.25 | 0.39 |
| Average | 43.34 | 0.43 |
| SD | 2.35 | 0.03 |

## 5.2.3 Conclusions about the heat treatment effectivity

- Solution heat treatment prior to repair via thermal processes is an important issue to recover the coherence between of γ-γ' of the parent metal.

- The cooling rate plays a key part to determine the main features of the microstructure such as distribution, size and area fraction of gamma prime crystals. Using lower cooling rates, the shape of the γ' precipitates will tend to be more cuboidal

- The hardness of the material decreased after partial solution heat treatment, reaching 375 HV.

- Any crack was developed after heat treatment.

- Generally speaking, after heat-treatment GTD 111 increased its area fraction of gamma prime in 39% and the average size of the phase precipitates is 32% larger than in untreated samples.

# 5.3 L-DED Manufacturing

## 5.3.1 Exploratory stage

Figure 38 shows different single beads tried in preliminary test to understand the processing conditions. The purpose of the preliminary test is to provide information about the powder used in the experiment and plan for subsequent stages. The substrate used was SS 316. In Table 9, it is possible to see the different combinations of power and scanning speed used in the preliminary test. The numbering of Figure 38 is according to Table 9.
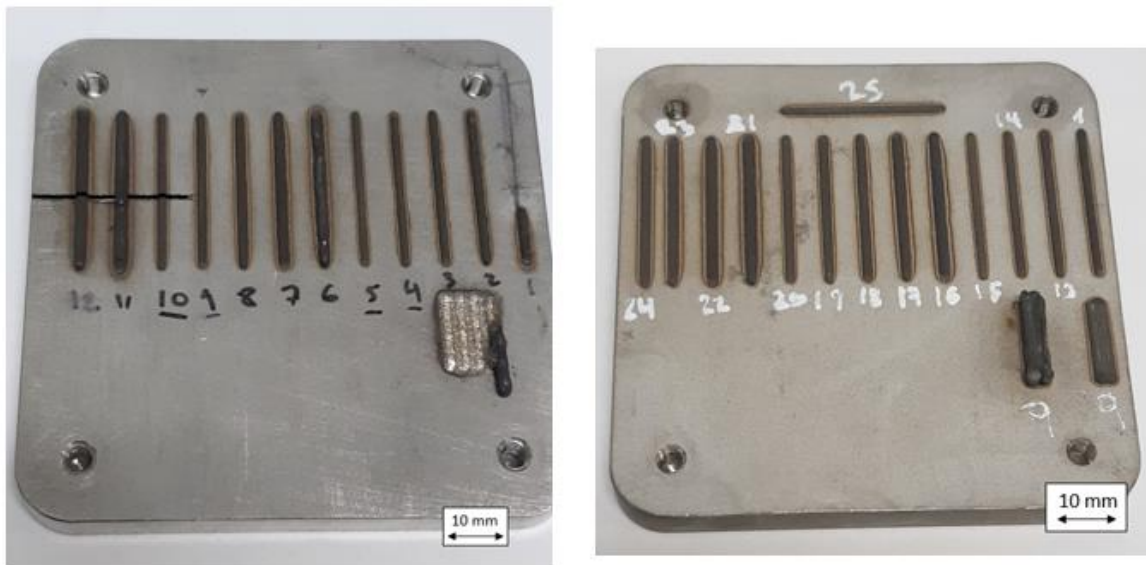


Figure 38. Preliminary test René 65 powder on 316 substrate
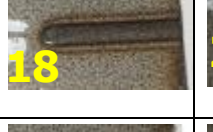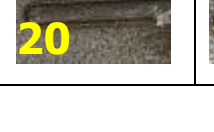
Table 9. Preliminary test 316R65 LP-DED

| $P_{(W)}$ / $V_{(mm/min)}$ | 400 | 500 | 600 | 700 | 800 |
|---|---|---|---|---|---|
| 180 | 1 | 6 | 11 | 16 | 21 |
| 250 | 2 | 7 | 12 | 17 | 22 |
| 350 | 3 | 8 | 13 | 18 | 23 |
| 450 | 4 | 9 | 14 | 19 | 24 |
| 550 | 5 | 10 | 15 | 20 | 25 |

The laser power and travel speed have a wide range with five levels for each one and the feed rate is fixed in 18 % of amplitude powder (10 g/min). Spot size of 1 mm is kept constant to obtain productivity and resolution in deposits. Based on the deposit shown in Figure 38, an evaluation of appearance, convexity, detachment, irregularities and other defects was performed, and the findings are shown in Figure 39.

Single bead is the most basic geometry, which makes it an ideal approach to start a methodology to develop parameters for a repair. An analysis in top and cross section is performed in all experiments to obtain the region of a stable process. Table 10 shows the top view of the single beads printed by L-DED with SS 316 powder. Stability is appreciated along the beads in the range of parameters of 4, 5, 9, 10, 13, 14, 15, 18, 19, 20, 23 and 24. No cracks were found by visual inspection.

Table 10. Preliminary test longitudinal beads 316R65 LP-DED

| P(w) / V(mm/min) | 400 | 500 | 600 | 700 | 800 |
|---|---|---|---|---|---|
| 180 | 1 | 6 | 11 | 16 | 21 |
| 250 | 2 | 7 | 12 | 17 | 22 |
| 350 | 3 | 8 | 13 | 18 | 23 |
| 450 | 4 | 9 | 14 | 19 | 24 |
| 550 | 5 | 10 | 15 | 20 | 25 |

A cross section assisted by OM to evaluate regular melt pools was performed in all samples and shown in Figure 39. Convexity is the aspect ratio between width and height of the bead. High aspect ratio must be avoided. Dilution is other important parameter to be controlled in nickel alloys because it is essential to reduce heat input into the substrate. Porosity was determinated qualitatively in this stage. Parameters with a range between 350-550 mm/min and 400-600 W have a good appearance.
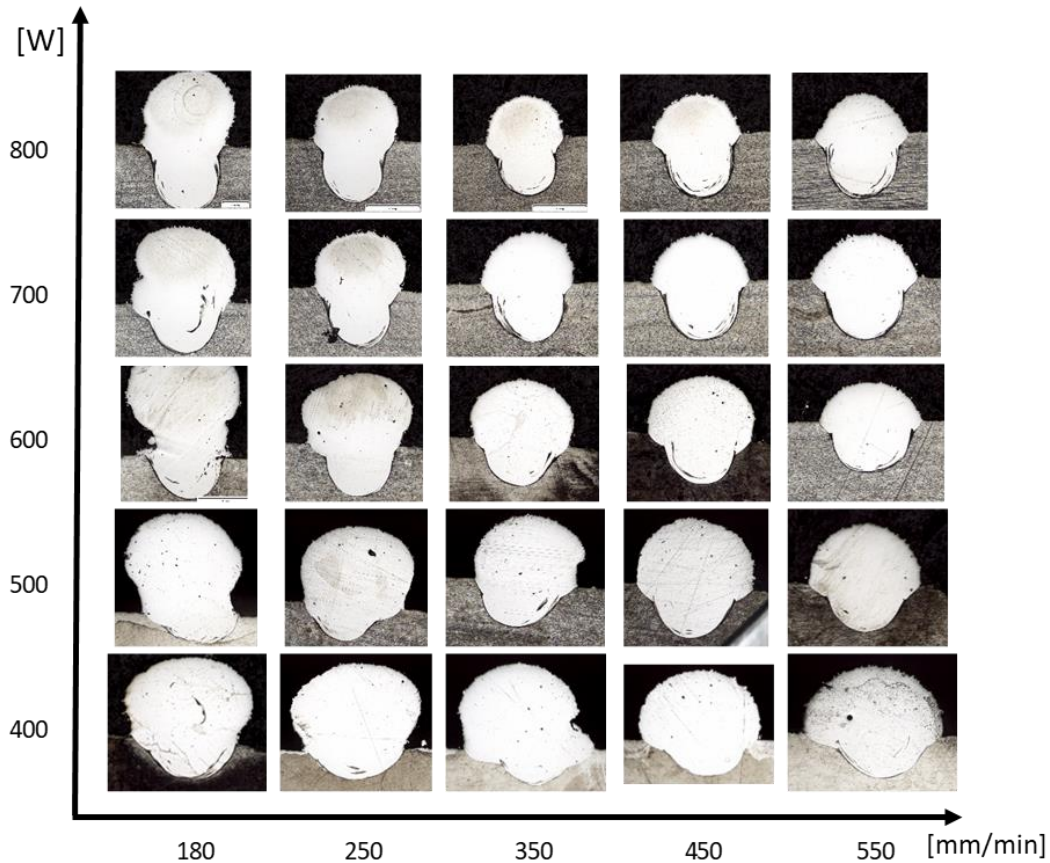
Figure 39. Cross section single beads on SS 316

The results are presented in the form of tabular maps of power vs travel speed (Figure 40). The legend represents all the characteristics found in the bead's examination. Green color represents the best parameters and read color the worst; any detachment was discarded in parameters selection. High dilution is displayed as yellow color. Unstable tracks both due to the balling effect and changes in height are classified with blue. The region to be studied is colored by green and represents the combination of parameters of 600 W–350 mm/min, 600 W–450 mm/min, 500 W–450 mm/min, 500 W–550 mm/min, 400 W–450 mm/min and 400 W–550 mm/min. The geometries found for low power and travel speed of 450 and 550 mm/min have good results, for this reason it is desired to test the combination of parameters of 300 W.

Acceptance criteria are defined in order to select a set of parameters to obtain a specific geometry. Green color describes deposits with low aspect ratio, no defects, low wet angle (contact angle < 90°) and a dilution less of 40%.
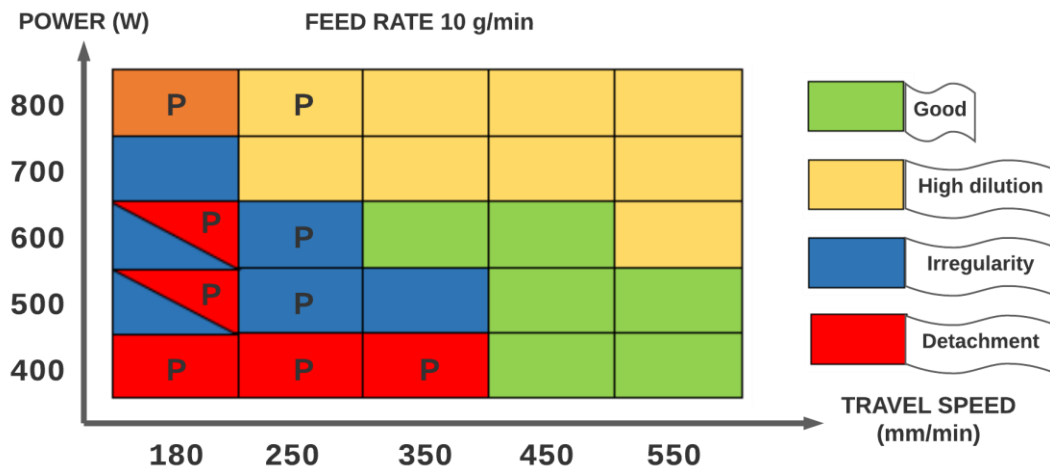
Figure 40. Window LP-DED process parameters

A final test on the 316 was carried out. A single layer with 500 W-450 mm/min was printed with the René 65 powder composed by four beads as shown in Figure 41. The objective of this testing is to explore the behavior of a printed layer with a hatch spacing of 0.7 mm. The defects observed in the single bead will not necessarily be repeated in a building part. A free-defect deposit, with acceptable dimensional stability was obtained. The results of the geometric characteristics are presented in the Table 11. The single layer has a reinforcement of 0.7 mm, 34.5% of dilution and a layer slope of 2° between the first and last peak. Acceptable range values of process parameters depend on the application and material. GTD 111 repair must have deposit free of cracks and a stable roughness. The value of dilution to obtain a quality printing with GTD 111 and René 65 are not available in literature. Almost all of the previous studies are focused in cladding, and not to multilayer deposition. According to the applications of both materials, dilution is not a restricted parameter.
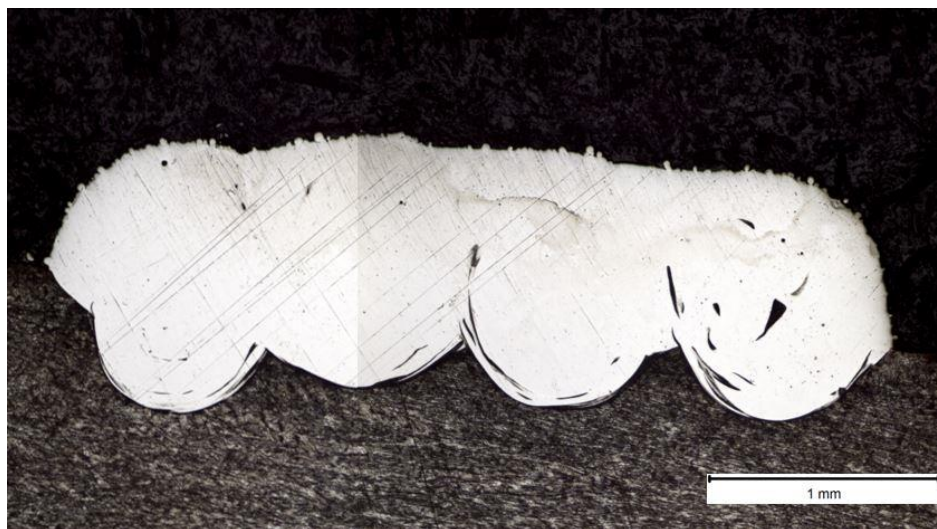


Figure 41. Single layer of René 80 on 316 substrate

Table 11. Measurement of single layer R65 on 316.

| | Single layer R65-316 | | | | | |
|---|---|---|---|---|---|---|
| # | Width (mm) | Height (mm) | Penetration area (mm2) | Total area (mm2) | Dilution | Layer Slope (°) |
| 1 | 3.7 | 0.7 | 1.2 | 3.5 | 34.5 | 1.8 |

Once the behavior of a fraction of the combinations Power (P) vs travel speed (S) on SS 316 was established, the selected values were printed on the surface parallel to the squealer tip. The main objective was to test the parameters in the real material, and thus be able to determine the dilution and possible weldability problems that may exist in the different regions of the weld. Figure 42 illustrates the cross sections of the chosen parameters in the tabular map (Figure 40). In addition, some values with 300 W and 450 mm/min and 550 mm/min were tested and presented lower dilution and wet angles than other parameters.
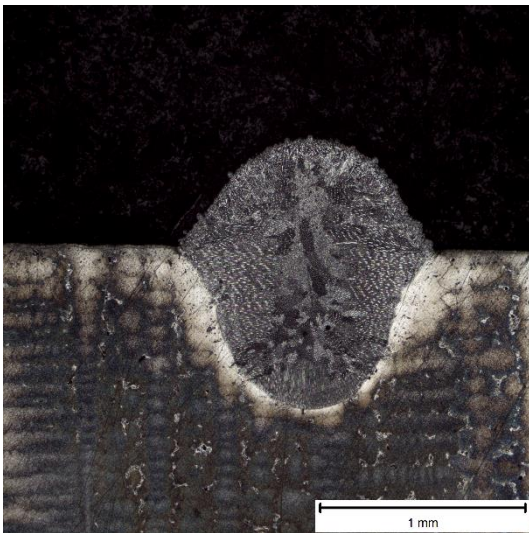


A)  #4 (400 W-450 mm/min)-50X
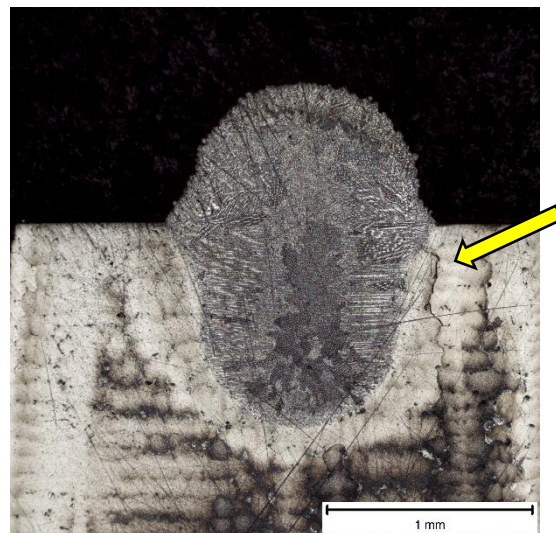


B)  #8 (500 W-350 mm/min)-50X
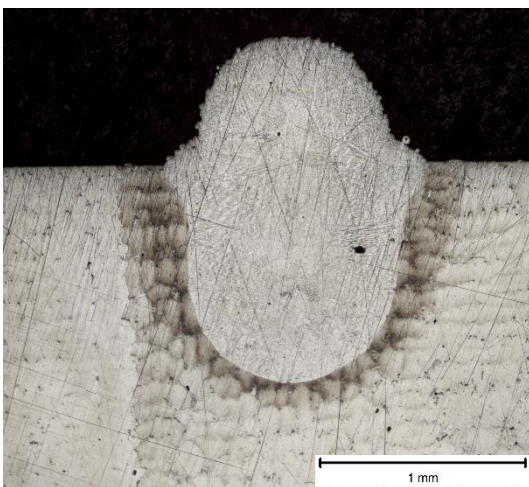
C)   #14 (600 W-450 mm/min)-50X
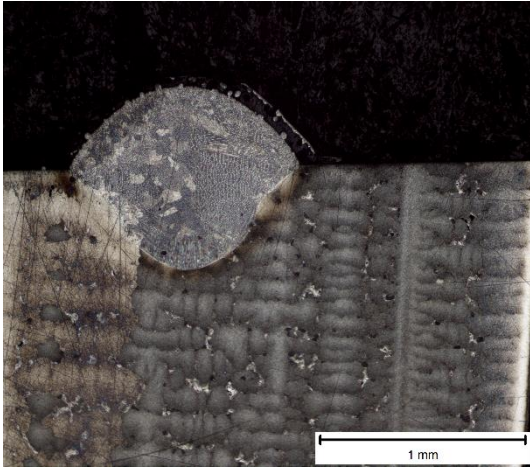
D)   #26 (300 W-450 mm/min)-50X



E)   #27 (300 W-550 mm/min)-50X

F)   #28 (350W-450 mm/min)-50X
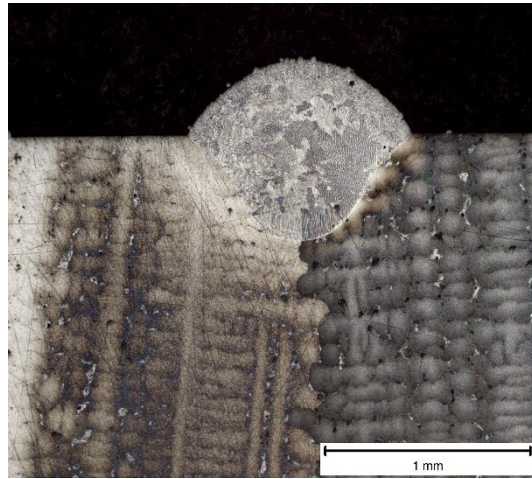


G)   #29 (350 W-550 mm/min)-50X
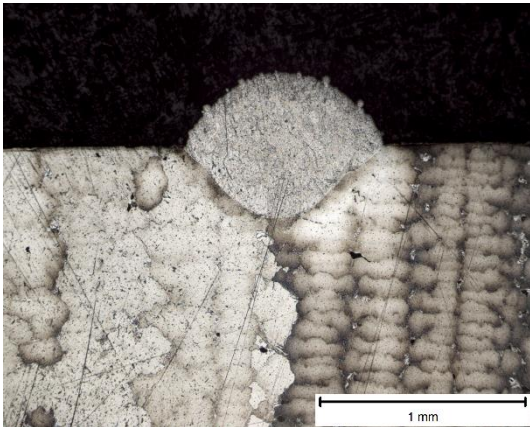
H)   #30 (250 W-450 mm/min)-50X
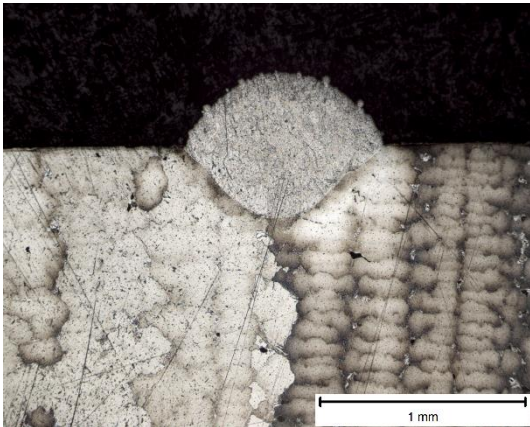


I)   #31 (200 W-550 mm/min)-50X

Figure 42. Cross-section of single beads of René 65 on GTD 111

Table 12 presents the measurements of single beads on GTD 111 and a reference figure. Generally speaking, parameters with power greater than 500 W present high dilution even a hot cracking phenomenon was observed in Figure 42B. It was discarded the successful parameter found on 316 SS, 600W-450 mm/min because it has a dilution of 67% presenting features totally different on GTD 111. Setting power less than 300 W for any speed value between 450 and 550 mm/min, lower dilutions and wetting angles were evidenced in the weld pool. Based on the measurements shown in the table, it is possible to choose the ideal parameters for a type of repair. For example, parameter #4 is a good candidate for good productivity and #31 could be used for high resolution and low dilution.



1: Reinforcement
2: Width
3: Penetration
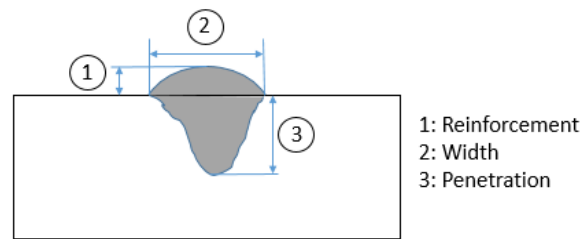
Table 12. Measurement of single beads deposited onto GTD 111

| Sample | Dilution (%) | Width (mm) | Depth (mm) | Ratio | Reinforcement (mm) | Cracks |
|---|---|---|---|---|---|---|
| #4 (400 W-450 mm/min) | 54.90 | 1.25 | 0.79 | 1.58 | 0.53 | No |
| #8 (500 W-350 mm/min) | 56.35 | 1.30 | 0.98 | 1.33 | 0.69 | Yes |
| #14 (600 W-450 mm/min) | 67.00 | 1.28 | 1.08 | 1.18 | 0.61 | No |
| #26 (300 W-450 mm/min) | 55.32 | 1.19 | 0.64 | 1.86 | 0.43 | No |
| #27 (300 W-550 mm/min) | 51.22 | 1.12 | 0.49 | 2.28 | 0.41 | No |
| #28 (350W-450 mm/min) | 55.46 | 1.20 | 0.73 | 1.64 | 0.47 | No |
| #29 (350 W-550 mm/min) | 55.21 | 1.16 | 0.61 | 1.90 | 0.45 | No |
| #30 (250 W-450 mm/min) | 56.12 | 1.10 | 0.52 | 2.11 | 0.37 | No |
| #31 (200 W-550 mm/min) | 43.00 | 0.97 | 0.34 | 2.85 | 0.30 | No |

The hot cracking detected in the application of 500W and low speed of 350 mm/min on the blade is presented in Figure 43. As is typical of liquation cracking, it originated in the heat-affected zone and propagated along grain boundaries. In this phenomenon typically MC or Laves phases could nucleate a crack due to lower melting points. This crack progresses easily across grain boundaries.
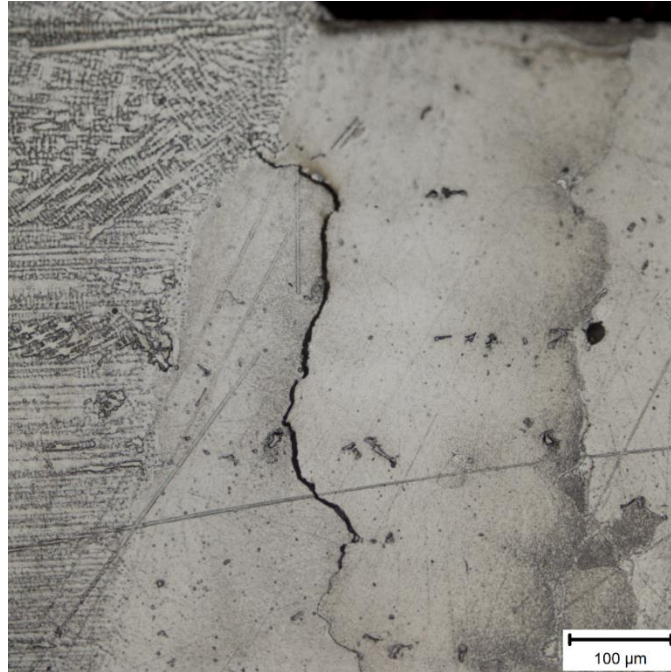
Figure 43. Liquation cracking of GTD 111 using René 65 powder.

Once the single beads were characterized, it was necessary to define if a value of 0.7 of hatch spacing was adequate for the programming of future deposits. For this reason, single layers were printed with the best parameters found from the single bead stage. Qualitatively, the beads with lower porosities, less slope between beads and an acceptable dilution were selected. Figure 44A shows on top view the deposits with different parameters according to Table 9; Figure 44B is a cross section analysis of 300 W-450 mm/min. It is worth noting the low porosity and the dimensional uniformity of the layer. Appendix III has more micrograph of other single layers.
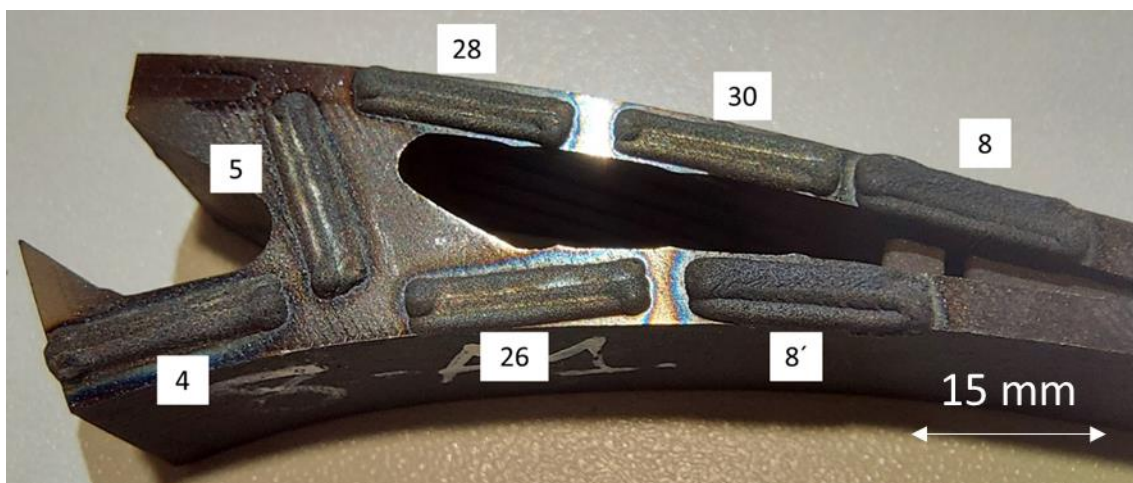


A. Single layer parameter selected L-DED.
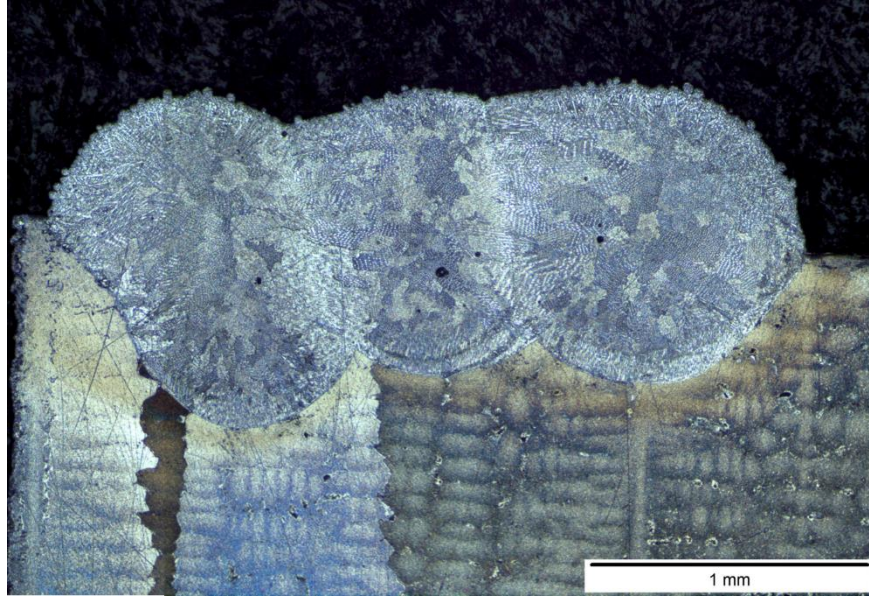
B. Cross-section of single layer #26 (300 W-450 mm/min).

Figure 44. René 65 Single layer deposited on GTD 111

In order to find the interlayer overlap, a multi-layer deposit was performed with the candidate values to be selected. It was possible to establish that 0.6 mm of interlayer overlap is good for obtaining an uniform deposit.
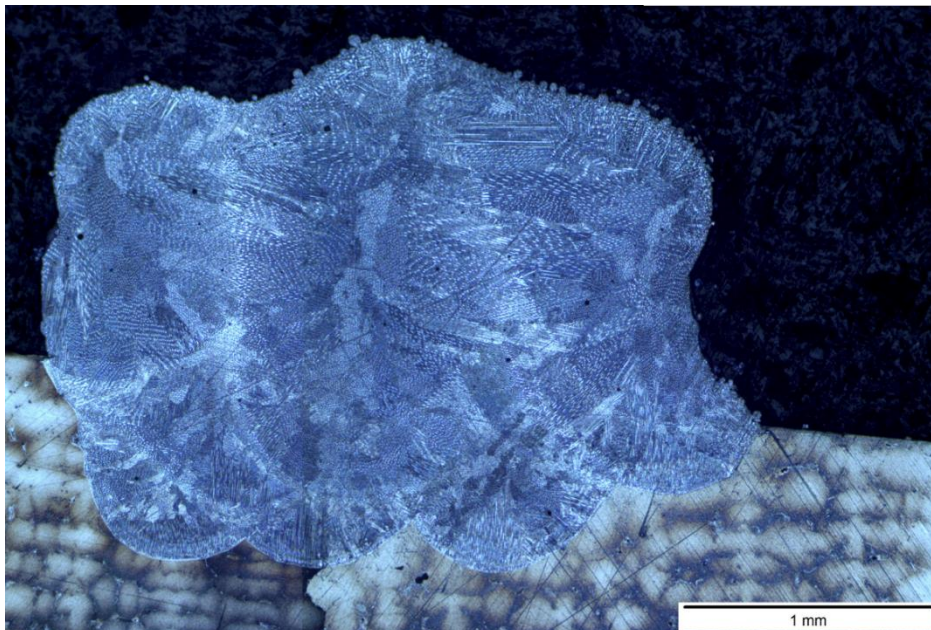


Figure 45. Multilayer deposited with 400 W – 450 mm/min

## 5.3.2 Experimental Stage

## 5.3.2.1 Visual examination

A schematic representation of the sequence path between layers is presented in Figure 46. The results of the exploratory stage are the input of the experimental stage as shown in Table 13. In this stage, three variables were tested (power, travel speed and rotation between layers) with two different values. Two replicates were made for each combination.
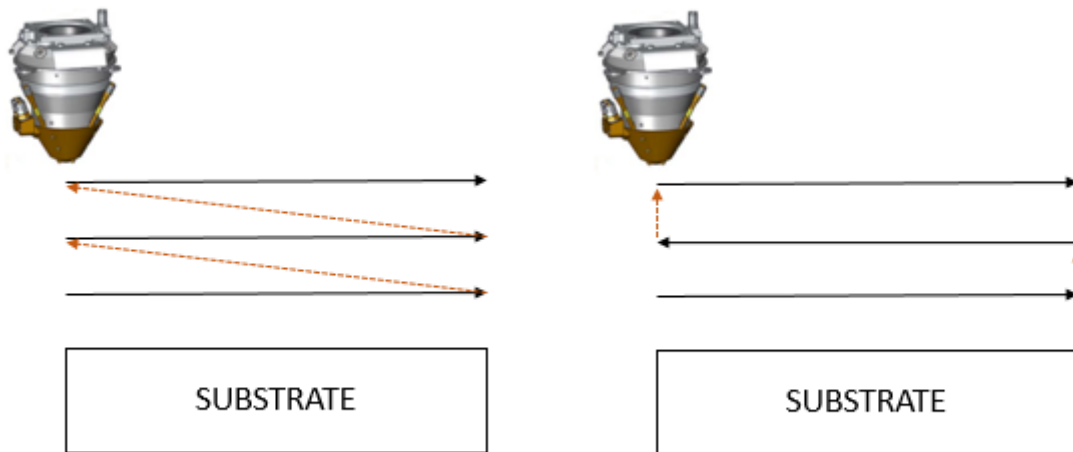


A) 0° of rotation between layers          B) 180° of rotation between layers

Figure 46. Schematic paths used in experimental stage
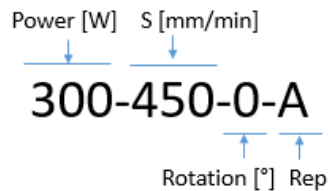


Table 13. Parameters used in experimental stage LP-DED

| Sample | Power (W) | Travel speed (mm/min) | Rotation (°) |
|---|---|---|---|
| 400-550-0 | 400 | 550 | 0 |

| 400-550-180 | 400 | 550 | 180 |
|---|---|---|---|
| 400-450-0 | 400 | 450 | 0 |
| 400-450-180 | 400 | 450 | 180 |
| 300-550-0 | 300 | 550 | 0 |
| 300-550-180 | 300 | 550 | 180 |
| 300-450-0 | 300 | 450 | 0 |
| 300-450-180 | 300 | 450 | 180 |

Figure 47 shows sixteen deposits of 15 x 3 x 3 mm printed on blade specimens manufactured in GTD 111. The parameters used are according to those shown in Table 9. In general, no detachments or defects were evidenced by visual inspection. The edges present more accumulation than the center of material due to the changes of directions produced in the corners. The programming of the deposits was done manually. A unique code was used for all the experiments, varying the values of the parameters for each case. The compilation of the coding programs is shown in Appendix IV. The selection of the starting point was aided by the camera that the equipment has (it is located at the desired point with great precision).
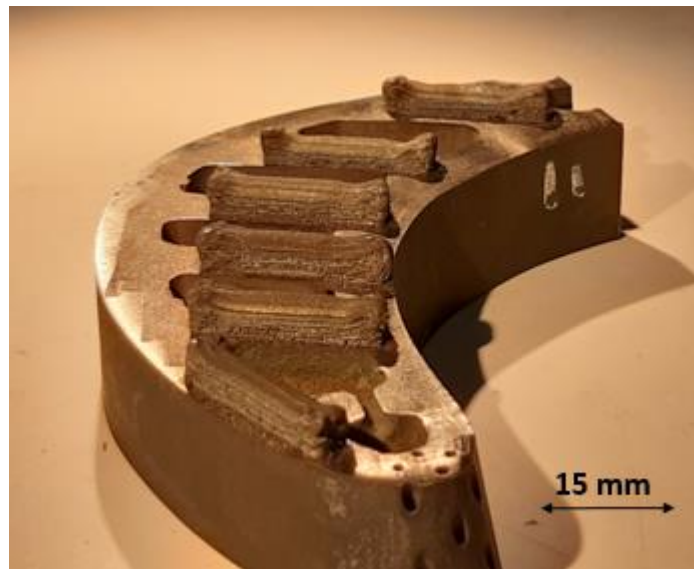


A)  Sample of GTD 111 printed by LP-DED

B) Sample of GTD 111 printed by LP-DED


C) Sample of GTD 111 printed by LP-DED

Figure 47. Deposits of Experimental Stage LP-DED

## 5.3.2.2 Cross sectional analysis for porosity measurement

In the central part of each built parallelepipedon, an analysis of the cross section was carried out (Figure 48A). The following Figures represent how the porosity was measured for each specimen. Firstly, the largest area that can be covered in the micrograph is selected (Figure 48B) to apply a threshold (Figure 48C) in order to be able to measure the area fraction of pores in the image. The rest of the images of the unetched samples can be seen in Appendix VII. The results of the porosity measurements are represented in Figure 48, where the percentage of porosity is associated with each sample. The plot shows that mostly the samples with rotation of 180° between layers have lower porosities. The values are generally low, lesser than 0.35 %.
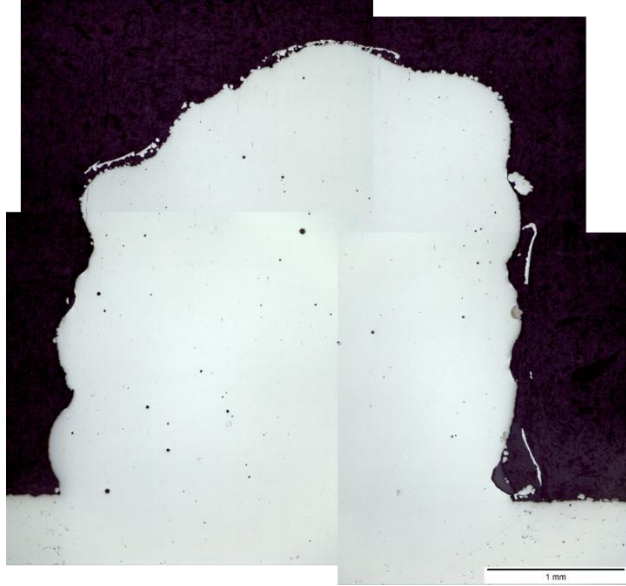
A) 400-550-180-B
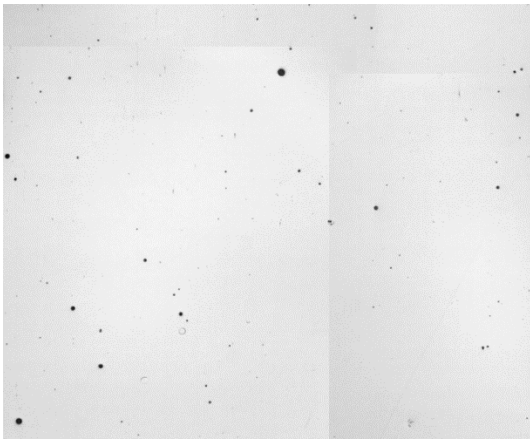


B) Area selected for measurement



C) Binarized image

Figure 48. Measurement of porosity in DOE samples LP-DED
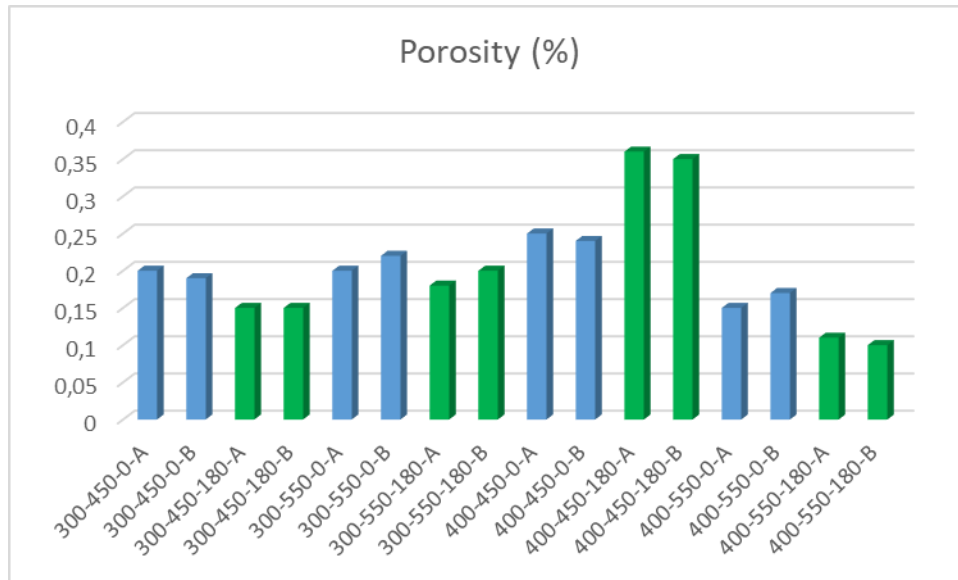
Figure 49. Porosity VS sample LP-DED

## 5.3.2.3 LOM Characterization

Figure 50 shows the microstructures of 400 W and 550 mm/min with different printing direction between layers. The parallelepiped is made up of four layers built with four beads. The microstructure images of the other parameters are shown in appendix VII. After the change of direction in the deposition, no preferential direction in the solidification of the molten metal was observed.
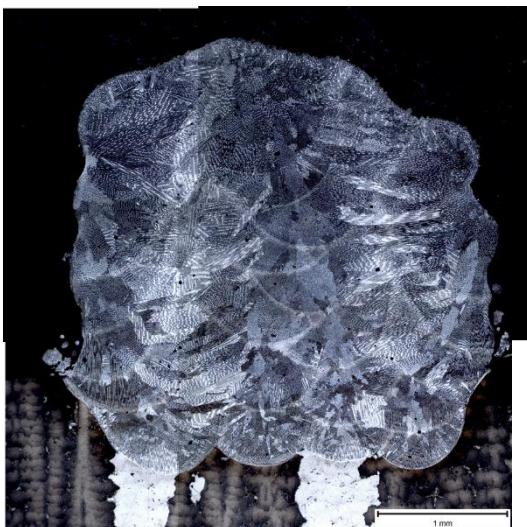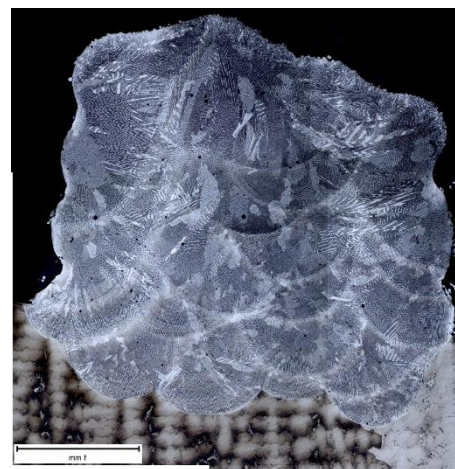


A)  400-550-0-A                    B)  400-550-180-A

Figure 50. Microstructure 0° and 180° rotation interlayer

Figure 51 shows the microstructure of 300 W and 450 mm/min at different magnifications. Therefore, no significant changes in the microstructure are evident; most of the solidification mode found was columnar at the interface and equiaxed dendritic growth at the subsequent layers. Figure 51A shows the equiaxial growth in the first layer. In Figure 51B it is clear to see the equiaxed dendrites structure.
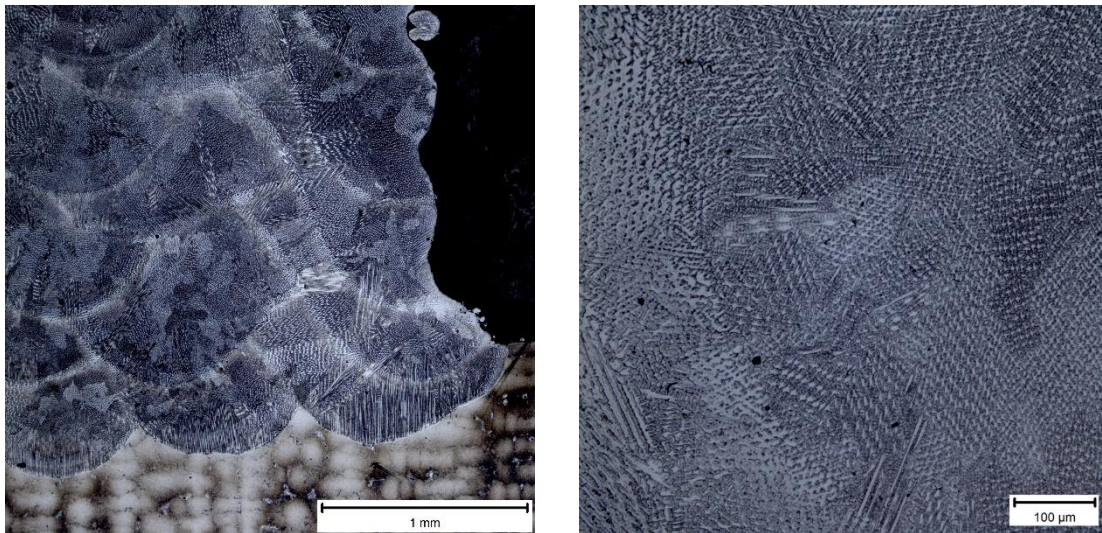


A) 300-450-0-A at 50X     B) 300-450-0-A at 200X

Figure 51. Microstructure of 300-450-0-A sample

## 5.3.2.4 Microhardness evaluation

Microhardness measurements were made to a single replicate of each parameter combination. The results are plotted and shown in the following figure. All the specimens have the same behavior, an increase in hardness at the HAZ and a stabilization zone in the molten metal. Hardness variations in all experiments do not exceed 10 %. GTD 111 and René 65 printed by LP-DED have similar hardness approximately 400 HV, as seen in Figure 52A. A hardness map was made on the specimen with 300W-450 mm/min and rotated 180° between layers. The results show a constant hardness between the substrate and the molten metal, with a decrease in the upper part of the deposit. Some blue colors represent porosities in the specimens (Figure 52B).

**Hardness Profile (HV)**
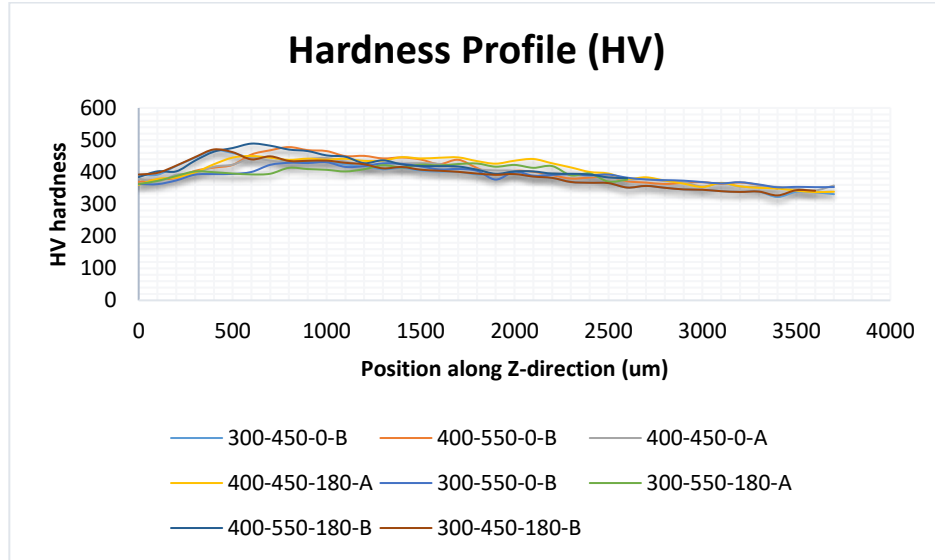
A) Hardness profile of LP-DED samples
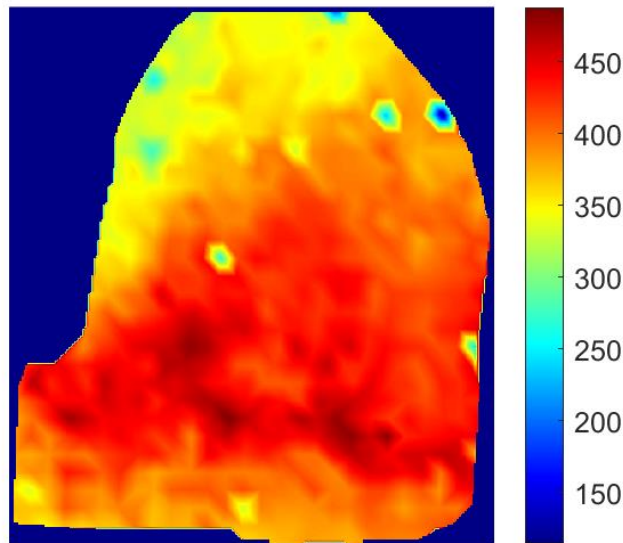


B) Microhardness map in sample 300-450-180-B

Figure 52. Hardness profile and mapping of LP-DED samples

### 5.3.2.5 EBDS analysis

Figure 53 shows the EBSD inverse pole figure (IPF) map from the cross-section of the parallelepiped sample parallel to the build direction of the as-built condition. Printed with 400 W, 450 mm/min and varied the direction of printing between 0° and 180°. The grains grow without any crystallographic preference unaligned with build direction. The grain morphology and orientation in weld metal are similar for both cases, presenting an equiaxed dendritic growth without a defined orientation.
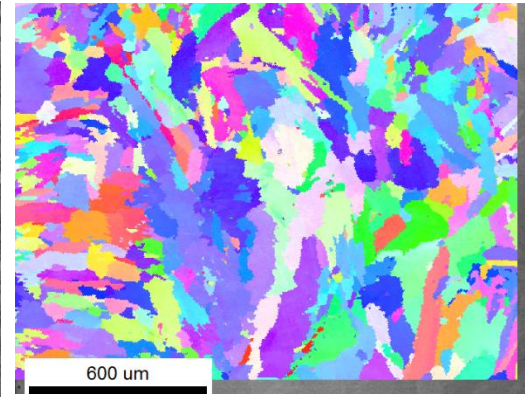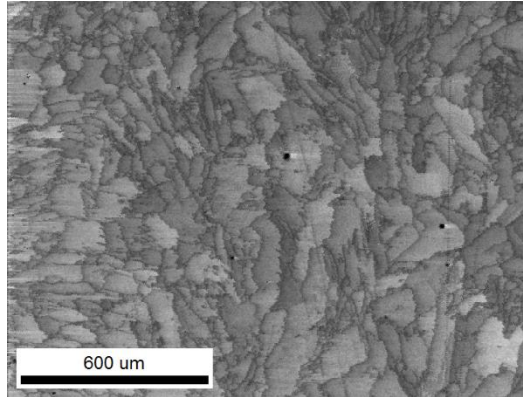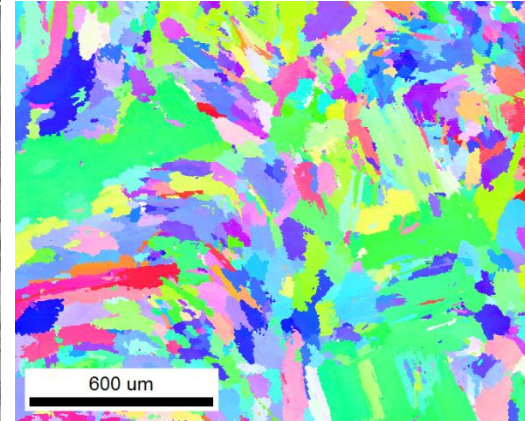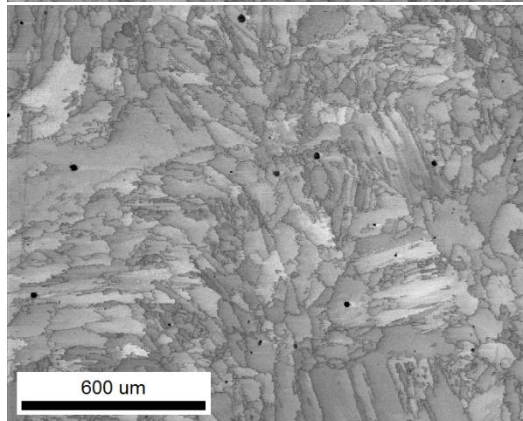
Figure 53. EBSD images of 300W-450mm/min and different sequence of application A) unidirectional and B) Bidirectional

Other EBSD images are shown in Figure 54. The parameters used are 400 W- 450 mm/min with 0° and 180°. An area of approximately 2 mm x 2 mm is examined. Generally speaking, no difference can be found between the two printing. The grains are solidified in an equiaxed manner showing similar angles of rotation.

A) 400 W-450 mm/min-0°



B) 400 W-450 mm/min-180°
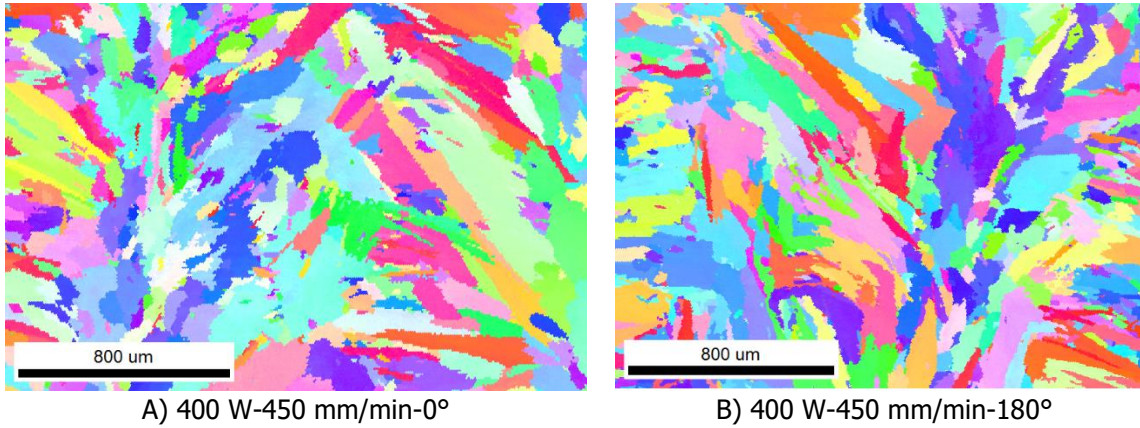
Figure 54. EBSD images of 400 x- 450 mm/min varying rotation sequence A) unidirectional and B) Bidirectional

The interface between GTD 111 and René 65 is represented in Figure 55. It can be seen the directional solidified microstructure of GTD 111 blades in red (001) and the non-uniform solidification direction in printed deposits.
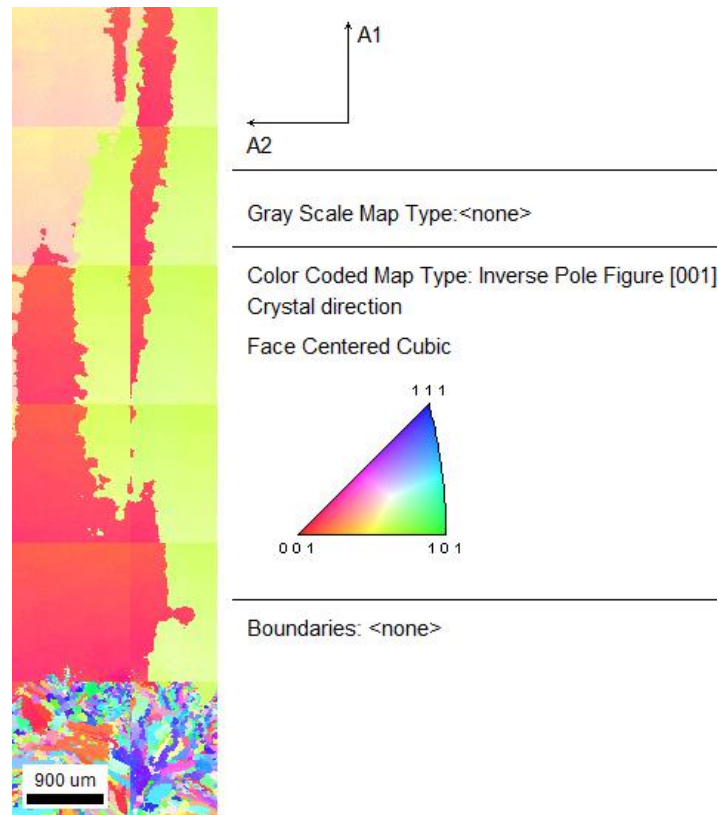


Figure 55. Interface between GTD 111 and René 65

## 5.3.3 Statistical Analysis

A full factorial design (DOE) $2^3$ with replica was implemented for experimental data analysis. Thus, 16 test conditions were performed in total in a random way. The independent variables and their respective levels are shown in Table 14.

Table 14. Factors Information of LP-DED DOE

| Factor | Levels | Values |
|---|---|---|
| Power | 2 | 300, 400 |
| Travel Speed | 2 | 450, 550 |
| Rotation | 2 | 0, 180 |

The first output parameter investigated was the hardness, an analysis of variance (ANOVA) method was used to identify the main effect and interaction between factors. A 95% confidence level and significance level of 5% (p-value) were set for all tests, thus values below the significance level are considered statistically significant. In Table 15, it is possible to see the results of ANOVA. Each factor has a significant effect individually and the 2-way interactions have a p-value less of 0.05. The same result is shown in Figure 56 in Pareto chart, a red line represents the significance level. The model adequacies were checked by adjusted-$R^2$ of 97.6%.

Power, travel speed and rotation layers have significant effect in hardness separately, in addition, the combination of power-travel speed, power-rotation and travel speed-rotation do not have significant effect in hardness due to P-value < 0.05.

Table 15. Analysis of Variance-Hardness- LP-DED

| Source | DF | Adj SS | Adj MS | F-Value | P-Value |
|---|---|---|---|---|---|
| Model | 7 | 1640.00 | 234.286 | 66.94 | <0.001 |
| Linear | 3 | 1545.00 | 515.000 | 147.14 | <0.001 |
| Power | 1 | 784.00 | 784.000 | 224.00 | <0.001 |
| Travel Speed | 1 | 361.00 | 361.000 | 103.14 | <0.001 |
| Rotation | 1 | 400.00 | 400.000 | 114.29 | <0.001 |
| 2-Way Interactions | 3 | 86.00 | 28.667 | 8.19 | 0.008 |
| Power*Travel Speed | 1 | 25.00 | 25.000 | 7.14 | 0.028 |
| Power*Rotation | 1 | 25.00 | 25.000 | 7.14 | 0.028 |
| Travel Speed*Rotation | 1 | 36.00 | 36.000 | 10.29 | 0.012 |
| 3-Way Interactions | 1 | 9.00 | 9.000 | 2.57 | 0.147 |
| Power*Travel Speed*Rotation | 1 | 9.00 | 9.000 | 2.57 | 0.147 |
| Error | 8 | 28.00 | 3.500 | | |
| | | | | | |
| Total | 15 | 1668.00 | | | |
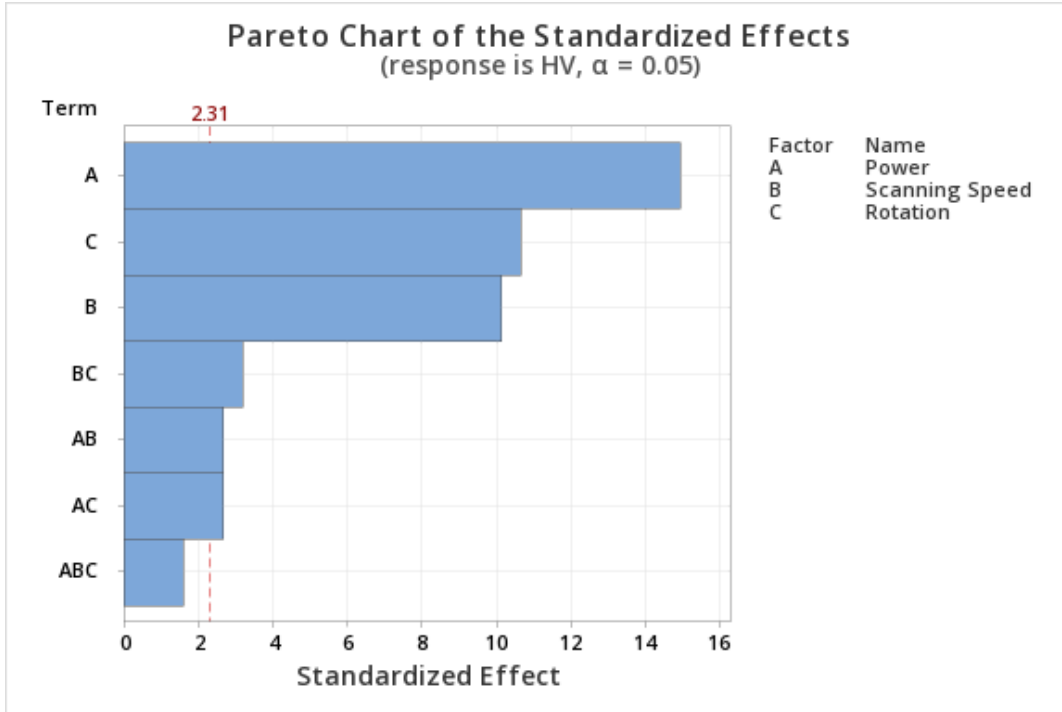
Figure 56. Pareto Chart of Hardness. LP-DED

Main effects for hardness are plotted in Figure 57. It is observed a slightly increase tendency in high values of power, scanning speed and 180° rotation layers in hardness.
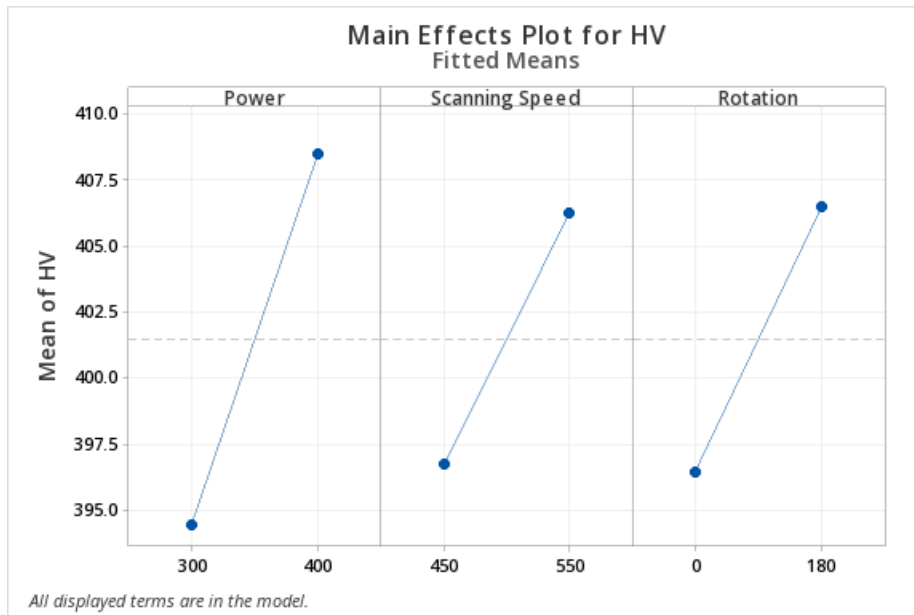


Figure 57. Main effects for HV. LP-DED

Interaction plot for hardness is shown in Figure 58. It is clear a proportional tendency to increase hardness due to high power and scanning speed. Rotate the direction between layers in 180° showed high values of hardness.
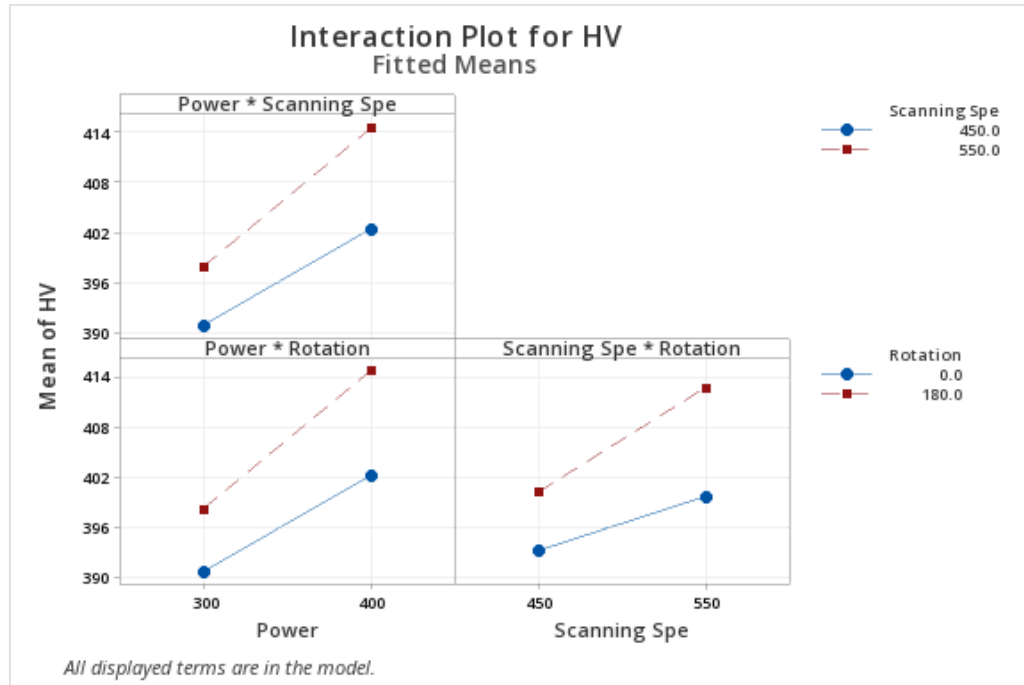


Figure 58. Interaction of factors for HV. LP-DED

In Figure 59 are shown the residual plots, that indicate independence and a normal distribution. It has a symmetry and high density of points close to the origin. These facts confirm all assumptions.
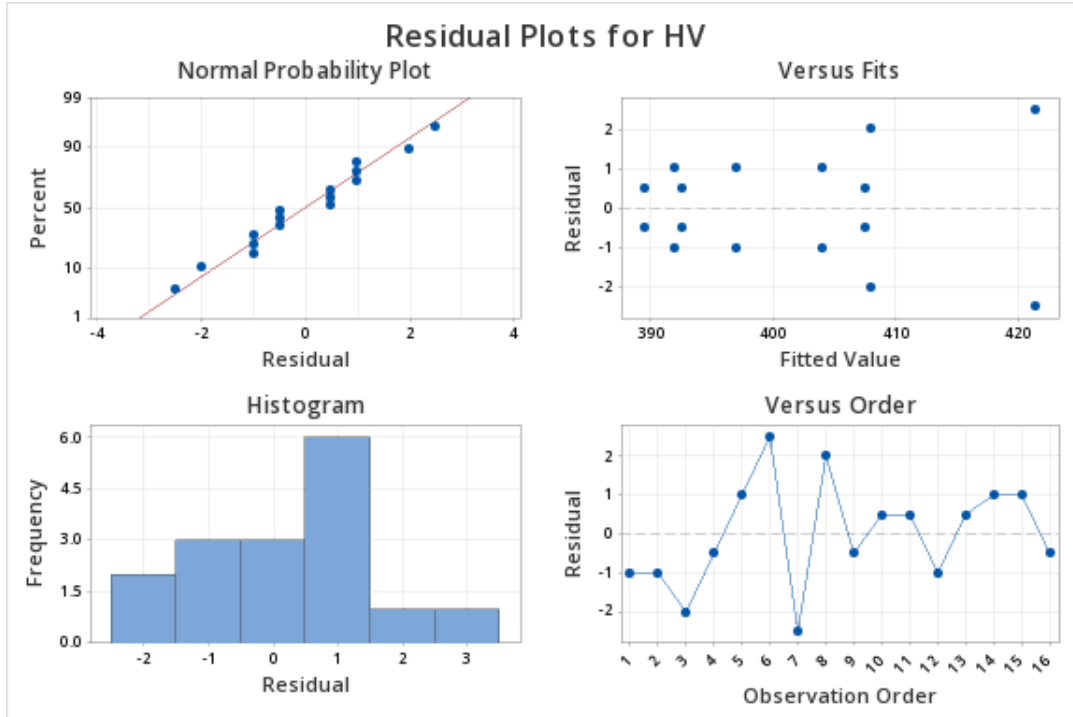
Figure 59. Residual Plots for HV. LP-DED

The other output parameter investigated is the percentage of porosity. According to Table 16 and Figure 61, analysis of variance and Pareto´s chart confirmed that power, scanning speed have main effects of porosity. On the hand, the interaction of power-scanning speed, power-rotation and scanning speed-rotation have significant effects of porosity.

Table 16. Analysis of Variance % Porosity

| Source | DF | Adj SS | Adj MS | F-Value | P-Value |
|---|---|---|---|---|---|
| Model | 7 | 0.078100 | 0.011157 | 81.14 | <0.001 |
| Linear | 3 | 0.021825 | 0.007275 | 52.91 | <0.001 |
| Power | 1 | 0.003600 | 0.003600 | 26.18 | 0.001 |
| Scanning Speed | 1 | 0.018225 | 0.018225 | 132.55 | <0.001 |
| Rotation | 1 | 0.000000 | 0.000000 | 0.00 | 1.000 |
| 2-Way Interactions | 3 | 0.047250 | 0.015750 | 114.55 | 0.001 |
| Power*Scanning Speed | 1 | 0.038025 | 0.038025 | 276.55 | <0.001 |
| Power*Rotation | 1 | 0.003600 | 0.003600 | 26.18 | 0.001 |
| Scanning Speed*Rotation | 1 | 0.005625 | 0.005625 | 40.91 | <0.001 |
| 3-Way Interactions | 1 | 0.009025 | 0.009025 | 65.64 | 0.001 |
| Power*Scanning Speed*Rotation | 1 | 0.009025 | 0.009025 | 65.64 | <0.001 |
| Error | 8 | 0.001100 | 0.000138 | | |
| | | | | | |
| Total | 15 | 0.079200 | | | |
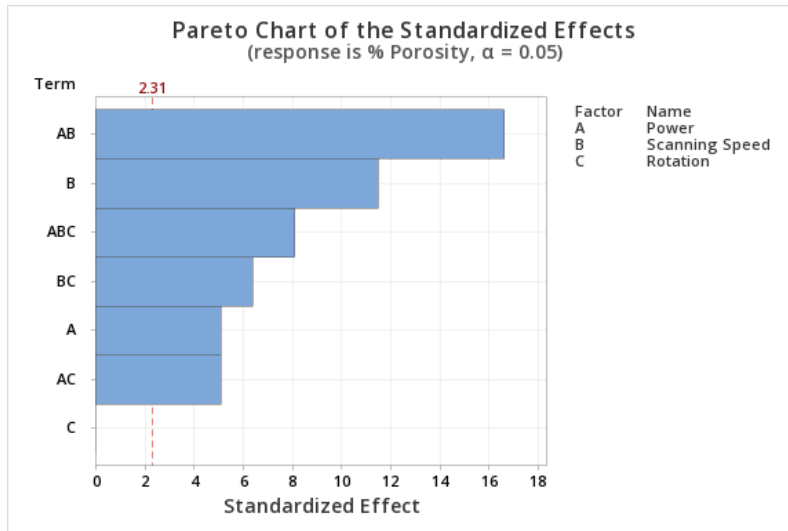
Figure 60. Pareto Chart of % porosity. LP-DED

Figure 61 shows residual plot for porosity confirmed that all results are distributed as normal probability and the symmetry in residual meaning good assumptions.
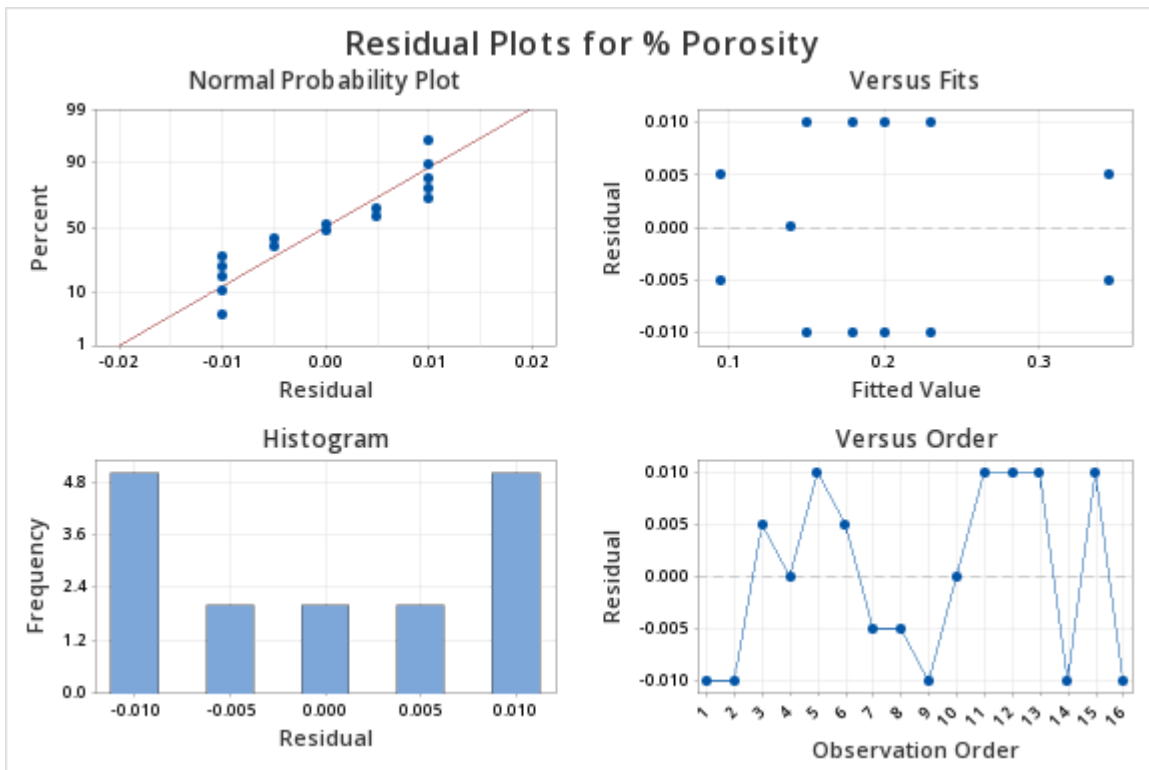


Figure 61. Residual Plots % Porosity in LP-DED process

Main effects plot for porosity shows in Figure 62 that it is possible to obtain better porosity results for 300 W, a high scanning speed of 550 mm/min and any differences with different rotations.
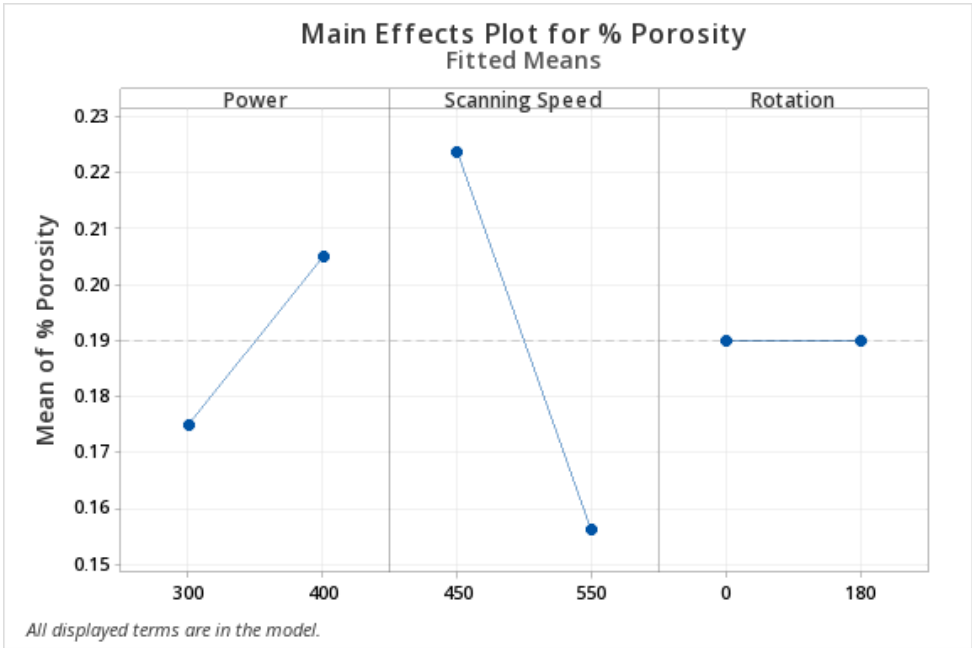


Figure 62. . Main effects Plot for % Porosity LP-DED

Interaction plot shows the response in porosity when a combination of parameters is carried out as described in Figure 63.  0.12 percentage of porosity was acquired using 400 W and 550 mm/min and 0.28 percentage of porosity setting 400 W and 450 mm/ min. Furthermore, the interaction between travel speed and rotation of layers shows an inversely proportional behavior.
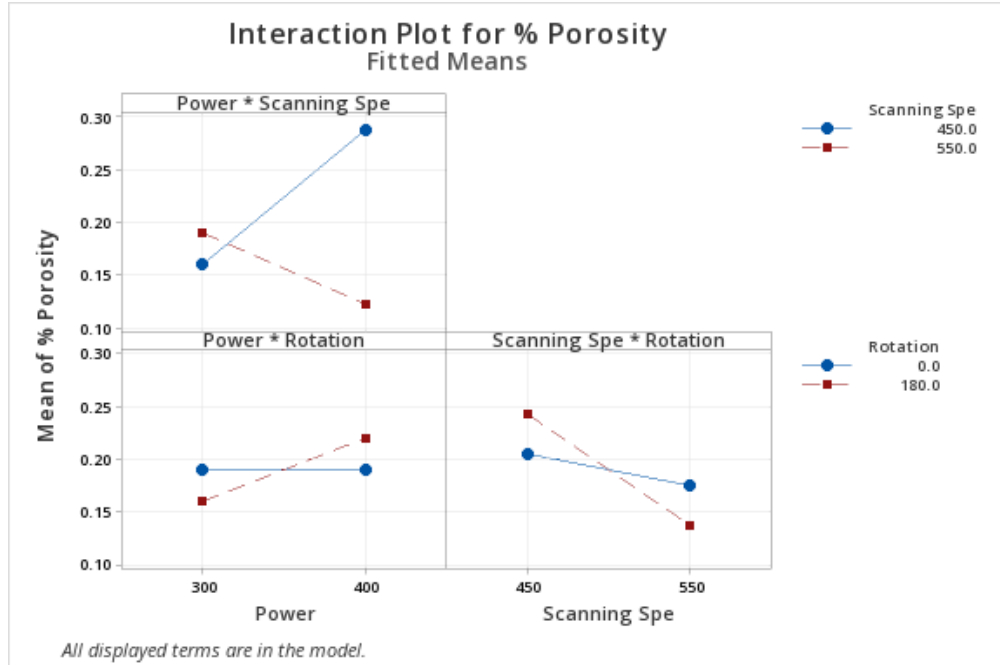
Figure 63. Interaction Plot for % Porosity. LP-DED

## 5.3.4 Wall printed sample

Once the DOE was performed, the combination of parameters of 300 W and 450 mm/min was selected to perform the restoration of a 3 mm wall in a GTD 111 sample. The dimensions simulate the restoration of the squealer tip (Figure 64). This testing confirmed the feasibility of using the LP-DED process in the repair of GTD 111 blades by NC programming.
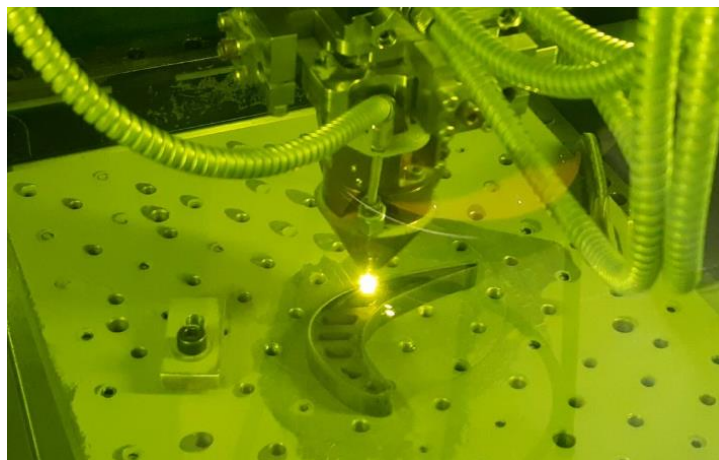


Figure 64. Wall printed sample using LP-DED

### 5.3.5 Main conclusions about the LP-DED process

The most relevant conclusions regarding the use of the LP-DED process in the recovery of GTD 111 blades are summarized below.

1. It is possible to melt powders with a PSD of 15/45 um, specially manufactured for L-PBF, efficiently with the LP-DED process.

2. The speed of completion of the pieces printed with LP-DED is very short, around 3 minutes to print the wall of the squealer tip.

3. Deposits free of defects and with a density greater than 99% were obtained without the use of preheat temperature.

4. LP-DED is an ideal additive manufacturing process for the repair or restoration of medium and large parts. Producing minimal heat affectation to the substrate with much better resolution than any welding process.

## 5.4 L-PBF manufacturing

### 5.4.1 Exploratory Stage

The objective of the exploratory stage is to provide information to understand the effect of processing parameters and to find stable deposits printed on SS 316 substrate using René 65 powder. Appendix IX and X show a top view of single beads and a layer of three beads with different conditions. The parameters tested are provided in Table 17.

Table 17. Preliminary test Single Beads L-PBF

| $P_{(W)}$ / $V_{(mm/s)}$ | 50 | 60 | 70 | 80 | 90 |
|---|---|---|---|---|---|
| 200 | 1 | 6 | 11 | 16 | 21 |
| 400 | 2 | 7 | 12 | 17 | 22 |
| 600 | 3 | 8 | 13 | 18 | 23 |
| 800 | 4 | 9 | 14 | 19 | 24 |
| 1000 | 5 | 10 | 15 | 20 | - |

All deposits were analyzed by dimensional stability in top and cross view, other analysis was focused on the measure of porosity in cubic sample of 20 mm. Figure 65 shows some results of the best combination of parameters, 80 W and 400 mm/s. A good dimensional stability was found in top view of a layer of three beads, as seen in Figure 65A. Figure 65B shows the cross section that get an adequate wet angle to ensure a proper multilayer deposition. After these two tests, a cube was printed to measure the percentage of porosity. Figure 65C

shows a cube printed on SS 316 substrate, whose results are presented in Figure 65 D having >99% of porosity.
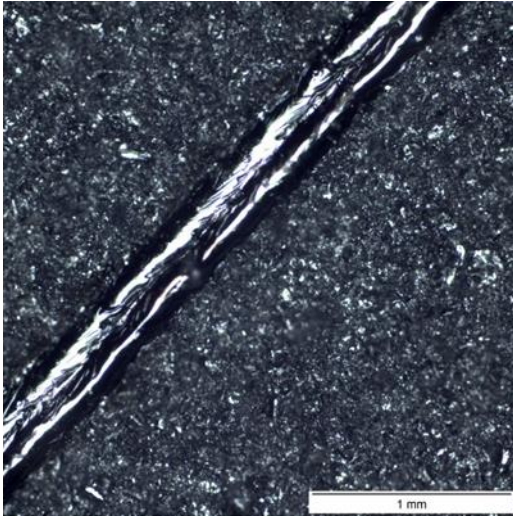


A) Top view of a layer of three beads
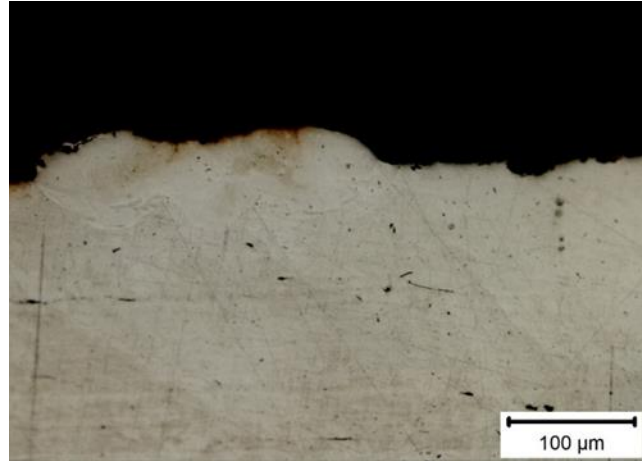


B) Cross-section of a layer of three beads
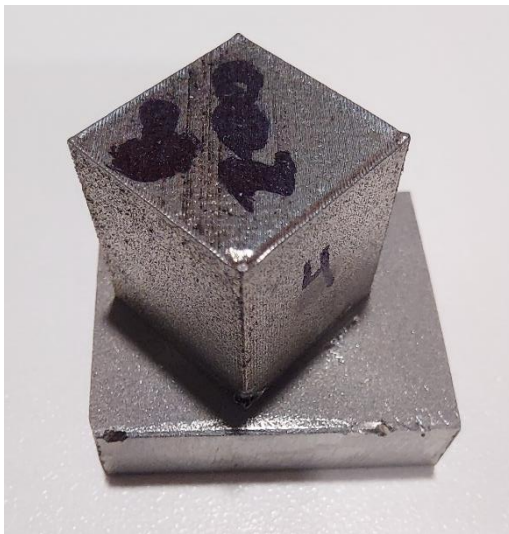


C) Printed cubic sample 80-200
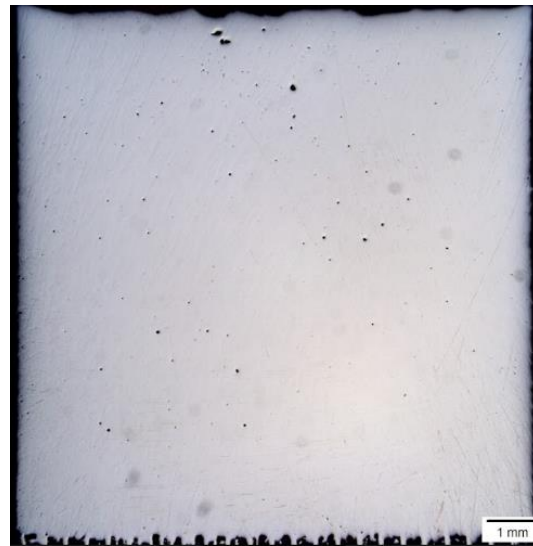


D) Cross section of a cube of 20 mm

Figure 65. Preliminary testing of L-PBF

## 5.4.2 Experimental stage

Two values of power, scanning speed and rotation between layers were defined. Additionally, the layer thickness and the hatch spacing was set to 80 μm. Table 18 describes

the different parameters used in the experiments. Two replicates were made for each combination.

Table 18. Parameters for DOE using L-PBF

| Power (W) | Scanning speed (mm/s) | Hatch spacing (um) | layer thickness (um) | Rotation (°) |
|---|---|---|---|---|
| 50 | 200 | 80 | 25 | 0 |
| 50 | 200 | 80 | 25 | 90 |
| 80 | 400 | 80 | 25 | 0 |
| 80 | 400 | 80 | 25 | 90 |
| 50 | 400 | 80 | 25 | 0 |
| 50 | 400 | 80 | 25 | 90 |
| 80 | 200 | 80 | 25 | 0 |
| 80 | 200 | 80 | 25 | 90 |

## 5.4.2.1 Visual Examination

Figure 66 shows sixteen parallelepipeds deposited with the parameters previously described with 5 x 5 x 2 mm. After visual inspection, all samples showed a good adhesion except one (50-400-0-B) that detached almost completely and is pointed by the white arrow. In addition, a good dimensional stability in all cubes were obtained.
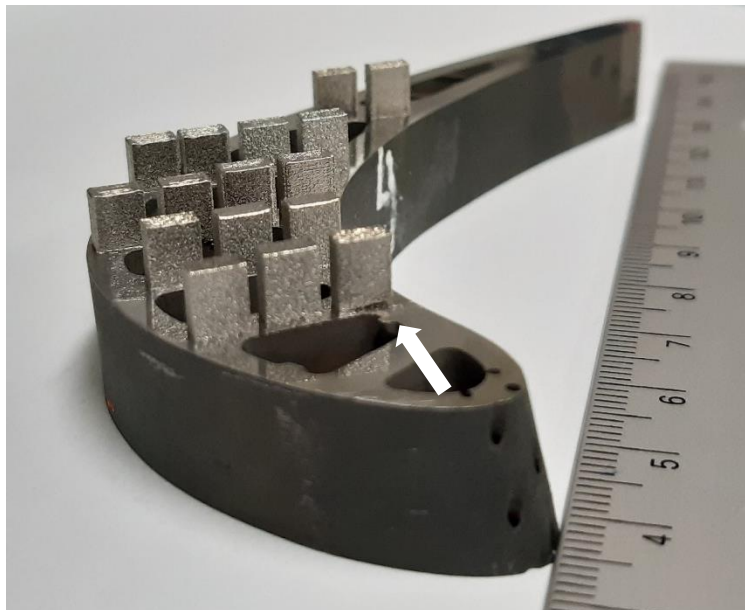


Figure 66. Printed samples according to Table 16

## 5.4.2.2 Cross sectional analysis for porosity

Porosity measurements were performed by image analysis using ImageJ software. Figure 67 shows the aspect of the samples with the lowest porosities found in the design of experiment, which have less porosity than the blade's substrate. All the studied cross sections can be observed in appendix XIII.



A)  50 W, 400 mm/s, 90°          B)  80 W, 400 mm/s, 0°
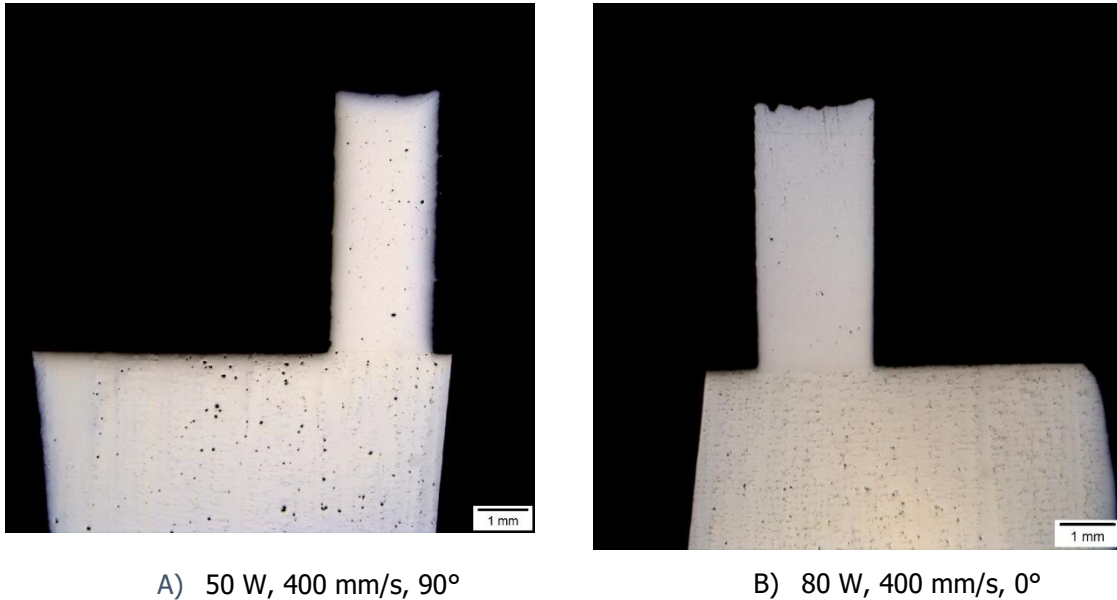
Figure 67. Printed samples of L-PBF DOE

The results of porosity in L-PBF samples are described in Figure 68. The highest values of porosity were found in samples with higher density energy. Generally speaking, every replication has approximately the same porosity, and a slight decrease in porosity was found in deposits printed with 90° of rotation between layers, with the sole exception of 80-400-90 samples. In these tests, only six samples out of sixteen have a value of porosity lower than 1%. There are two combinations of parameters that reach around 0.1% of porosity, namely 50-400-90 and 80-400-0 (Figure 67).
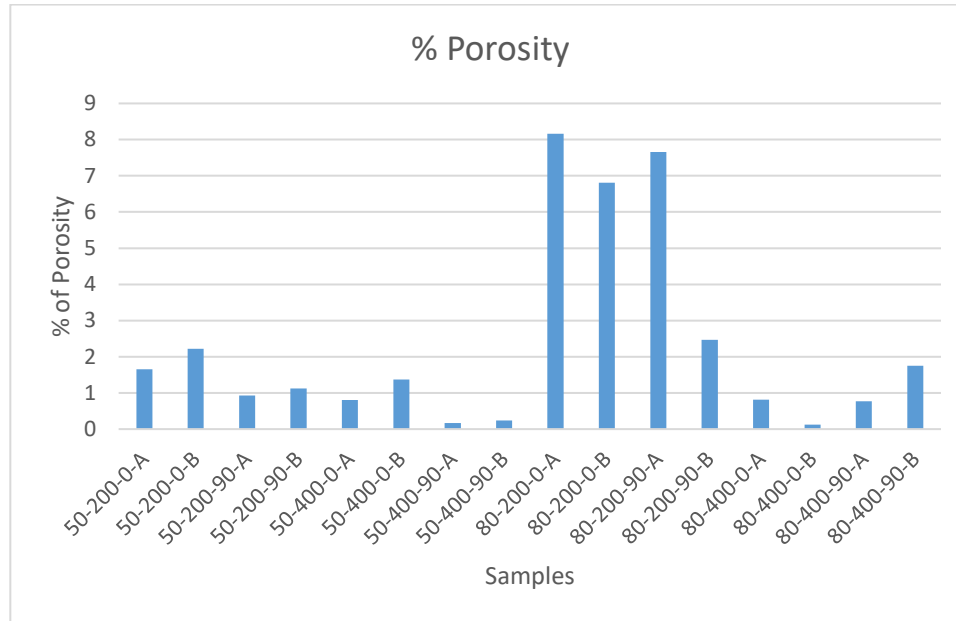
Figure 68. Results of % porosity in L-PBF experimental stage

## 5.4.2.3 LOM Characterization

The analysis focused on the samples with low porosity since the porosity of the as-built (AB) parts affect the ultimate strength and fatigue (Beretta, 2017). Figure 69 shows the AB microstructure of 50-400-90 at different magnifications. The built direction is marked by a blue arrow. All specimens were analyzed at 12.5x, 50x and in some cases at higher magnifications such as 200x and 1000x. In appendices XIV and XV you can see the rest of the images.

The microstructure of AM parts is highly dependent on the processing parameters. Columnar dendrite structure is formed in the Z direction, the microstructure exhibits anisotropy due to the dendrite structure (Den, 2018). The temperature gradient flowing from top to the bottom, thus the angle between the direction of the flux and the crystallographic direction <001> is the lowest, therefore the chosen direction. Different combination between temperature gradient and growth rate affects the final solidification structure. In general, there are columnar grains, equiaxed grains and a mix of them.

A) 50-400-90-A at 50x

B) 50-400-90-A at 200x
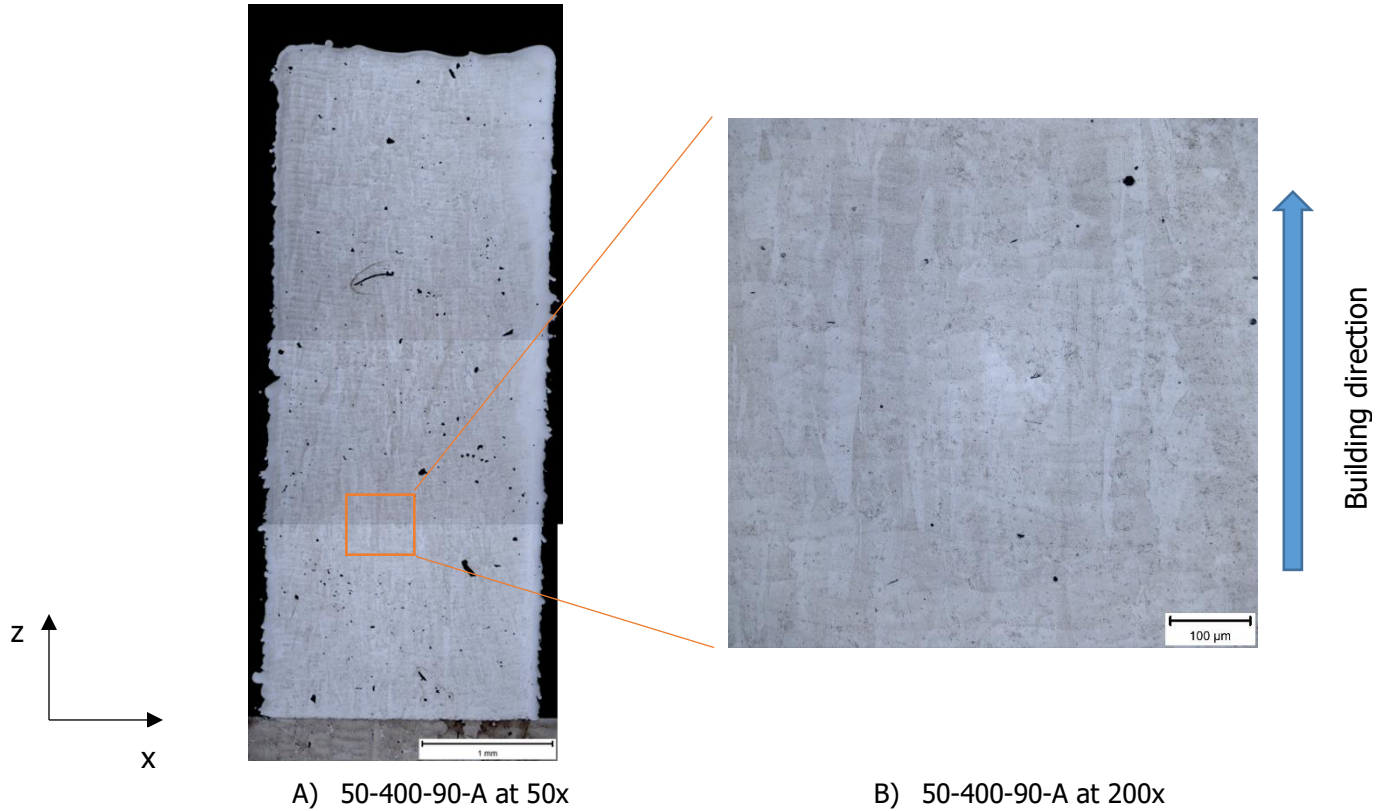
Figure 69. OM examination in L-PBF samples

Figures 70A and 70B describe the microstructure of 50-400-0 sample at different magnifications without defects. In Figure 70B it is possible to distinguish columnar dendrites (C.D) and equiaxed dendrites (E.D). On the other hand, Figures 70C and D show the microstructure of the 50-200-90-B sample. The use of these process parameters led to the formation of some pores and vertical cracks as shown in Figure 70D.



A) 50-400-0-B-200X

B) 50-400-0-B-1000X
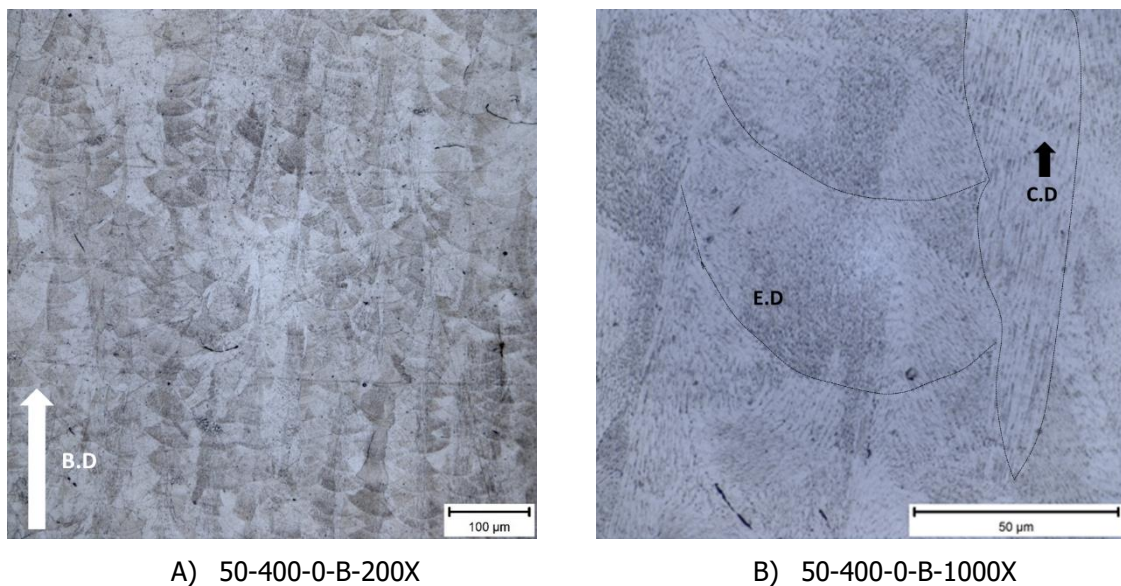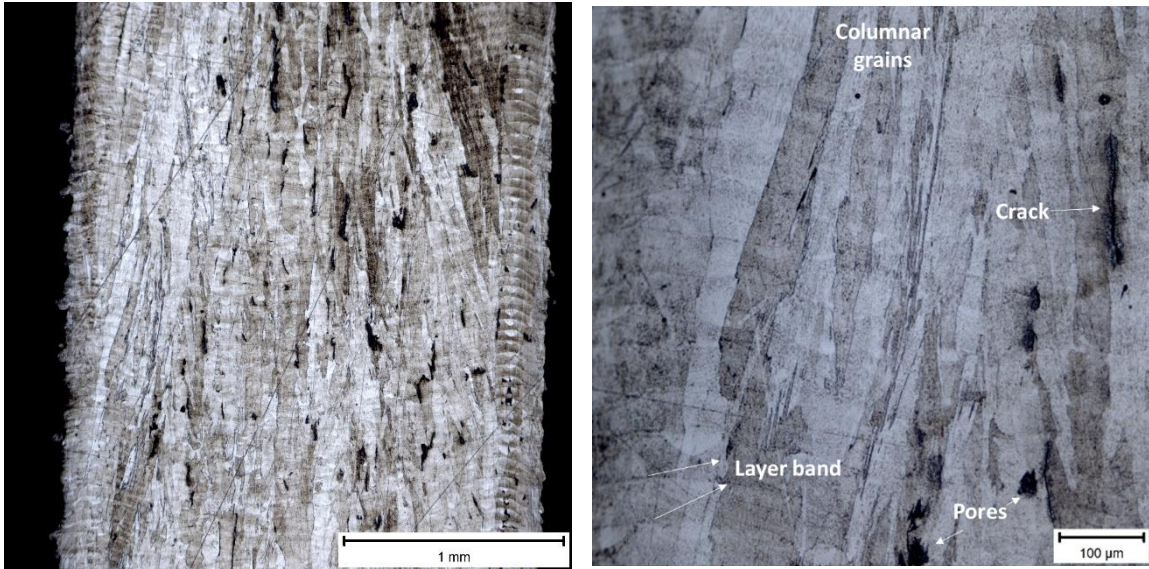
C)  50-200-90-B-50X          D)  50-200-90-B-200X

Figure 70. Microstructure of L-PBF samples

## 5.4.2.4 Microhardness evaluation

Microhardness profiles of the cross section of the samples along the build direction are given in Figure 71. The profiles were done only in sound samples, samples with a huge quantity of porosity were discarded for this evaluation. The remarkable fact in this testing is that using low energy density reduces the hardness of deposits with René 65 powder. Higher hardness values were found in samples using 80 W. A steep drop in hardness happens at the spot of defects.
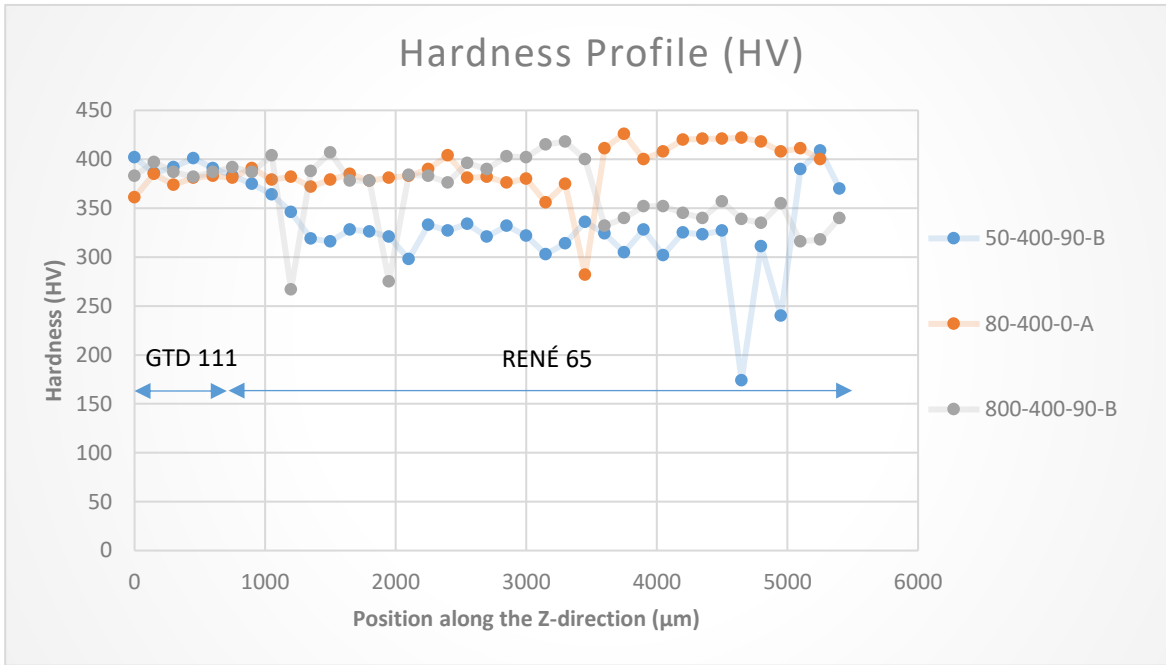
Figure 71. Hardness Profile (HV) of L-PBF samples

Figure 72 shows several indentation marks that can be regarded as an indication of the good adherence between the substrate and the deposits. A microhardness mapping of 80-400-0 sample is shown in Figure 72A. The deposit has a slightly softer microstructure compared to the substrate (~400 HV).
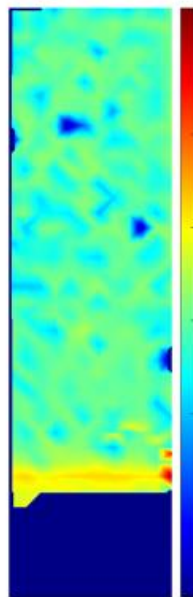


A)  800-400-0
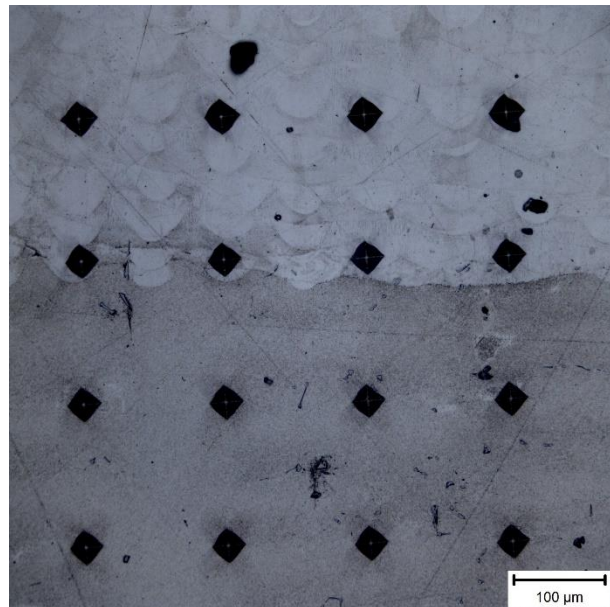


B)  80-400-90-B-200X

Figure 72. Microhardness mapping L-PBF samples

## 5.4.2.5 EBSD Analysis

The crystallographic texture data was revealed by EBSD grain structural maps using inverse pole figure (IPF) in the as-built condition and it is presented in Figure 73. Figure 73A shows an indexation quality map from the EBSD scan and Figure 73B describes the IPF images of the same transverse section. A random texture of grains is observed with a tendency to align with <001>. Such preferential orientation of grains is a consequence of the vertical heat flux direction.

Figure 73B presents the interface between the GTD 111 substrate and René 65. It is possible to see the directionally solidified microstructure of GTD 111 at the top of the image and the epitaxial growth of René 65 microstructure. Figure 73C shows a kernel average misorientation (KAM) map of the 80-400-0 sample, the as-built microstructure shows some residual local misorientation due to several remelting microstructures. On the other hand, Figure 73D shows the misorientation distribution graph, confirms that the misorientation angle of the grains is mostly distributed between 0 and 5 degrees, corresponding to a uniform orientation of the cubic structure.



Color Coded Map Type: Inverse Pole Figure [001]
Crystal direction

Face Centered Cubic

A)  Micrograph                    B)  IPF-EBSD
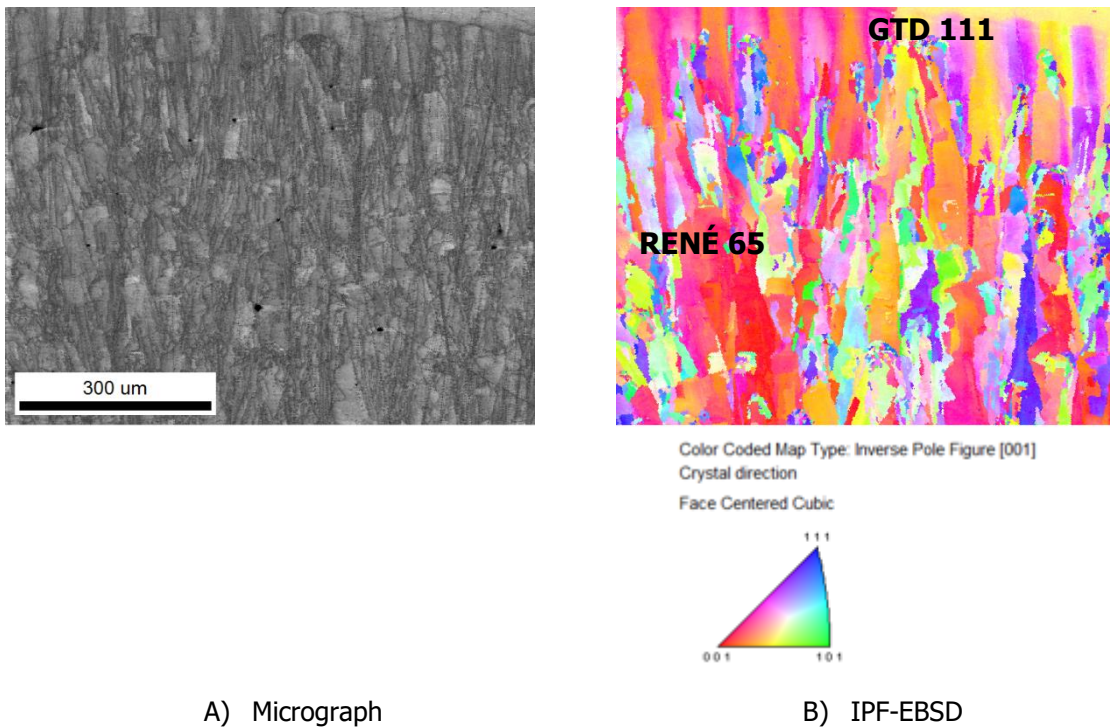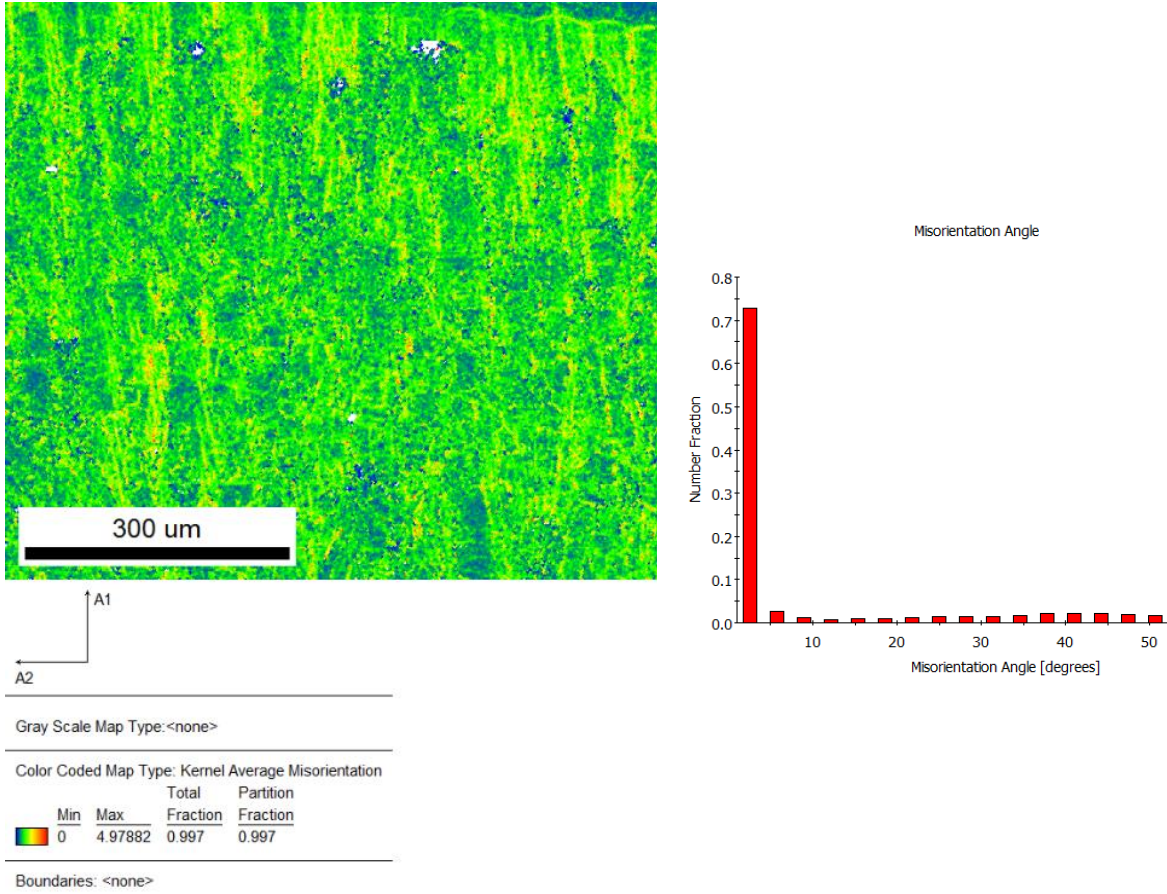
| C) KAM map | D) Misorientation angle from EBSD |

Figure 73. EBSD results of L-PBF 80-400-0 sample

## 5.4.3 Statistical Analysis

As the same manner as 5.3, a full factorial design (DOE) $2^3$ with replica was implemented for experimental data analysis. A total of 16 test conditions were performed in a random way. A 95% confidence level and significance level of 5% (p-value) were set for all tests, thus values below the significance level are considered statistically significant. The full factorial design is shown in Table 19.

Table 19. Full Factorial Design of L-PBF testing

| Power | Scanning Speed | Rotation |
|-------|----------------|----------|
| 50 | 400 | 90 |
| 80 | 200 | 90 |
| 80 | 400 | 90 |

| | | |
|---|---|---|
| 50 | 200 | 0 |
| 50 | 200 | 90 |
| 80 | 200 | 0 |
| 50 | 200 | 90 |
| 80 | 200 | 90 |
| 50 | 400 | 0 |
| 80 | 400 | 90 |
| 50 | 400 | 90 |
| 50 | 400 | 0 |
| 80 | 400 | 0 |
| 50 | 400 | 0 |
| 50 | 200 | 0 |
| 80 | 200 | 0 |

The response of hardness variable in the full design factorial is unstable due to high percentage of porosity. Three hardness samples were reported with a stable behavior and presented in Figure 71. Due to the quantity of defects and the extremely drop in hardness any statistical analysis was done in this testing.

In Table 20, the result of ANOVA was presented for porosity analysis. Any variable with a P-value less of 0.05 is considered with a significant effect. Scanning speed has a strong consequence result into porosity, and p-value of power is close to the permitted limit of 0.005. In this case, the influence of power is taking into account as significant. 2-ways and 3-ways interactions do not have effect in the porosity response

Table 20. ANOVA analysis of porosity variable

| Fuente | GL | Aj. SS | Aj. MS | Value F | Value p |
|---|---|---|---|---|---|
| Model | 7 | 93,201 | 13,3144 | 6,90 | 0,007 |
| Lineal | 3 | 67,072 | 22,3573 | 11,58 | 0,003 |
| Power | 1 | 25,125 | 25,1252 | 13,02 | 0,007 |
| Scanning Speed | 1 | 39,031 | 39,0313 | 20,22 | 0,002 |
| Rotation | 1 | 2,916 | 2,9156 | 1,51 | 0,254 |
| 2-ways Interactions | 3 | 23,593 | 7,8643 | 4,07 | 0,050 |
| Power*Scanning Speed | 1 | 20,954 | 20,9535 | 10,85 | 0,011 |
| Power*Rotation | 1 | 0,007 | 0,0068 | 0,00 | 0,954 |
| Scanning Speed*Rotation | 1 | 2,633 | 2,6325 | 1,36 | 0,277 |
| 3 ways interaction | 1 | 2,536 | 2,5361 | 1,31 | 0,285 |
| Power*Scanning Speed*Rotation | 1 | 2,536 | 2,5361 | 1,31 | 0,285 |
| Error | 8 | 15,443 | 1,9304 | | |
| Total | 15 | 108,644 | | | |

The same result is shown in Figure 74 in Pareto chart, a red line represents the significance level. The model adequacies were checked by adjusted-$R^2$ of 73.35% and $R^2$ of 86%. Power, scanning speed and interaction of them has a significant effect in porosity.
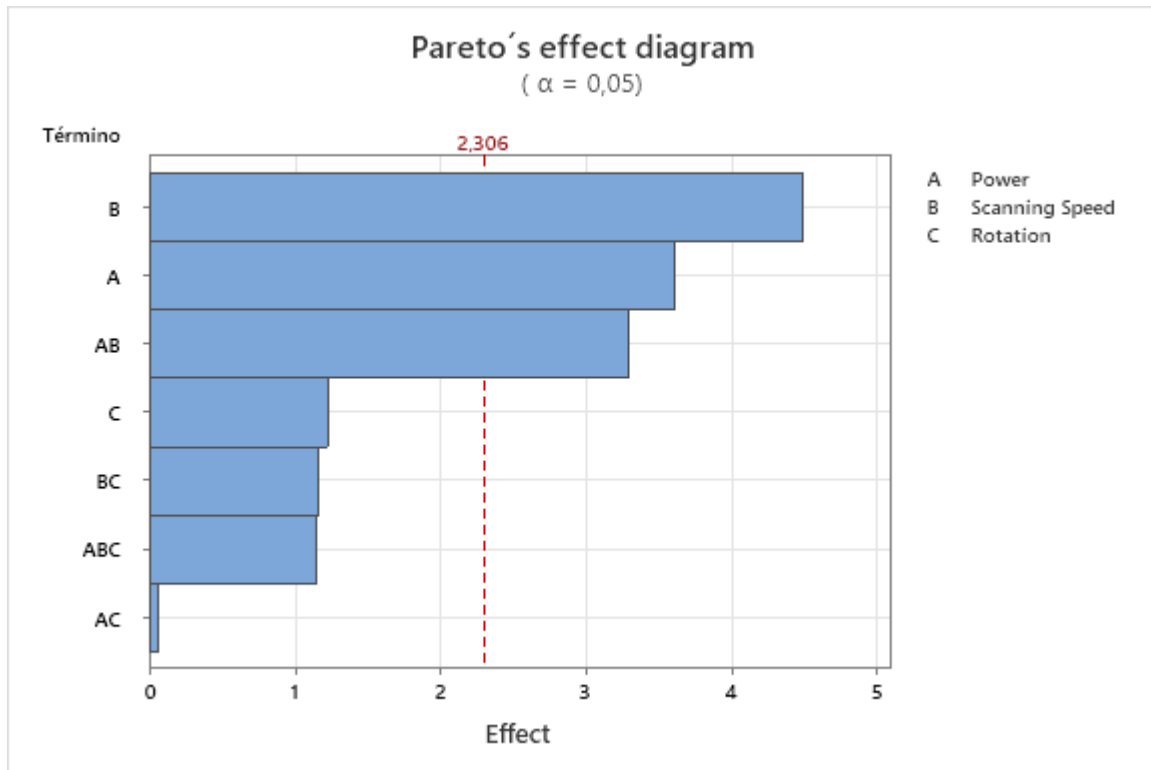


Figure 74. Pareto´s chart of porosity analysis

Main effects for porosity are plotted in Figure 75. It is observed that low value is obtained with low power and high scanning speed. Rotation does not have relevance in porosity results.
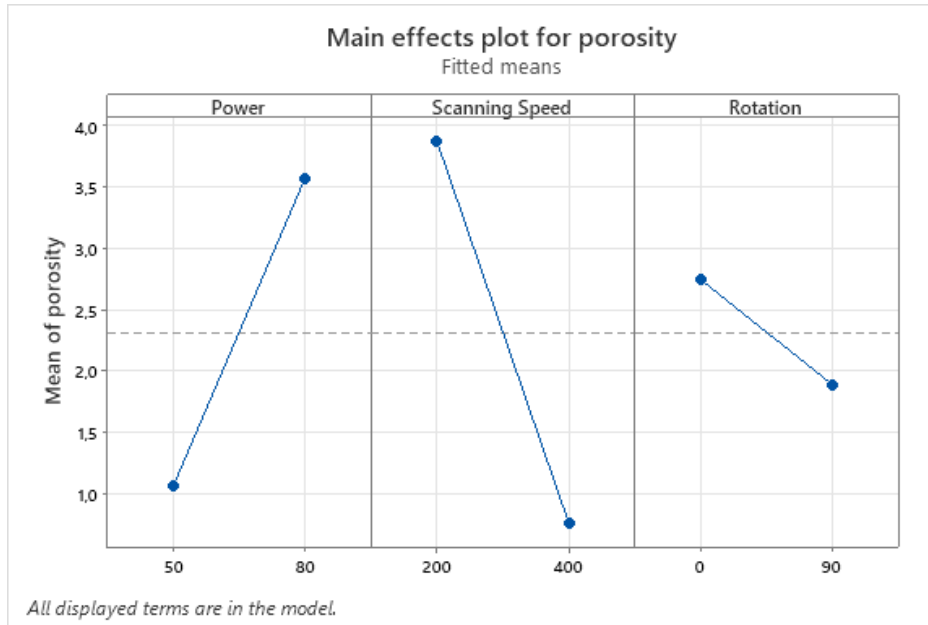
Figure 75. Main effects of porosity. L-PBF

Interaction plot for porosity is shown in Figure 76. High value of scanning speed keeps low porosity independently of the power magnitude. There is a proportional tendency to increase porosity when power arise to 80 W regardless the rotation of layers. Furthermore, at 400 mm/s low porosity values are reached at any rotation.
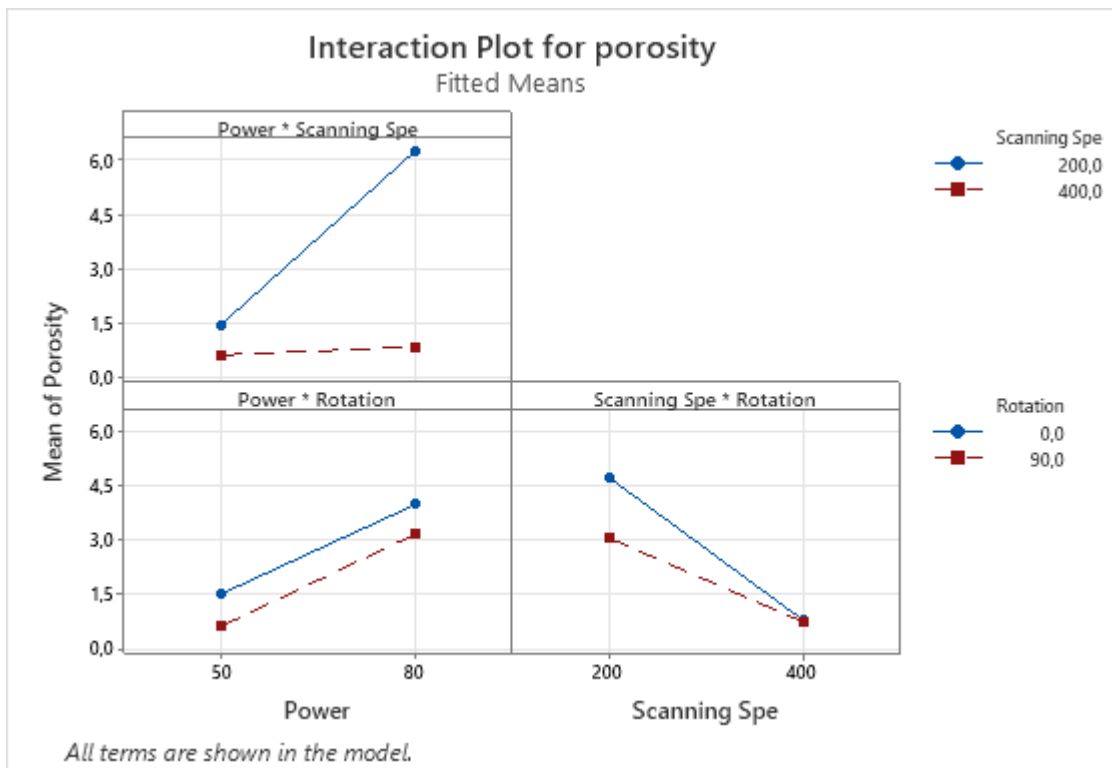
Figure 76. Interaction of factors for porosity. L-PBF.

In Figure 77 are shown the residual plots, that indicate independence and a normal distribution. It has a symmetry and high density of points close to the origin. These facts confirm all assumptions.
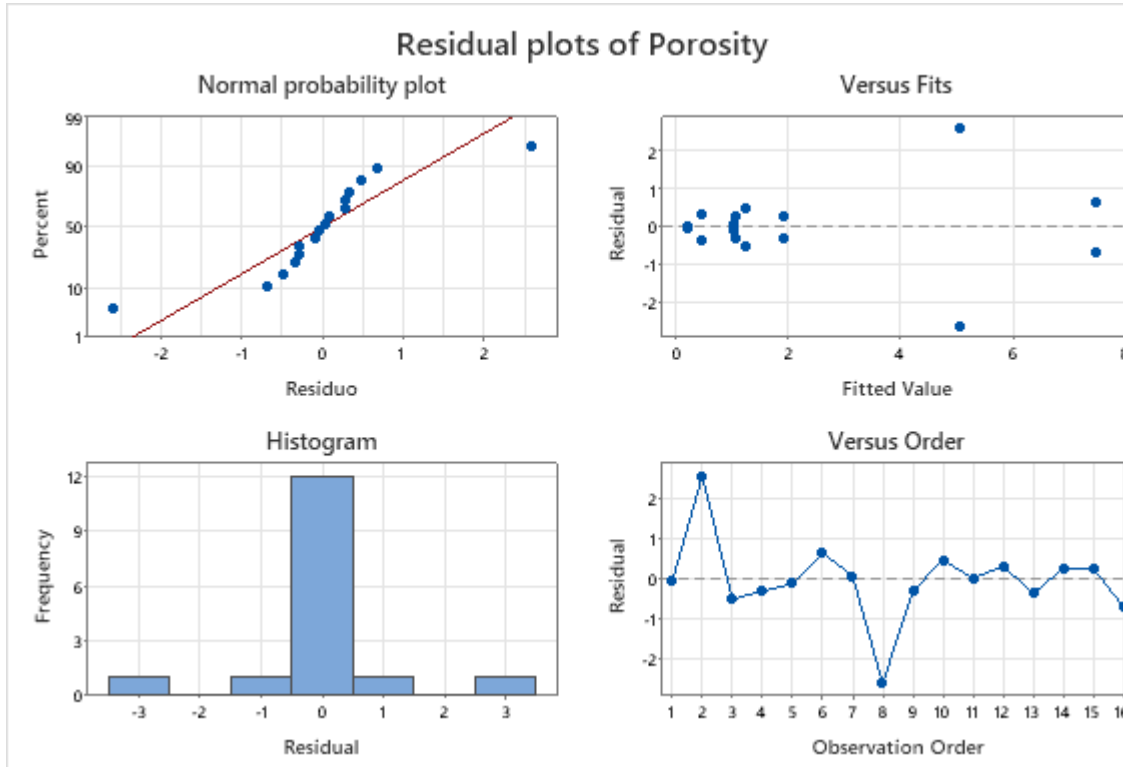


Figure 77. Residual Plots for porosity. L-PBF.

## 5.4.4 Wall Printed Samples

After an extensive study to develop parameters and analyze microstructure, texture, microhardness and soundness of the deposits, the combination of parameters of 80 W, 400 mm and 0° of rotation between layers was chosen to print a wall of 3 mm of height and 1.8 mm of thickness. This test has the purpose to simulate the repair of the squealer tip of turbine blade, a typical restoration task carried out in maintenance operations.
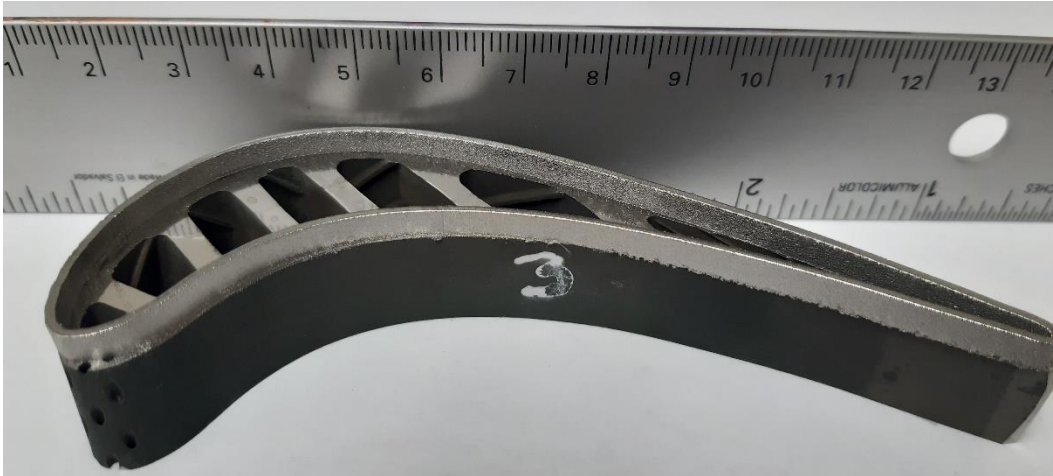
Figure 78. Wall restoration of squealer tip using L-PBF.

Visual inspection of the printed wall displays good appearance and free-defect. A stable deposit was obtained with good dimensional accuracy. This result presents a feasibility to repair turbine blades by L-PBF process.

## 5.4.5 Printing of scaled-blades

Once the possibility of carrying out a dimensional restoration on a GTD 111 specimen was validated, several blades were printed using L-PBF at a scale of 1:5. Figure 79 shows different images of the printed specimens. In Figure 79, three blades are seen in the as-built condition and attached to the build plate by the supports. Figure 79B and 79C represent a blade in different views already separated from the build plate. Small details such as cooling holes and assembly channels at the root of the blades can be seen. In Figure 79B some distortion is found at the bottom of the blade. The L-PBF technique shows great potential by obtaining fine details from the as-built condition. Three blades were built in 18 hours using the best parameters for the blade restoration.
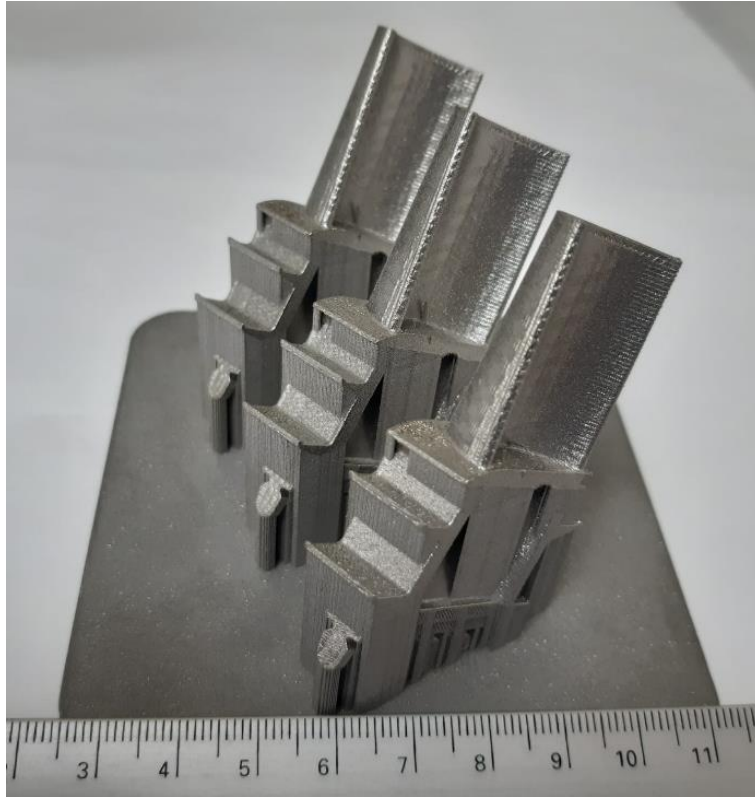
A) Scaled blades printed with Rene 65



B) Concave airfoil
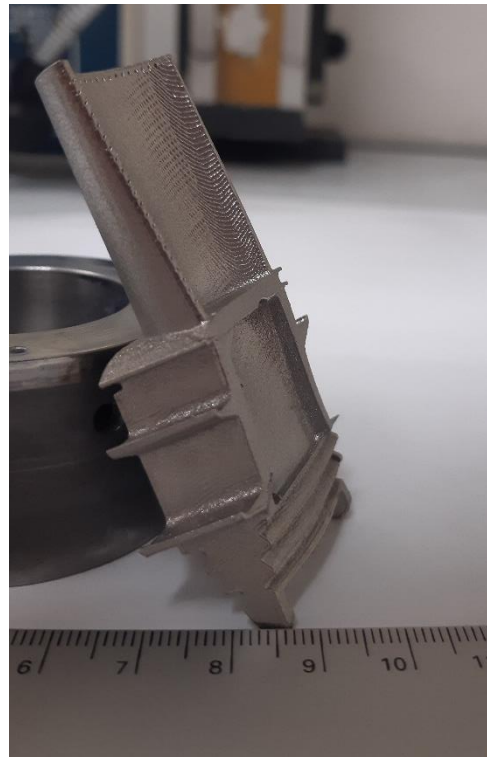


C) Side view of printed blade

Figure 79. Printed blades by L-PBF

### 5.4.6 Main Conclusions about the L-PBF process

1. The equipment used for the L-PBF process had a limited range of parameters and the size of possible impressions made. This is because the machine is designed for laboratory use. An example of this is the fixed setting of the thickness of the deposited layer (25 um). As the volume available to print is limited to 90 x 90x 90 mm.
2. When a customized build plate is used, a completely parallel surface must be ensured for both the plate and the test sample. The differences in the results of testing replicas are based on this fact.
3. Good bonding and dimensional stability with different parameters were obtained.
4. A lower hardness was obtained by L-PBF compared to the substrate GTD 111.
5. Low porosity (less 1%) was obtained using 50-400-90 and 80-400-0.
6. Generally speaking, L-PBF deposits have a highly texturized microstructure, with preferred orientation along <001>.
7. According to hardness, percent of porosity and soundness, the best combination of parameters is 80-400-0.
8. L-PBF is a slow process but the high accuracy in its deposits counteracts the use of extensive post-machining.
9. The use of L-PBF is highly recommended when high resolution must be ensured from the manufacturing process, especially in nickel base alloys that are so complex to machine.
10. In terms of future applications, L-PBF technique has great potential for the repair of gas turbine components.

## 5.5 LP-DED AND L-PBF COMPARISON

The additive manufacturing processes of L-PBF and LP-DED are compared according to the feasibility of repairing the blades of GTD 111. Both processes showed good results for the repair of the squealer tip of the blades. The resolution of the prints with L-PBF stands out, where it is possible to replicate the cooling holes. The microstructure formed with L-PBF is more directional than those achieved with LP-DED. The LP-DED process, it is worth highlighting the high speed to rebuild dimensions and its economics when compared to L-PBF. Higher hardness was obtained by LP-DED almost matching to GTD 111 hardness. Other benefit to use LP-DED was to develop more successful parameters using René 65 powder.

# CHAPTER 6: CONCLUSIONS

1. The blades used in service and studied in this work have a microstructure that is suitable to be restored for the return to operation since the nature and distribution of phases can be modified by proper heat treating. After the heat treatment, the blades must be cooled down to room temperature in air to obtain a refined microstructure. Cooling inside the furnace must be avoided.

2. It is possible to re-build the squealer tip of the degraded blades by LP-DED and L-PBF processes without pre-heating. L-PBF provides better resolution in the printed pieces and better dimensional stability. On the other hand, LP-DED is a more versatile process where the required dimensions can be restored in a faster and cheaper way. In terms of the microstructure, the deposits obtained by LP-DED have an equiaxed solidification mode while L-PBF generates more directional grains.

# CHAPTER 7: FUTURE WORK

1. Perform a homogenization treatment with a faster cooling rate (air cooling). In addition, to carry out the precipitation heat treatments to be able to know the properties with the finished repair.

2. Measure the fraction of gamma prime once the precipitation heat treatment has been carried out. In addition to the measurement in the as-built condition for the different AM processes used.

3. To ensure a directionally solidified microstructure, further experiments with narrower temperature gradients are proposed. One possibility is the use of pre-heating or use faster travel speed in LP-DED process.

4. It is recommended to use a more versatile machine with a wider range of parameters than the machine used for L-PBF. This would allow higher power values and thus reduce the extensive number of defects.

5. The qualification of the procedures developed for L-PBF and LP-DED must be carried out as well as performance tests with the parameters selected in the DOE's.

# REFERENCES

A. Lou, C. Grosvenor, Selective laser sintering, birth of an industry, http://www.me.utexas.edu/news/news/selective-laser-sintering-birth-of-an-industry. Accessed 12//2021., (2012).

American Society for Testing and Materials, "Standard Guide for Directed Energy Deposition of Metals, ASTM F3187," 2016.

American Society for Testing and Materials, "Standard Terminology for Nondestructive Examinations, ASTM E1316," vol. 02, no. June 2014. p. 39, 2019.

American Welding Society. (2010). AWS A3. 0M/A3. 0: 2010: standard welding terms and definition. and thermo-mechanical fatigue of CM247LC-DS. Warrendale, PA, USA: TMS, 1996. p.319. Astm, I. (2015).

ASTM 52900-15 standard terminology for additive manufacturing—general principles— terminology. *ASTM International, West Conshohocken, PA, 3*(4), 5.

Athiroj, A., Wangyao, P., Hartung, F., & Lothongkum, G. (2018). Low heat input welding of nickel superalloy GTD-111 with Inconel 625 filler metal. Materials Testing, 60(1), 22-30.

A. Willis and D. McCartney, "A Comparative Study of Solidification Features in Nickel-Base Superalloy: Microstructural Evolution and Microsegregation, Mat. Sci. & Eng, Vol. A 145, No.2, pp. 223-232, (1991).

Balikci, E., Raman, A., & Mirshams, R. A. (1997). Influence of various heat treatments on the microstructure of polycrystalline IN738LC. Metallurgical and Materials Transactions A, 28(10), 1993-2003.

Basak, A., (2017). Advanced Powder Bed Fusion-Based Additive Manufacturing with Turbine Engine Hot-Section Alloys through Scanning Laser Epitaxy. Dissertation.

Berahmand, M., & Sajjadi, S. A. (2012). An investigation on the coarsening behavior of γ' precipitate in GTD-111 Ni-base superalloy. Phase Transitions, 85(1-2), 1-12.

Berahmand, M., & Sajjadi, S. A. (2013). Morphology evolution of γ' precipitates in GTD-111 Ni-based superalloy with heat treatment parameters. International journal of materials research, 104(3), 275-280.

Beretta, S., & Romano, S. (2017). A comparison of fatigue strength sensitivity to defects for materials manufactured by AM or traditional processes. International Journal of Fatigue, 94, 178-191.

Biondo, C., Page, J., Samuelson, J., Fuchs, G., Stannley, T., Wlodek, R. (2016) US 2010/0080729 A1. Kansas City: U.S. Patent and Trademark Office.

Bor HY, Chao CC, Ma CY. The influence of Mg on creep properties and fracture behaviors of Mar-M247 superalloy under 1255 K/200 MPa. Metallurgical and Materials Transactions A (Physical Metallurgy and Materials Science) 2000;31:1365.

Brooks, R.B. 1982, *Heat treatment, structure and properties of nonferrous alloys.* ASM International, materials Park, OH, p. 145.

C. Deckard, J. Beaman, J. Darrah, Method for selective laser sintering with layerwise cross-scanning, in, 1986.

C. Deckard, Method and apparatus for producing parts by selective sintering, in, 1986. 204.

C. Yan, L. Hao, A. Hussein, D. Raymont, Evaluations of cellular lattice structures manufactured using selective laser melting, International Journal of Machine Tools and Manufacture, 62 (2012) 32-38.

Caiazzo, F., Alfieri, V., Cardaropoli, F., & Sergi, V. (2017). Investigation on edge joints of Inconel 625 sheets processed with laser welding. Optics & Laser Technology, 93, 180-186.

Carlota, V. Optomec Customers Have Repaired More than 10 Million Turbine Blades- Optomec. Available online: https://www.3dnatives.com/en/optomec-customer-surpass-10-million-turbine-blade-repairs-260820204/#! (accessed on 6 February 2022).

Charalampous, P., Kostavelis, I., & Tzovaras, D. (2020). Non-destructive quality control methods in additive manufacturing: a survey. Rapid Prototyping Journal.

Chen, C., Wu, H. C., & Chiang, M. F. (2008). Laser cladding in repair of IN738 turbine blades. International Heat Treatment and Surface Engineering, 2(3-4), 140-146.

Choi, B. G., Kim, I. S., Kim, D. H., & Jo, C. Y. (2008). Temperature dependence of MC decomposition behavior in Ni-base superalloy GTD 111. Materials Science and Engineering: A, 478(1-2), 329-335.

Daleo, J. A., & Wilson, J. R. (1996, June). GTD111 Alloy Material Study. In Turbo Expo: Power for Land, Sea, and Air (Vol. 78767, p. V005T12A017). American Society of Mechanical Engineers.

Daleo, J.A. and Wilson, J.R., 1998, "GTD111 alloy material study," *Journal of Engineering for Gas Turbines and Power, Transactions of the ASME*, **120**(2), pp. 375-382.

Dass, A., & Moridi, A. (2019). State of the art in directed energy deposition: From additive manufacturing to materials design. Coatings, 9(7), 418.

DebRoy, T., Wei, H. L., Zuback, J. S., Mukherjee, T., Elmer, J. W., Milewski, J. O., ... & Zhang, W. (2018). Additive manufacturing of metallic components–process, structure and properties. Progress in Materials Science, 92, 112-224.

Deng, D. (2018). Additively Manufactured Inconel 718: Microstructures and Mechanical Properties (Vol. 1798). Linköping University Electronic Press.

Donachie MJ, Donachie SJ. Superalloys: A Technical Guide. Ohio: ASM International, 2002.

DuPont , J. N. , Robino , C. V. , Marder , A. R. , Notis , M. R. , and Michael , J. R. 1988. Solidification of Nb - Bearing Superalloys: Part I. Reaction Sequences , *Metallurgical and Material Transactions A* , 29A : 2785 – 2796.

Dutta, B., Babu, S., & Jared, B. H. (2019). Science, technology and applications of metals in additive manufacturing. Elsevier.

Eisenbarth, D. (2020). *Buildup strategies for additive manufacturing by direct metal deposition* (Doctoral dissertation, ETH Zurich).

Engler-Pinto CC, Jr., Noseda C, Nazmy MY, Rezai-Aria F. Interaction between creep

F. J. Fela, "Influence of Chemical Composition Variations on the Elemental Solidification Segregation Segregation in Nickel-Base Single Crystal Superalloy", Maser's The University of Florida, May 2000.

Gandini, E., Agnesone, F., Taricco, F., & Arrighi, L. (1997, June). Advances in gas turbine blade repair by laser welding. In *Turbo Expo: Power for Land, Sea, and Air* (Vol. 78712, p. V004T12A011). American Society of Mechanical Engineers.

Groh, J., Gabb, T., Helmink, R., & Wusatowska-Sarnek, A. (2014, December). René 65 billet material for forged turbine components. In Proc. 8th Int. Symp. Superalloy 718 Deriv (p. 107). John Wiley & Sons.

Gu, D.D.; Meiners, W.; Wissenbach, K.; Poprawe, R. Laser additive manufacturing of metallic components: materials, processes and mechanisms. Int. Mater. Rev. 2012, 57, 133–164.

Hale, J. M. (1994). IGTI, vol. 9. ASME.

Hardy, M. C., Detrois, M., McDevitt, E. T., Argyrakis, C., Saraf, V., Jablonski, P. D., ... & Tin, S. (2020). Solving recent challenges for wrought Ni-base superalloys. *Metallurgical and Materials Transactions A*, *51*(6), 2626-2650.

Heaney, J.A.; Lasonde, M.L.; Powell, A.M.; Bond, B.J.; O'Brien, C.M. Development of a New Cast and Wrought Alloy (Rene 65) for High Temperature Disk Applications. In Proceedings of the 8th International Symposium on Superalloy 718 and Derivatives, Pittsburgh, PA, USA, 28 September–1 October 2014.

https://www.3dsystems.com/our-story. Accesed 12/2/2021

https://www.eos.info/about_eos/history. Accesed 12/2/2021

Huarte-Mendicoa, L., Penaranda, X., Lamikiz, A., & Moralejo, S. (2019). Experimental Microstructure Evaluation of Rene 80 in Laser Cladding. Lasers in Manufacturing and Materials Processing, 6(3), 317-331.

Ian Gibson, I. G. (2015). Additive manufacturing technologies 3D printing, rapid prototyping, and direct digital manufacturing.

Ion, J. C. (2005). Laser processing of engineering materials. principles, procedure and industrial application. Chapter 12–Cladding.

ISO/ASTM52900-15 (2015) Standard terminology for additive manufacturing—general principles—terminology. ASTM International, West Conshohocken.

J. Johnson and M. J. Donachie, Microstructure of Precipitation Strengthened Nickel-Base Superalloys, in National Metal Congress, Chicago, 1966.

J. Kranz, D. Herzog, Design guidelines for laser additive manufacturing of lightweight structures in TiAl6V4, Journal of Laser Applications, 27 (2015).

J.K. Tien, Superalloys, Supercomposites and Superceramics, Elsevier, 2012.

J.R. Davis, ASM Specialty Handbook: Heat-Resistant Materials, ASM International, Ohio, 1997

Jena, A., Atabay, S. E., Gontcharov, A., Lowden, P., & Brochu, M. (2021). Laser powder bed fusion of a new high gamma prime Ni-based superalloy with improved weldability. Materials & Design, 208, 109895.

Jones, J. B., McNutt, P., Tosi, R., Perry, C., & Wimpenny, D. I. (2012). Remanufacture of turbine blades by laser cladding, machining and in-process scanning in a single machine.

Jovanović, M. T., Mišković, Z., & Lukić, B. (1998). Microstructure and stress-rupture life of polycrystal, directionally solidified, and single crystal castings of nickel-based IN 939 superalloy. Materials characterization, 40(4-5), 261-268.

Kaplanskii, Y. Y., Levashov, E. A., Korotitskiy, A. V., Loginov, P. A., Sentyurina, Z. A., & Mazalov, A. B. (2020). Influence of aging and HIP treatment on the structure and properties of NiAl-based turbine blades manufactured by laser powder bed fusion. Additive Manufacturing, 31, 100999.

Keicher, D. M., Smugeresky, J. E., Romero, J. A., Gri_th, M. L., Harwell, L. D. (1997). Using the laser engineered net shaping (lens) process to produce complex components from a cad solid model. Photonics West. SPIE Vol. 2993, pp. 91-97.

Keshavarz, M. K., Gontcharov, A., Lowden, P., Chan, A., Kulkarni, D., & Brochu, M. (2021). Turbine Blade Tip Repair by Laser Directed Energy Deposition Additive Manufacturing Using a Rene 142–MERL 72 Powder Blend. Journal of Manufacturing and Materials Processing, 5(1), 21.

Kountras, A. (2004). Metallographic study of gamma-gamma prime structure in the Ni-based superalloy GTD111 (Doctoral dissertation, Massachusetts Institute of Technology).

Lawrence, J. R. (Ed.). (2017). Advances in laser materials processing: technology, research and applications. Woodhead Publishing.

Lewandowski, J. J., & Seifi, M. (2016). Metal additive manufacturing: a review of mechanical properties. Annual review of materials research, 46, 151-186.

Lewis, G., Nemec, R., Milewski, J., Thoma, D., Cremers, D., Barbe, M. (1994). Directed light fabrication. Applications of Lasers and Electro-Optics.

Li, L., 2006, "Repair of directionally solidified superalloy GTD-111 by laser-engineered net shaping," *Journal of Materials Science*, **41**(23), pp. 7886-7893.

Li, L., Deceuster, A., & Zhang, C. (2012). Effect of process parameters on pulsed-laser repair of a directionally solidified superalloy. Metallography, Microstructure, and Analysis, 1(2), 92-98.

Li, X. W., Wang, L., Dong, J. S., & Lou, L. H. (2014). Effect of solidification condition and carbon content on the morphology of MC carbide in directionally solidified nickel-base superalloys. Journal of Materials Science & Technology, 30(12), 1296-1300.

Lifshitz, I. M. and Sloyozov, V.V. 1961. The kinetics of precipitation from supersaturated solid solutions, *Journal of Physical Chemistry of Solids*, 19 (1 − 2 ): 35 − 50.

Lippold, J. C. (2014). Welding metallurgy and weldability. John Wiley & Sons.

Liu, Y., Li, Y., & Peng, H. (2010, March). Laser net shape manufacturing of Rene80. In Pacific International Conference on Applications of Lasers and Optics (Vol. 2010, No. 1, p. 609). Laser Institute of America.

Liu, Z. Y., Li, C., Fang, X. Y., & Guo, Y. B. (2018). Energy consumption in additive manufacturing of metal parts. Procedia Manufacturing, 26, 834-845.

M. Seifi, A. Salem, J. Beuth, O. Harrysson, J. Lewandowski, Overview of materials characterization needs for metal additive manufacturing, Journal of Materials, 68 (2016) 747-764.

M. Durand-Charee, "The Microstructure of Superalloys", Gordon and Breach Science Publishers, Toronto, Canada, p. 60-69, (1997).

M. Gell, D.N. Duhl, K. Gupta, and K Sheffler, "Advanced Superalloys Airfoils", Journal of Metals, Vol. 39, No. 7, pp.11-15, (1987).

Mazumder, J., Choi, J., Nagarathnam, K., Koch, J., Hetzner, D. (1997). The direct metal deposition of h13 tool steel for 3-d components. JOM 49 (5), pp. 55-60.

Melia, M. A., Whetten, S. R., Puckett, R., Jones, M., Heiden, M. J., Argibay, N., & Kustas, A. B. (2020). High-throughput additive manufacturing and characterization of refractory high entropy alloys. Applied Materials Today, 19, 100560.

Olufayo, O. A., Che, H., Songmene, V., Katsari, C., & Yue, S. (2019). Machinability of Rene 65 superalloy. *Materials*, *12*(12), 2034.

Pauzi, A. A., Berahim, N., & Husin, S. (2016). Degradation of Gas Turbine Blades for a Thermal Power Plant. In *MATEC Web of Conferences* (Vol. 54, p. 03002). EDP Sciences.

Popovich, V. A., Borisov, E. V., Popovich, A. A., Sufiiarov, V. S., Masaylo, D. V., & Alzina, L. (2017). Functionally graded Inconel 718 processed by additive manufacturing: Crystallographic texture, anisotropy of microstructure and mechanical properties. Materials & Design, 114, 441-449.

Qi, H., Azer, M., & Singh, P. (2010). Adaptive toolpath deposition method for laser net shape manufacturing and repair of turbine compressor airfoils. The International Journal of Advanced Manufacturing Technology, 48(1), 121-131.

R. Baker, Method of making decorative articles, in, Westinghouse Electric & Mfg Co, 1920.

Rehme, O., & Emmelmann, C. (2005, June). Reproducibility for properties of selective laser melting products. In Proceedings of the Third International WLT-Conference on Lasers in Manufacturing (pp. 227-232). Proc. Third Int. WLT-Conference Lasers Manuf. Munich.

Rittinghaus, S. K., Schmelzer, J., Rackel, M. W., Hemes, S., Vogelpoth, A., Hecht, U., & Weisheit, A. (2020). Direct energy deposition of TiAl for hybrid manufacturing and repair of turbine blades. Materials, 13(19), 4392.

Rolls-Royce plc, The Jet Engine, 4th edn (Derby, UK: The Technical Publications Department, Rolls-Royce plc, 1992).

Sajjadi, S. A., and Nategh, S., 2001, "A High Temperature Deformation Mechanism Map for the High Performance Ni-Base Superalloy GTD-111," *Materials Science and Engineering A*, **307**(1-2), pp. 158-164.

Sajjadi, S. A., Nategh, S., & Guthrie, R. I. (2002). Study of microstructure and mechanical properties of high performance Ni-base superalloy GTD-111. Materials Science and Engineering: A, 325(1-2), 484-489.

Sajjadi, S. A., Zebarjad, S. M., Guthrie, R. I. L., & Isac, M. (2006). Microstructure evolution of high-performance Ni-base superalloy GTD-111 with heat treatment parameters. Journal of materials processing technology, 175(1-3), 376-381.

Scheibel, J. R., Aluru, R., & Van Esch, H. (2018, June). Mechanical Properties in GTD-111 Alloy in Heavy Frame Gas Turbines. In Turbo Expo: Power for Land, Sea, and Air (Vol. 51128, p. V006T24A009). American Society of Mechanical Engineers.

Schilke, P. W., Foster, A.D., Pepe, J. J., and Beltran, A. M., 1992, "Advanced Materials Propel Progress in LAND-BASED GAS TURBINES," *Advanced Materials and Processes*, **141**(4), pp. 22-30.

Schilke, P.W., 2004, "Advanced Gas Turbine Materials and Coatings," GE ENERGY, Schenectady, NY.

Sims CT. Contemporary view of nickel-base superalloys. Journal of Metals 1966;18:1119.

Smallman, R. E. and Bishop, R. J., 1999, *Modern physical metallurgy and materials engineering: science, process, applications*, Butterworth-Heinemann, pg 46-47.

Sosa, J. M., Huber, D. E., Welk, B. A., & Fraser, H. L. (2017). MIPAR™: 2D and 3D Image Analysis Software Designed by Materials Scientists, for All Scientists. Microscopy and Microanalysis, 23(S1), 230-231.

Standard, A. S. T. M. (2012). Standard terminology for additive manufacturing technologies. ASTM International F2792-12a.

Stewart, C. (2009). Tertiary creep damage modeling of a transversely isotropic Ni-based superalloy.

Sun, W. R., Lee, J. H., Seo, S. M., Choe, S. J., & Hu, Z. Q. (1999). The eutectic characteristic of MC-type carbide precipitation in a DS nickel-base superalloy. Materials Science and Engineering: A, 271(1-2), 143-149.

T. Wohlers, T. Gornet, History of additive manufacturing, Wohlers Report 2014, (2014).

T.M. Pollock, S. Tin, Nickel-based superalloys for advanced turbine engines: chemistry, microstructure and properties, Journal of propulsion and power, 22 (2006) 361-374.

Thiesen Junior, A. (2021). Selection of processing parameters for the laser directed energy deposition process applied to additive manufacturing: a methodological proposal.

Thornton, P. H. Davies , P. H. , and Johnston , T. L. 1970 . Temperature dependence of the fl ow stress of the gamma prime phase based upon Ni 3 Al , *Metallurgical Transactions A* , 1 ( 1 ): 207 − 218.)

Toyserkani, E., Khajepour, A., & Corbin, S. F. (2004). Laser cladding. CRC press.

Turazi, A., de Oliveira, C. A. S., Bohórquez, C. E. N., & Comeli, F. W. (2015). Study of GTD-111 superalloy microstructural evolution during high-temperature aging and after rejuvenation treatments. Metallography, Microstructure, and Analysis, 4(1), 3-12.

Ünal-Saewe, T., Gahn, L., Kittel, J., Gasser, A., & Schleifenbaum, J. H. (2020). Process development for tip repair of complex shaped turbine blades with IN718. Procedia Manufacturing, 47, 1050-1057.

Villada, J. A., Bayro-Lazcano, R. G., Martinez-Franco, E., Espinosa-Arbelaez, D. G., Gonzalez-Hernandez, J., & Alvarado-Orozco, J. M. (2019). Relationship between γ' phase degradation and in-Service GTD-111 first-stage blade local temperature. Journal of Materials Engineering and Performance, 28(4), 1950-1957.

Viswanathan, R., and Scheirer, S. T., 1998, "Materials Advances in Land-Based Gas Turbines," *POWER-GEN 1998 Conference*, Orlando, FL.

Wangyao, P., Krongtong, V., Tuengsook, P., Hormkrajai, W., & Panich, N. (2006). The relationship between reheat-treatment and hardness behaviour of cast nickel superalloy, GTD-111. Journal of Metals, Materials and Minerals, 16(1).

Wangyao, P., Phansri, L., Hirisatja, P., Saelor, K., Zrník, J., & Novy, Z. (2015). Effect of Precipitation Aging Conditions on Microstructural Refurbishment in Cast Nickel Base Superalloy GTD-111. In Advanced Materials Research (Vol. 1127, pp. 79-84). Trans Tech Publications Ltd.

Wangyao, P., Polsilapa, S., Chaishom, P., Zrnik, J., Homkrajai, W., & Panich, N. (2008). Gamma prime particle coarsening behavior at elevated temperatures in cast nickel-based superalloy, GTD-111 EA. High Temperature Materials and Processes, 27(1), 41-50.

Wangyao, P., Suvanchai, P., Chuankrerkkul, N., Krongtong, V., Thueploy, A., & Homkrajai, W. (2010). Microstructural analysis after reheat treatments and long-term heating in cast nickel base superalloy, GTD-111. High Temperature Materials and Processes, 29(4), 277-286.

Wessman A, Laurence A, Cormier J, Villechaise P, Billot T, Franchet J-M (2016) Thermal stability of cast and wrought alloy Rene 65. Proceedings of the International Symposium on Superalloys.

Wessman, A. E. (2016). *Physical Metallurgy of Rene 65, a Next-Generation Cast and Wrought Nickel Superalloy for use in Aero Engine Components* (Doctoral dissertation, University of Cincinnati).

Wessman, A., Cormier, J., Hamon, F., Rainey, K., Tin, S., Tiparti, D., & Dial, L. (2020). Microstructure and Mechanical Properties of Additively Manufactured Rene 65. In *Superalloys 2020* (pp. 961-971). Springer, Cham.

Wilson, J. M., Piya, C., Shin, Y. C., Zhao, F., & Ramani, K. (2014). Remanufacturing of turbine blades by laser direct deposition with its energy and environmental impact analysis. Journal of Cleaner Production, 80, 170-178.

Wohlers, T., Campbell, I., Diegel, O., Kowen, J., Fidan, I., Bourell, D. (2018). Wohlers Report 2018. Wohlers Associates, Fort Collins.

Xue, L., Chen, J. Y., Islam, M. U., Pritchard, J., Manente, D., & Rush, S. (2000, October). Laser consolidation of Ni-base IN-738 superalloy for repairing gas turbine blades. In International Congress on Applications of Lasers & Electro-Optics (Vol. 2000, No. 1, pp. D30-D39). Laser Institute of America.

Yilmaz, O., Gindy, N., & Gao, J. (2010). A repair and overhaul methodology for aeroengine components. Robotics and Computer-Integrated Manufacturing, 26(2), 190-201.

Zhang, X., Chai, Z., Chen, H., Xu, J., Xu, L., Lu, H., & Chen, X. (2021). A novel method to prevent cracking in directed energy deposition of Inconel 738 by in-situ doping Inconel 718. Materials & Design, 197, 109214.

# APPENDIX I

Technical data of the TrueLaser Cell 3000 machine

| Technical data | | |
|---|---|---|
| **Working range** | | |
| Linear axes X\|Y\|Z | 800\|600\|400 mm | |
| Swivel axis | ± 135° | |
| Rotating axis | n x 360° | |
| Max. workpiece dimensions 2D | 800 mm x 600 mm | |
| Max. processing volume 3D | 420 mm x 420 mm x 220 mm (ø 916 mm) | |
| | **Axis speed** | **Axis acceleration** |
| Simultaneous | 85 m/min | 17 m/s² |
| Linear axes X\|Y\|Z | 50 m/min | 10 m/s² |
| Rotating axes B \| C | 120\|800 min$^{-1}$ | 130\|500 rad/s² |
| **Positional deviation Pa[1]** | | |
| Linear axes X\|Y\|Z | 0.015 mm | |
| Rotating axes B \| C | 0.03° | |
| **Rotary changer** | | |
| Diameter of rotary table | 1070 mm | |
| Working height | 870 mm | |
| Max. weight supported on each side | 95 kg, pitch circle diameter of 650 mm | |
| Time to completely rotate the rotary changer | 3.4 s | |
| **Dimensions of machine** | | |
| Width\|Depth\|Height | 1600\|2840\|2645 mm | |
| **TRUMPF Laser** | | |
| Max. laser output | 8000 W | |
| Available solid-state lasers | TruPulse, TruFiber, TruDisk, TruDiode | |

[1] Corresponds to "mean bidirectional positional deviation M". Measured at the tool center point (TCP) of the processing optics. The accuracy of the value given assumes a working length of 300 mm and represents an acceptance criterion for delivery.

# APPENDIX II

Technical data of the Concept Laser Mlab machine

## Technical Data

| | Concept Laser Mlab |
|---|---|
| Build envelope | 50 x 50 x 80 mm (x,y,z) |
| | 70 x 70 x 80 mm (x,y,z) |
| | 90 x 90 x 80 mm (x,y,z) |
| Layer thickness | 15 – 30 µm |
| Production speed | 1 – 5 cm3/h (depending on material) |
| Laser system | Fibre laser 100 W (cw)) |
| Max. scanning speed | 7 m/s |
| Focus diameter | approx. 50 µm |
| Connected loads | Power consumption 1.5 kW |
| | Power supply 1/N/PE AC 230 V, 16 A |
| Inert gas supply | 1 gas connection provided / Nitrogen or Argon |
| Inert gas consumption | approx. 0.6 – 0.8 l/min* |
| Machine dim: | 705 x 1848 x 1220 mm (W x H x D) |
| Handling station dims: | N/A |
| Machine weight | approx. 600 kg |
| Handling station weight | N/A |
| Operating conditions | 15 – 30°C |
| Materials available | Stainless Steel 316L |
| | Stainless Steel 17-4PH |
| | Bronze CuSn |
| | remanium star® CL (CoCrW) |
| | Silver 930 |
| | Gold, Yellow |
| | Gold, Rose |
| | Platinum |

# APPENDIX III

Single layers on GTD 111 printed by René 65
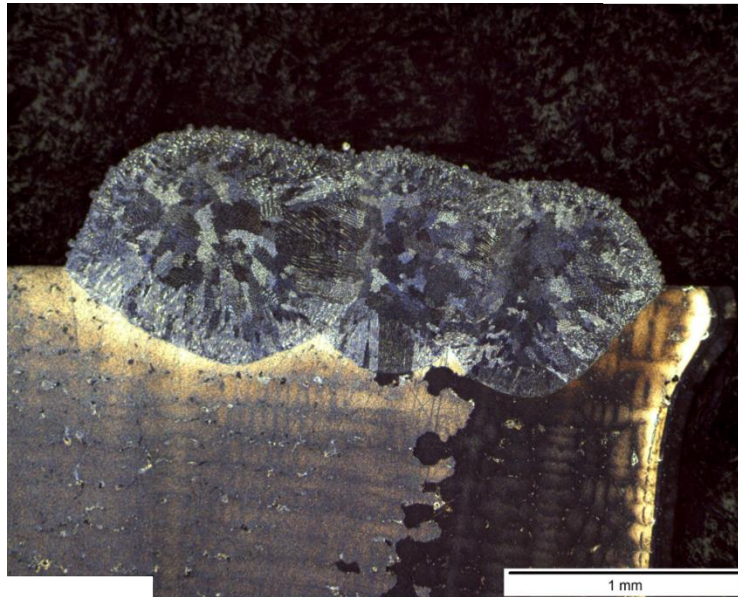


A) #30 (250 W-450 mm/min)
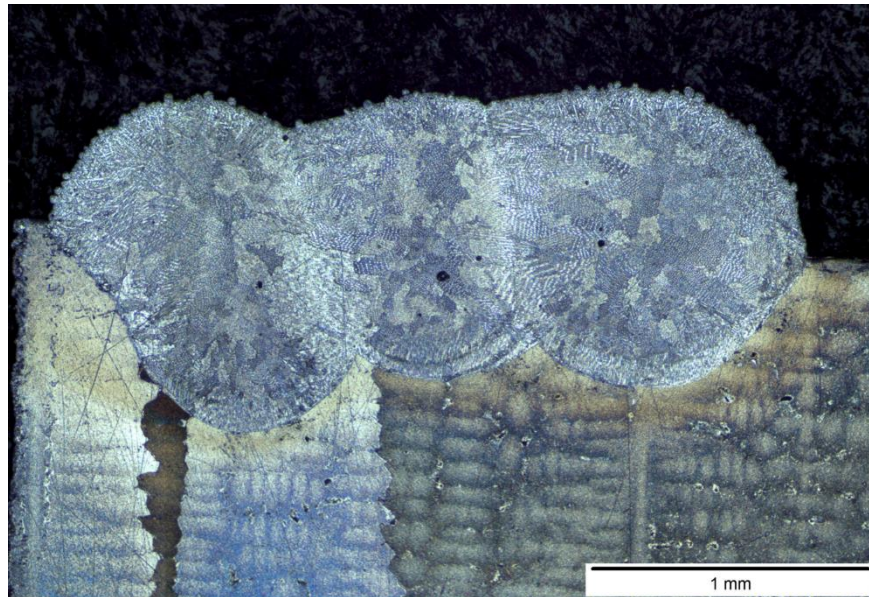


B) #26 (300 W-450 mm/min)
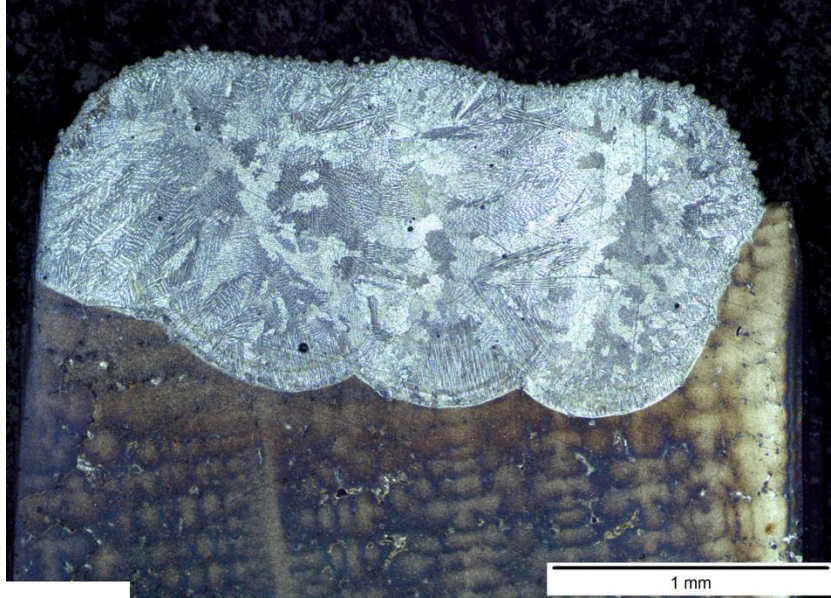
C) #28 (350W-450 mm/min)
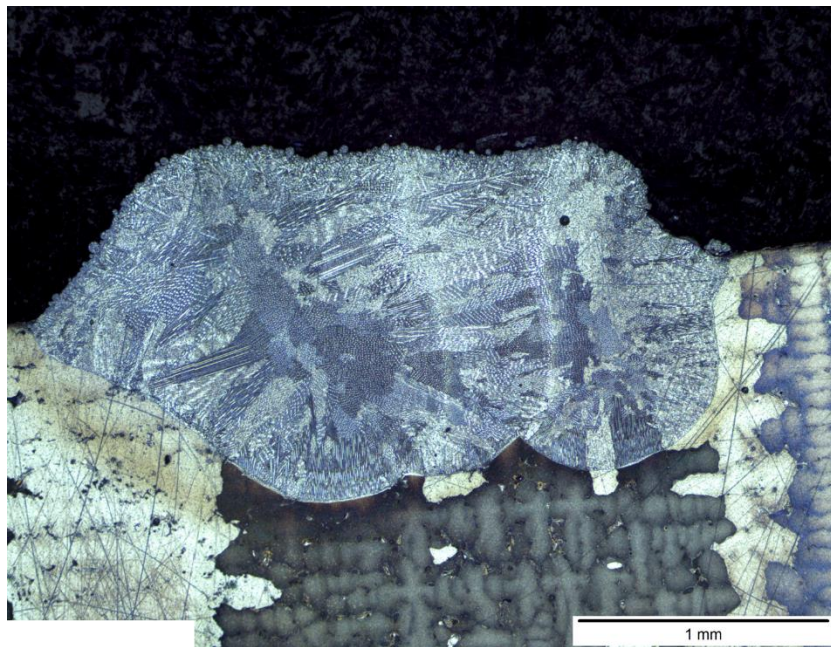

D) #4 (400 W-450 mm/min)
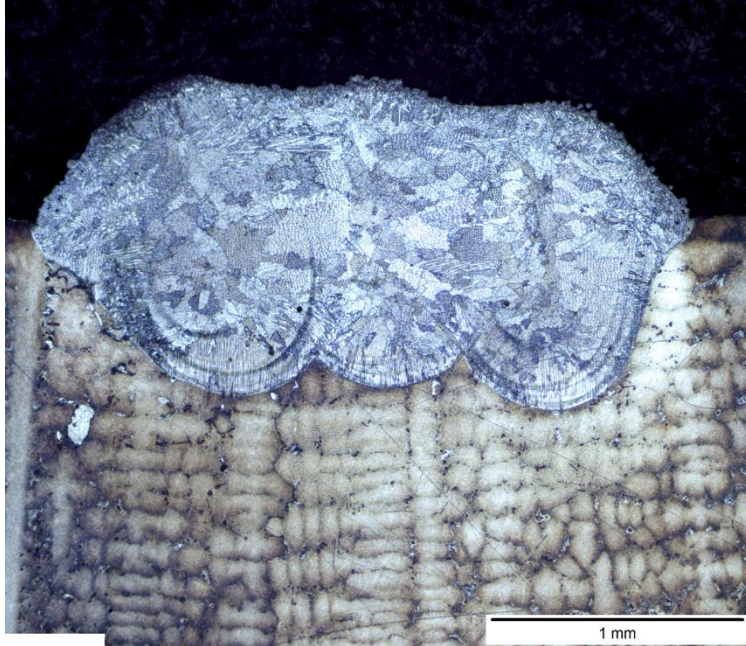
E)  #5 (400 W-550 mm/min)



F)  500 W – 350 mm/min
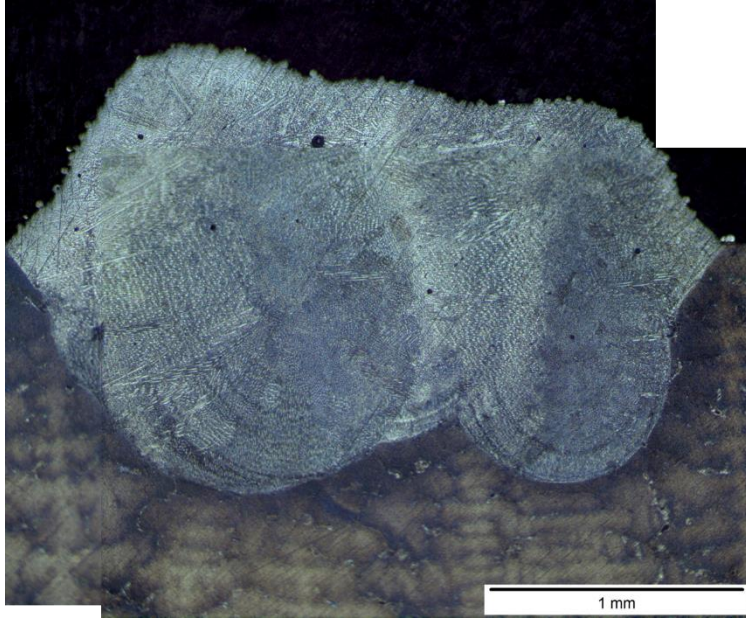
G)   500 W – 450 mm/min

# APPENDIX IV

Spectrum of the matrix gamma

| Element | Weight% | Atomic% |
|---------|---------|---------|
| C K     | 7.38    | 27.34   |
| O K     | 0.46    | 1.27    |
| Al K    | 1.55    | 2.56    |
| Ti K    | 2.70    | 2.50    |
| Cr K    | 16.02   | 13.71   |
| Co K    | 10.79   | 8.15    |
| Ni K    | 57.52   | 43.60   |
| W M     | 3.59    | 0.87    |
|         |         |         |
| Totals  | 100.00  |         |



10μm          Electron Image 1



Full Scale 1005 cts  Cursor: 0.508 keV (45 cts)
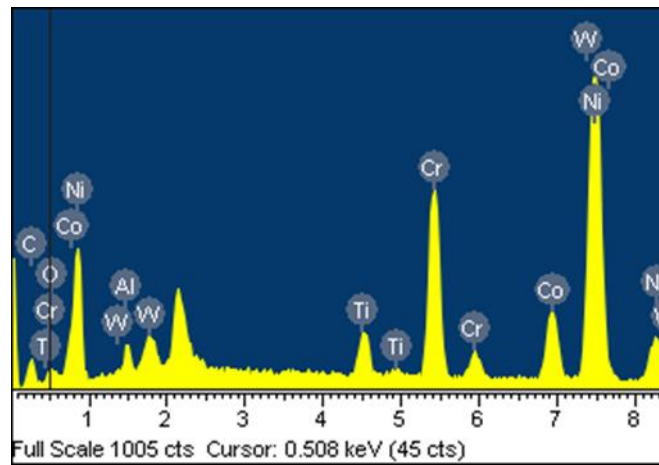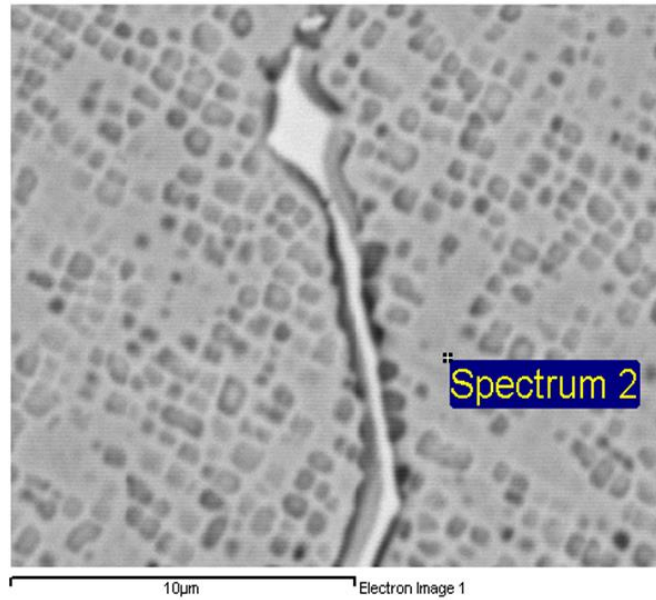
# APPENDIX V

Spectrum result of gamma primme



| Element | Weight% | Atomic% |
|---------|---------|---------|
| C K | 3.00 | 12.92 |
| Al K | 1.35 | 2.59 |
| Ti K | 4.24 | 4.58 |
| Cr K | 11.71 | 11.67 |
| Co K | 8.77 | 7.71 |
| Ni K | 67.47 | 59.55 |
| Ta M | 1.52 | 0.44 |
| W M | 1.95 | 0.55 |
| Totals | 100.00 | |
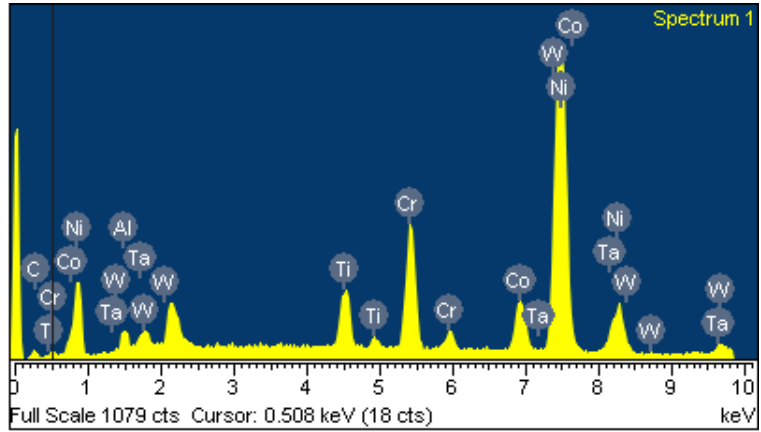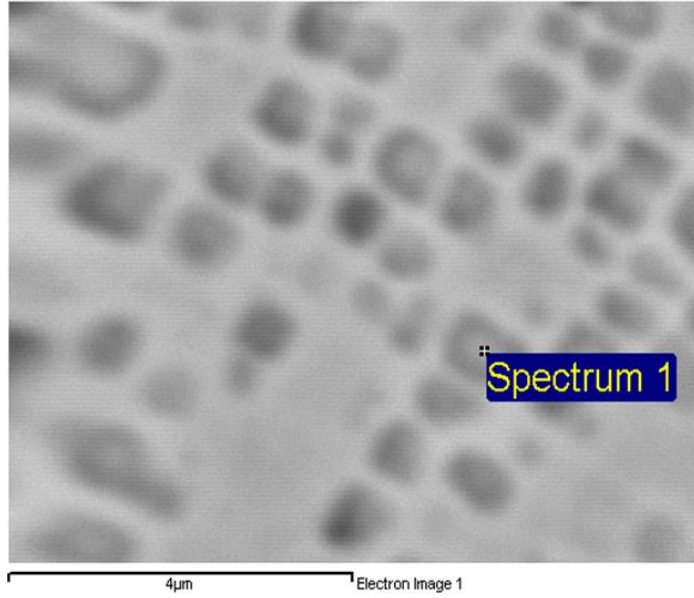
# APPENDIX VI

NC programing of TrumpF Trulaser Cell 3000

<u>Preliminary test of René 65 on 316</u>

```
;TrulaserCell 3000
;Base metal GTD 111. Powder René 65. Single layer
; Rene 65 in Hopper 1
TC_RESET
G71
TC_DYNAMIC_LEVEL(0)
SET_G54 (X, Y, Z)
G90
F=5000
G500
G01 Z = 400.00
G54
M00
X0 Y0 F = 1500
m0
Z0
R199=0
R200=5
f1500
Y-15 ; ST 1
TC_LMD_ON("R65ST1",0); SET TECHNOLOGY TABLE
Y15
TC_LMD_OFF(1)
X7; ST 13
TC_LMD_ON("R65ST13",0)
Y-15
TC_LMD_OFF(1)
X14 ; ST 14
TC_LMD_ON("R65ST14",0)
Y15
TC_LMD_OFF(1)
X21 ; ST 15
TC_LMD_ON("R65ST15",0)
Y-15
TC_LMD_OFF(1)
X28; ST 16
TC_LMD_ON("R65ST16",0)
Y15
TC_LMD_OFF(1)
X35 ; ST 17
TC_LMD_ON("R65ST17",0)
Y-15
TC_LMD_OFF(1)
```

```
X42; ST 18
TC_LMD_ON("R65ST18",0)
Y15
TC_LMD_OFF(1)
X49 ; ST 19
TC_LMD_ON("R65ST19",0)
Y-15
TC_LMD_OFF(1)
X56; ST 20
TC_LMD_ON("R65ST20",0)
Y15
TC_LMD_OFF(1)
X63 ; ST 21
TC_LMD_ON("R65ST21",0)
Y-15
TC_LMD_OFF(1)
x70; ST 22
TC_LMD_ON("R65ST22",0)
Y15
TC_LMD_OFF(1)
X77 ; ST 23
TC_LMD_ON("R65ST23",0)
Y-15
TC_LMD_OFF(1)
X84 ; ST 24
TC_LMD_ON("R65ST24",0)
Y15
TC_LMD_OFF(1)
X56Y-21 ;ST 25
TC_LMD_ON("R65ST25",0)
X26
TC_LMD_OFF(1)
X0Y21
TC_LMD_ON("R65ST9",0)
Y36
X0.8
Y21
X1.6
Y36
X2.4
Y21
TC_LMD_OFF(1)
X12
TC_LMD_ON("R65ST9",0)
Y36
X12.8
Y21
X13.6
Y36
X14.4
Y21
```

```
TC_LMD_OFF(1)
Z0.5
X12
TC_LMD_ON("R65ST9",0)
Y36
X12.8
Y21
X13.6
Y36
X14.4
Y21
TC_LMD_OFF(1)
Z1
X12
TC_LMD_ON("R65ST9",0)
Y36
X12.8
Y21
X13.6
Y36
X14.4
Y21
TC_LMD_OFF(1)
Z1.5
X12
TC_LMD_ON("R65ST9",0)
Y36
X12.8
Y21
X13.6
Y36
X14.4
Y21
TC_LMD_OFF(1)
Z2
X12
TC_LMD_ON("R65ST9",0)
Y36
X12.8
Y21
X13.6
Y36
X14.4
Y21
TC_LASER_OFF(2)
TC_RESET
M30
```

## Single beads on GTD 111

```
;TrulaserCell 3000
```

```
;Base metal GTD 111. Powder René 65. Single tracks
; Rene 65 in Hopper 1
TC_RESET
G71
TC_DYNAMIC_LEVEL(0)
SET_G54 (X, Y, Z)
G90
F=5000
G500
G01 Z = 400.00
G54

M00

X0 Y0 f1500
m0
Z0

R199=0
R200=5

f1500
X2 ; ST 1
TC_LMD_ON("R65ST9",0); SET TECHNOLOGY TABLE
X17
TC_LMD_OFF(2)
TC_RESET
m30
```

## Single Layer of René 65 on GTD 111

```
;TrulaserCell 3000
;Base metal GTD 111. Powder René 65 Hopper 1.
TC_RESET
G71
TC_DYNAMIC_LEVEL(0)
SET_G54 (X, Y, Z)
G90
F=5000
G500
G01 Z = 400.00
G54
M00
X0 Y0 F = 1500
m0
Z0
R199=0
R200=5
f1500
TC_LMD_ON("R65ST4",0); SET TECHNOLOGY TABLE
X7
```

```
Y0.7
X0
Y2.4
X7
TC_LMD_OFF(1)
TC_LASER_OFF(2)
TC_RESET
M30
```

## Multilayer of René 65 on GTD 111 0° rotation between layer

```
;TrulaserCell 3000
;Base metal GTD 111. Powder René 65 Hopper 1. Multilayer Unidirectional
TC_RESET
G71
TC_DYNAMIC_LEVEL(0)
SET_G54 (X, Y, Z)
G90
F=5000
G500
G01 Z = 400.00
G54
M00
X0 Y0 F = 1500
m0
Z0
R199=0
R200=5
f1500
TC_LMD_ON("R65ST4",0); SET TECHNOLOGY TABLE
X8
Y0.7
X0
Y1.4
X8
Y2.1
X0
TC_LMD_OFF(1)
Z0.65
X0Y0
TC_LMD_ON("R65ST4",0)
X8
Y0.7
X0
Y1.4
X8
Y2.1
X0
TC_LMD_OFF(1)
Z1.3
X0Y0
```

```
TC_LMD_ON("R65ST4",0)
X8
Y0.7
X0
Y1.4
X8
Y2.1
X0
TC_LMD_OFF(1)
Z1.95
X0Y0
TC_LMD_ON("R65ST4",0)
X8
Y0.7
X0
Y1.4
X8
Y2.1
X0
TC_LMD_OFF(1)
Z2.6
X0Y0
TC_LMD_ON("R65ST4",0)
X8
Y0.7
X0
Y1.4
X8
Y2.1
X0
TC_LASER_OFF(2)
TC_RESET
M30
```

## Multilayer of René 65 on GTD 111 180° rotation between layer

```
;TrulaserCell 3000
;Base metal GTD 111. Powder René 65 Hopper 1. Multilayer Bidirectional
TC_RESET
G71
TC_DYNAMIC_LEVEL(0)
SET_G54 (X, Y, Z)
G90
F=5000
G500
G01 Z = 400.00
G54
M00
X0 Y0 F = 1500
m0
Z0
```

```
R199=0
R200=5
f1500
TC_LMD_ON("R65ST4",0); SET TECHNOLOGY TABLE
X8
Y0.7
X0
Y1.4
X8
Y2.1
X0
TC_LMD_OFF(1)
Z0.65
X8Y0
TC_LMD_ON("R65ST4",0)
X0
Y0.7
X8
Y1.4
X0
Y2.1
X8
TC_LMD_OFF(1)
Z1.3
X0Y0
TC_LMD_ON("R65ST4",0)
X8
Y0.7
X0
Y1.4
X8
Y2.1
X0
TC_LMD_OFF(1)
Z1.95
X8Y0
TC_LMD_ON("R65ST4",0)
X0
Y0.7
X8
Y1.4
X0
Y2.1
X8
TC_LMD_OFF(1)
Z2.6
X0Y0
TC_LMD_ON("R65ST4",0)
X8
Y0.7
X0
```

Y1.4
X8
Y2.1
X0
TC_LASER_OFF(2)
TC_RESET
M30

## Rebuild a squealer tip using René 65 on GTD 111

```
N10;TrulaserCell 3000
N20;On GTD 111 blade. Powder René 65. Build-up wall
N30; Rene 65 in Hopper 1
N40TC_RESET
N50G71; Unit mm
N60G17
N70TC_DYNAMIC_LEVEL(0)
N80SET_G54 (226.913,475.286,232.042)
N90G90
N100F=5000
N110G500
N120G01 Z = 400.00
N130G54
N140
N150M00
N160
N170X0 Y0 f1500
N180m0
N190Z0
N200
N210R199=0
N220R200=5
N230
N240f1500
N250G17
M0
N260Z1.95
N270TC_LMD_ON("R65ST26",0); SET TECHNOLOGY TABLE
N280G01 X13.5 Y-1.67
N290G01 X22.467 Y-2.659
N300CIP I1=29.67 J1=-3.18 X43.24 Y-3.40
N310CIP I1=54.84 J1=-2.67 X64.68 Y-1.42
N320CIP I1=73.85 J1=1.133 X85.45 Y7.72
N330CIP I1=92.40 J1=16.87 X95.19 Y30.63
N340CIP I1=94.32 J1=39 X89.82 Y52.73
N350CIP I1=86.95 J1=58.02 X83.68 Y61.89
N360CIP I1=78.75 J1=64.48 X73.85 Y58.99
N370CIP I1=74.32 J1=51.26 X74.52 Y44.34
N380CIP I1=72.99 J1=34.59 X67.39 Y24.38
N390CIP I1=59.87 J1=17.29 X49.53 Y11.70
N400CIP I1=41.45 J1=9 X24.62 Y5.28
```

```
N410CIP I1=15.23 J1=4.34 X-0.008 Y3.32
N420CIP I1=-1.205 J1=1.42 X-0.925 Y0.474
N430CIP I1=-0.756 J1=0.246 X0 Y0
N440TC_LMD_OFF(2)
N450TC_RESET
N460m30
```

# APPENDIX VII

Unetched samples-Cross section of L-DED samples
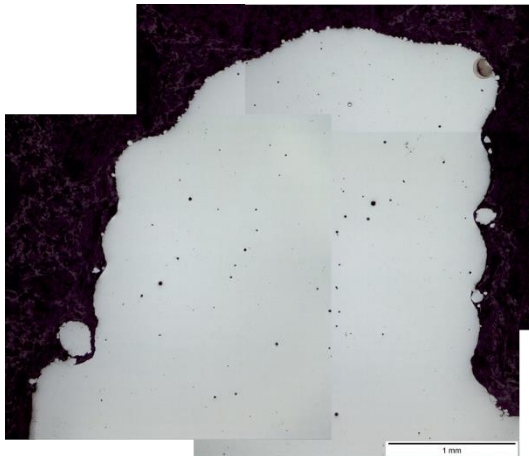


300-450-0-A
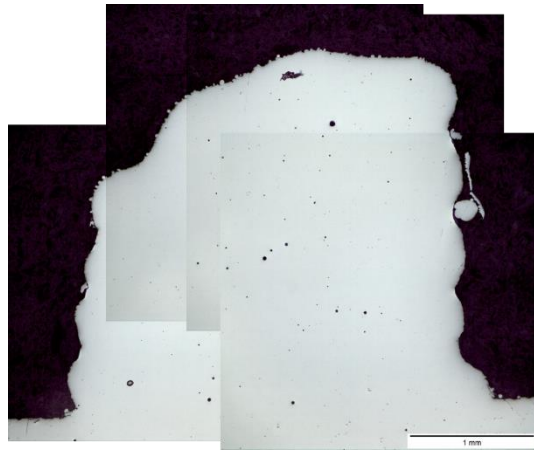


300-450-0-B
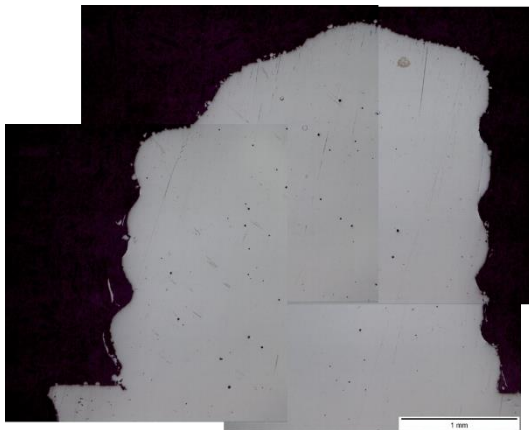


300-450-180-A
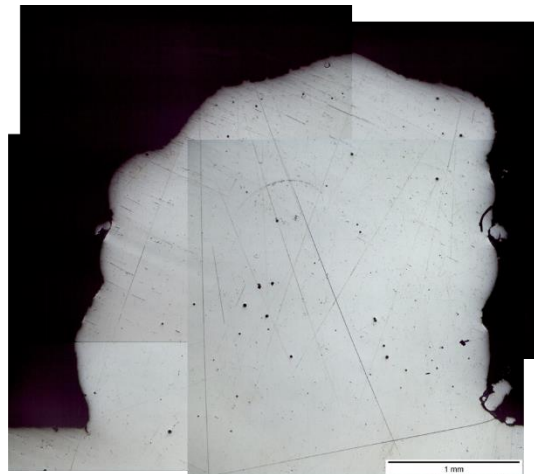


300-450-180-B
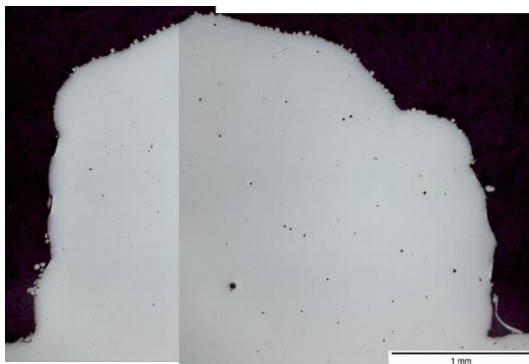


300-550-0-A
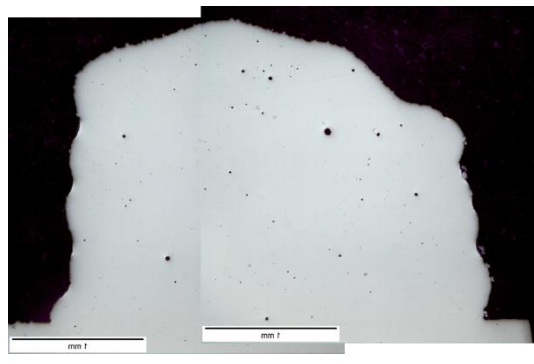


300-550-0-B
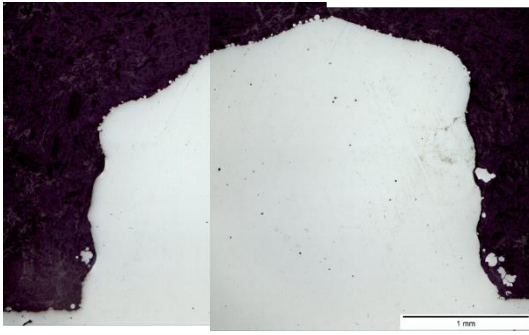
300-550-180-A
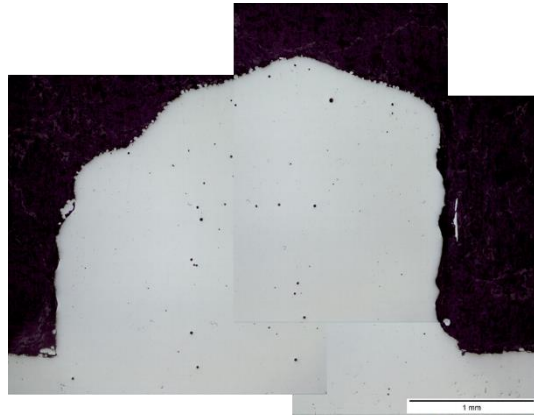


300-550-180-B
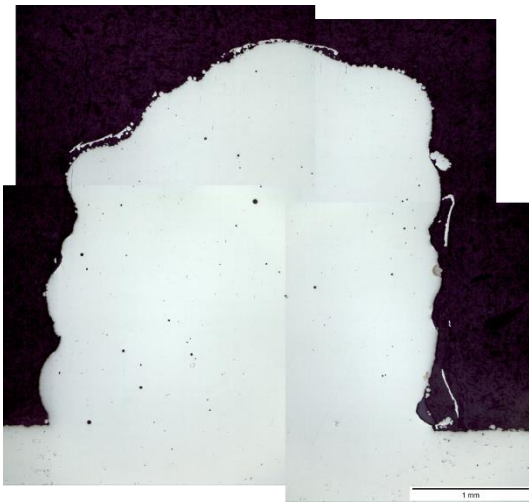


400-450-0-A
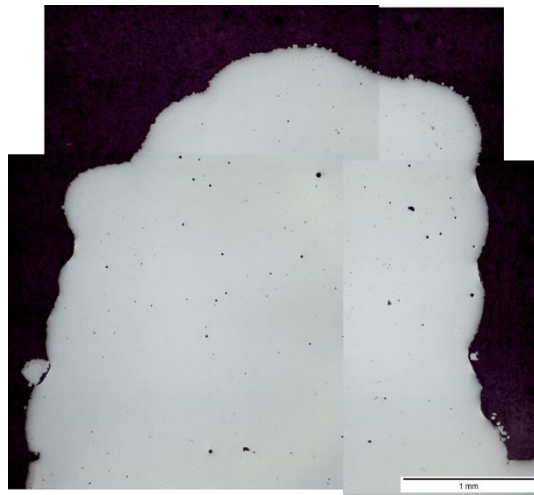


400-450-0-B
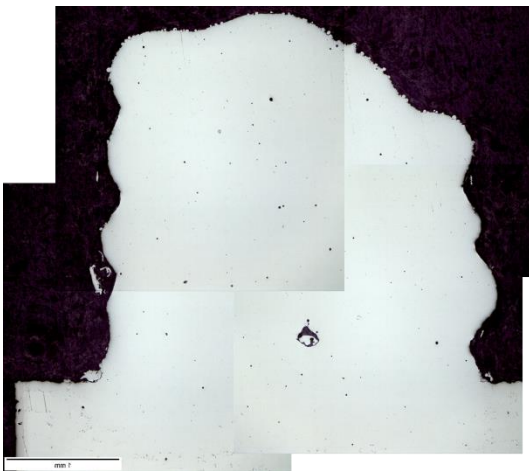


400-450-180-A
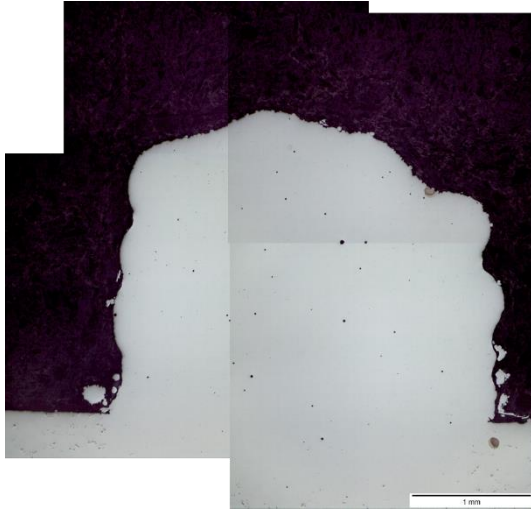


400-450-180-B
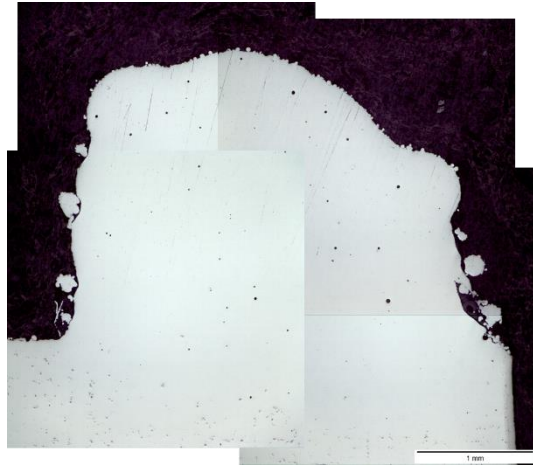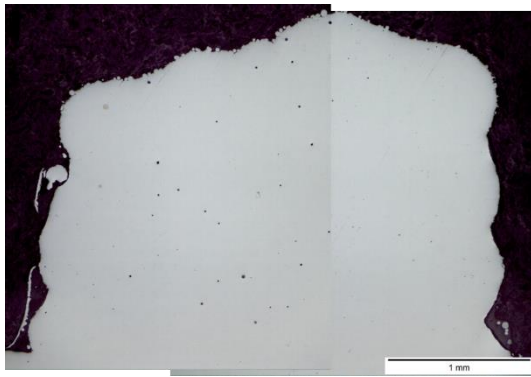
400-550-0-A



400-550-0-B
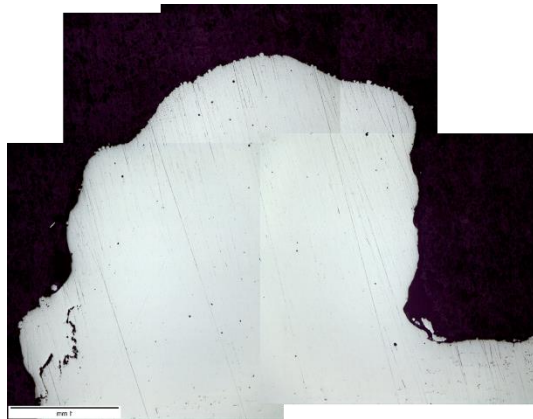


400-550-180-A



400-550-180-B

# APPENDIX VIII

Microstructure of LP-DED samples
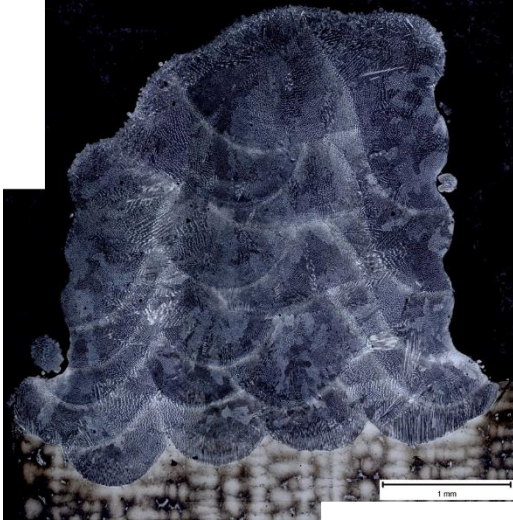
300-450-0-A

300-450-180-A
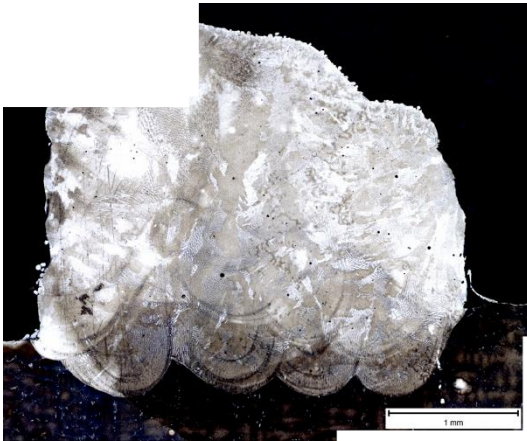
300-550-0-A

300-550-180-A
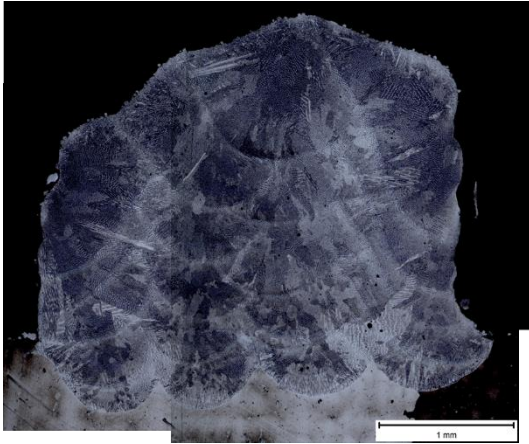
300-550-180-B



400-450-0-B



400-450-180-A



400-450-180-B
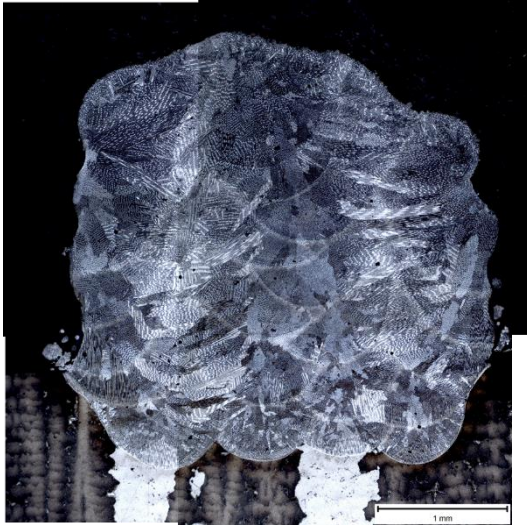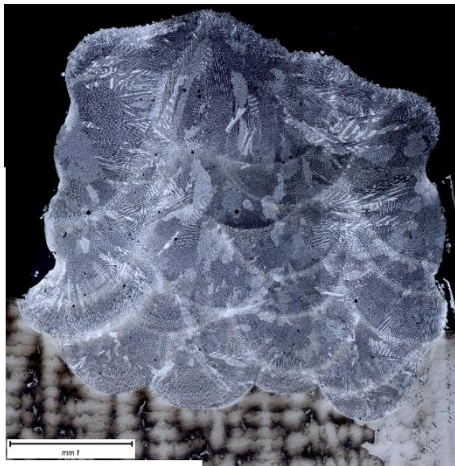
400-550-0-A



400-550-0-B



400-550-180-A
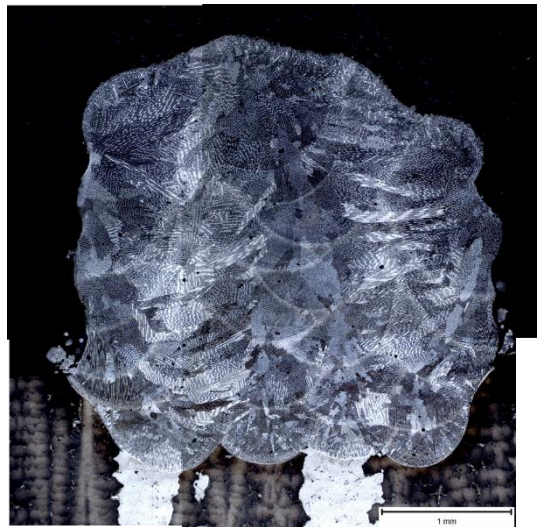


400-550-0-A

# APPENDIX IX

Top view of single bead using L-PBF
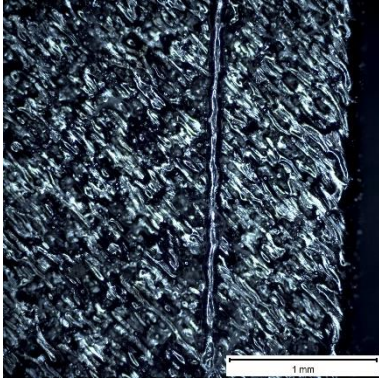


A) Single track 1
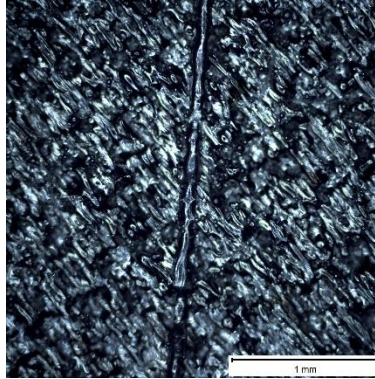


B) Single track 2
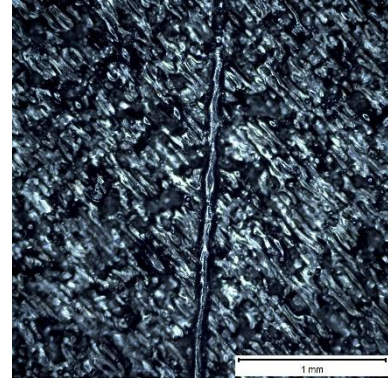


C) Single track 3
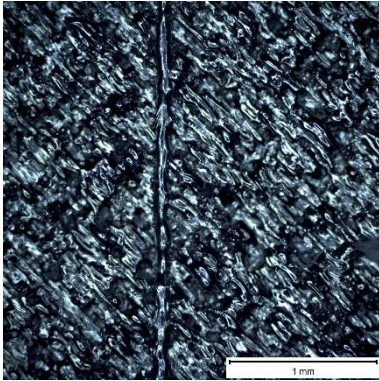


D) Single track 4
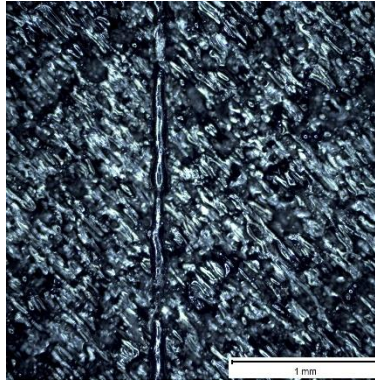


E) Single track 5
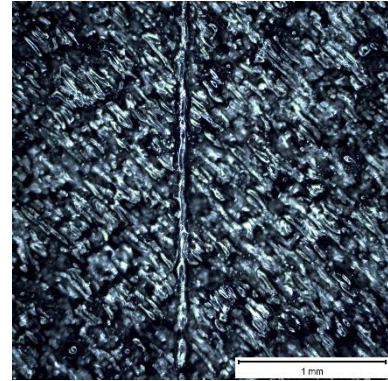


F) Single track 6
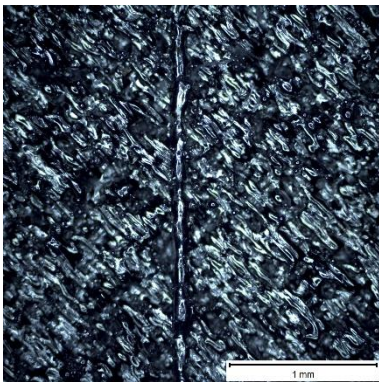


G) Single track 7
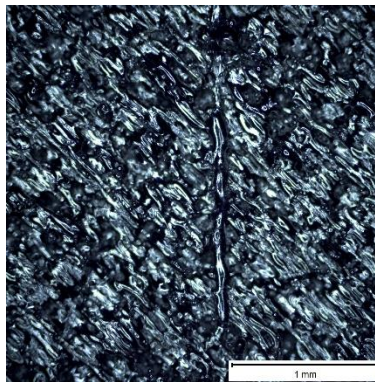


H) Single track 8
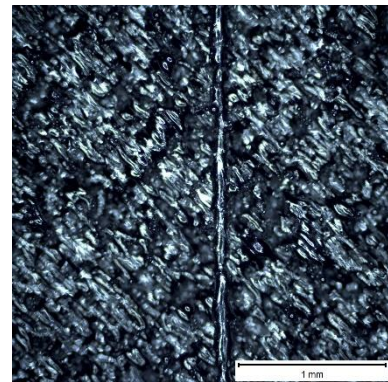


I) Single track 9
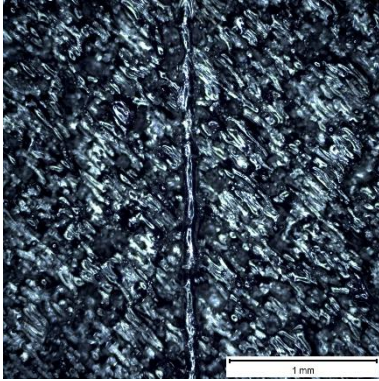
J) Single track 10
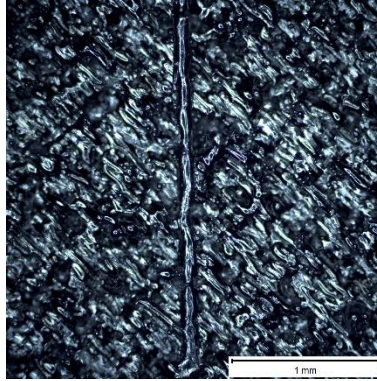

K) Single track 11
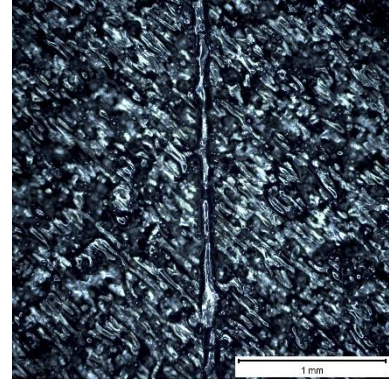

L) Single track 12
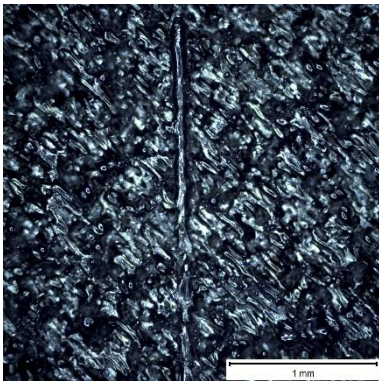

M) Single track 13
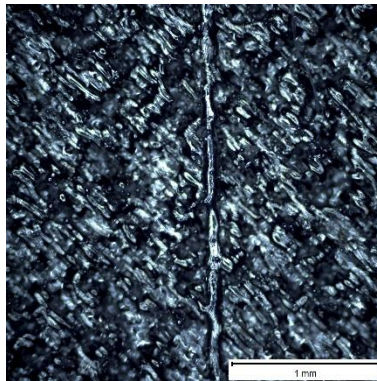

N) Single track 14
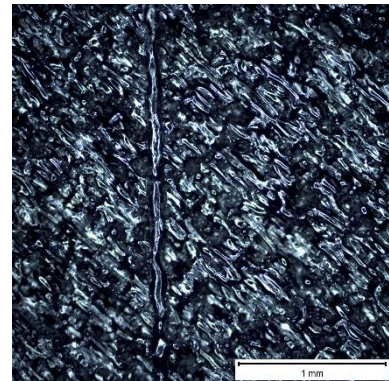

O) Single track 15
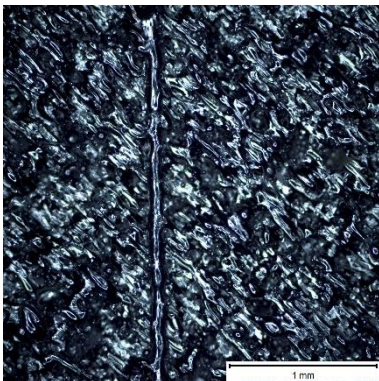

P) Single track 16
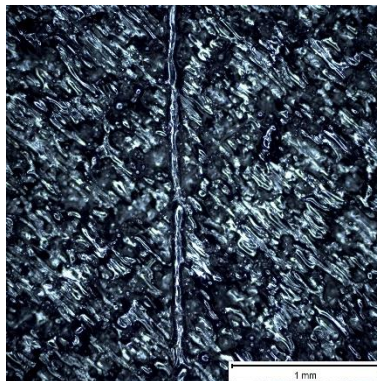

Q) Single track 17
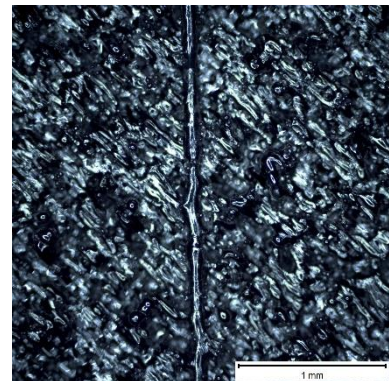

R) Single track 18
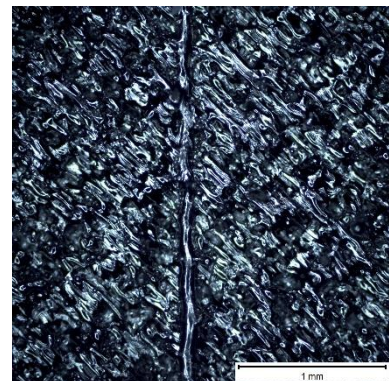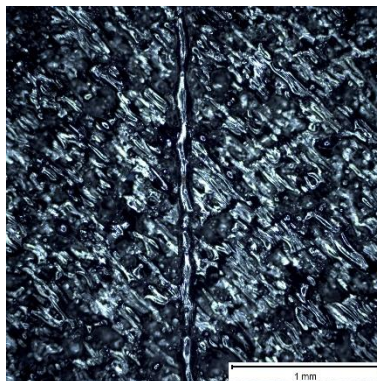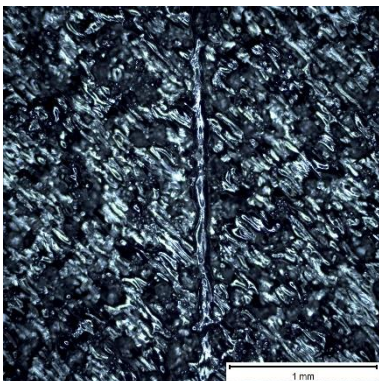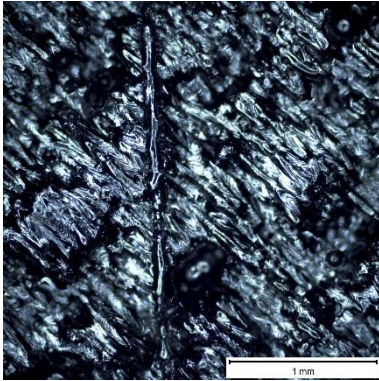
S) Single track 19          T) Single track 20          U) Single track 21
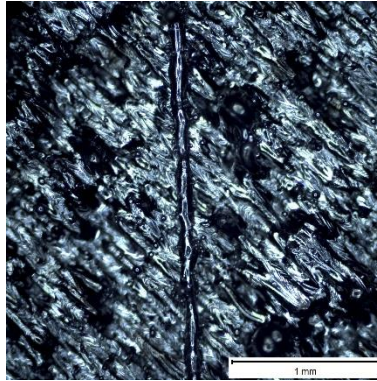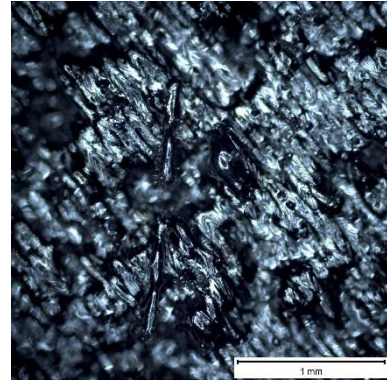


V) Single track 22          W) Single track 23          X) Single track 24

# APPENDIX X

Top view of layer of three beads using L-PBF process
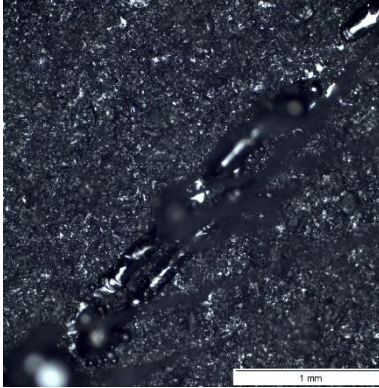


A) 50W-450 mm/s
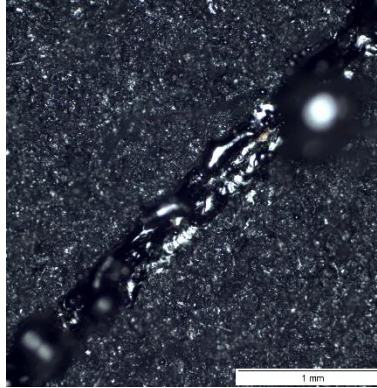
B) 50W-500 mm/s
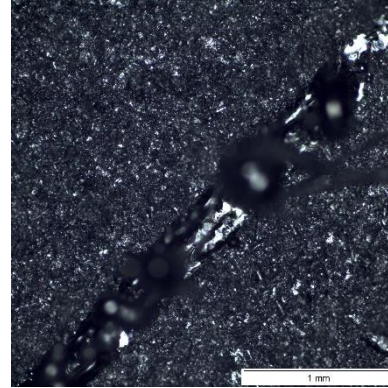
C) 50W-550 mm/s
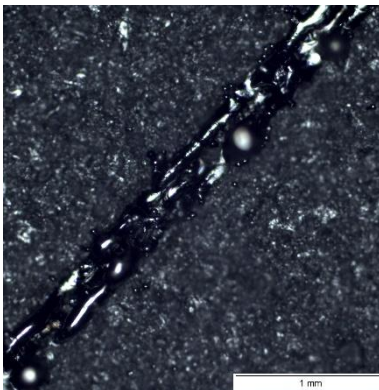
D) 50W-600 mm/s
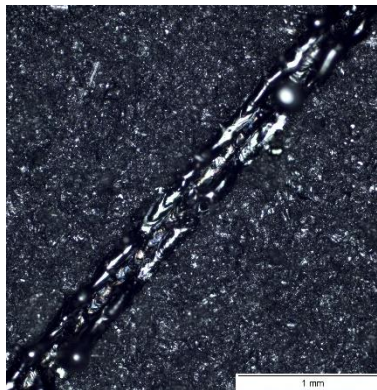
E) 50W-650 mm/s
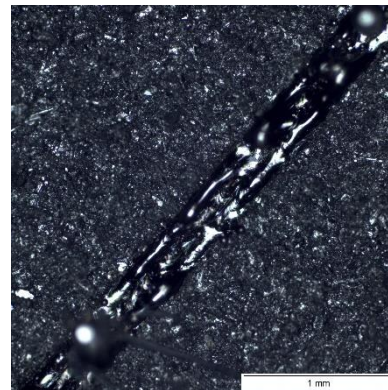
F) 50W-700 mm/s
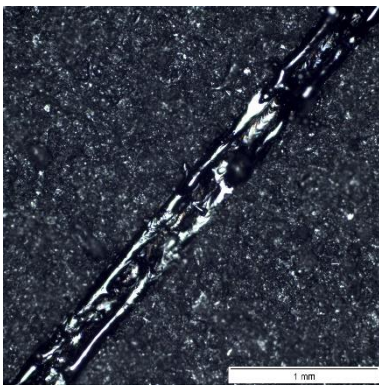
G) 50W-750 mm/s
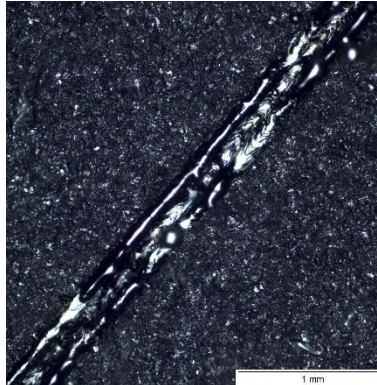
H) 50W-800 mm/s
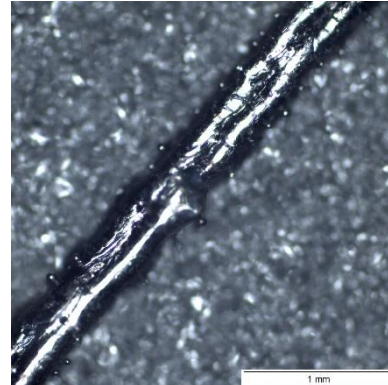
I) 90W-450 mm/s
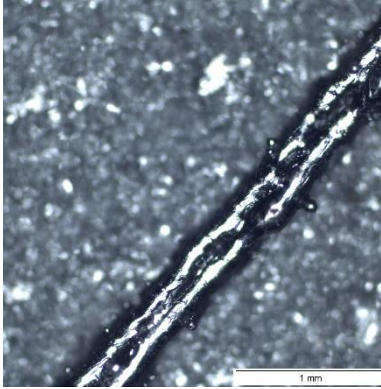
J) 90W-500 mm/s
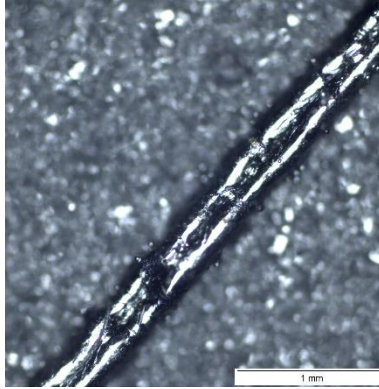


K) 90W-550 mm/s
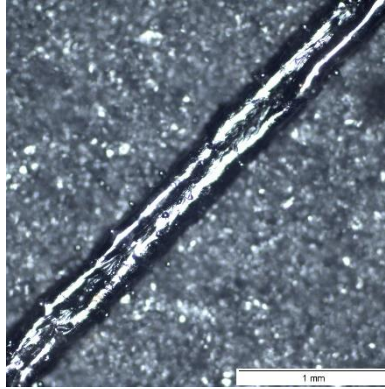


L) 90W-650 mm/s
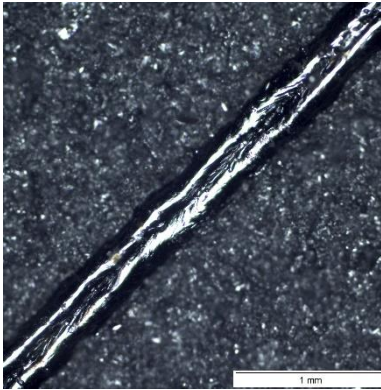


M) 90W-700 mm/s
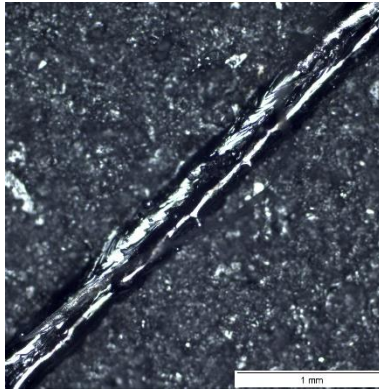


N) 90W-750 mm/s
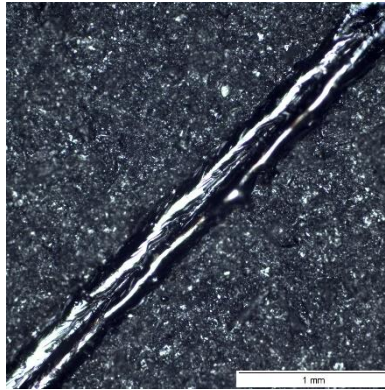


O) 90W-800 mm/s
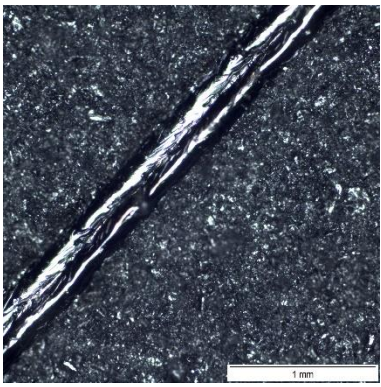


P) 90W-850 mm/s
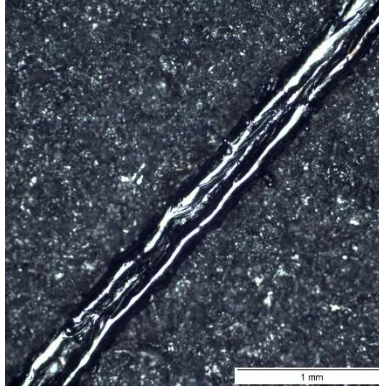


Q) 90W-900 mm/s

# APPENDIX XI

Cross section layer of 3 ST L-PBF
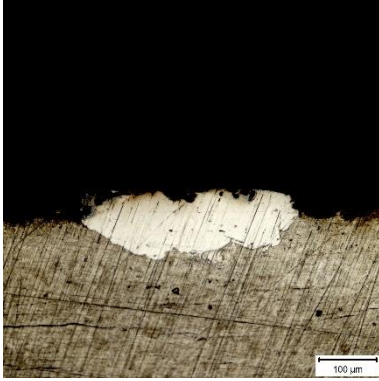


A) 90W-450 mm/s
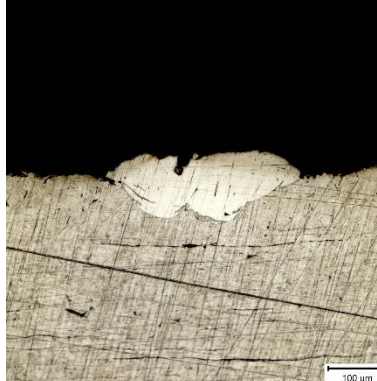


B) 90W-500 mm/s
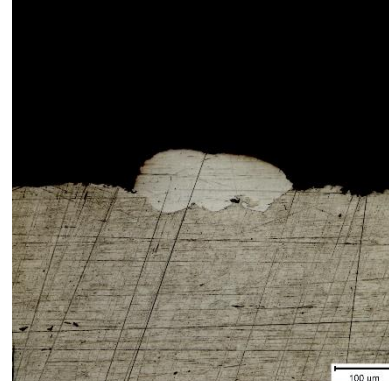


C) 90W-400 mm/s



D) 90W-700 mm/s
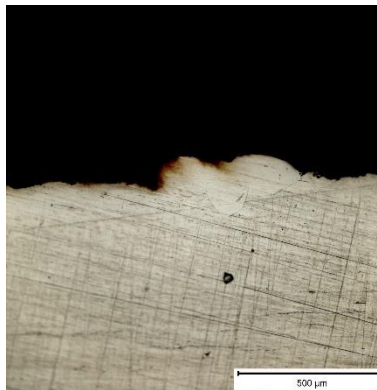


E) 90W-750 mm/s



F) 90W-800 mm/s
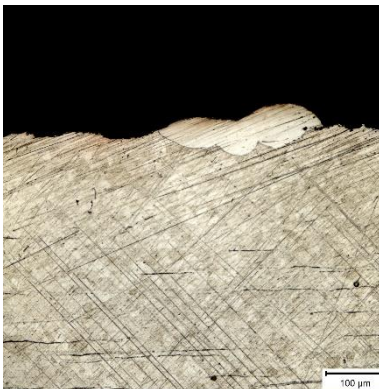


G) 90W-850 mm/s
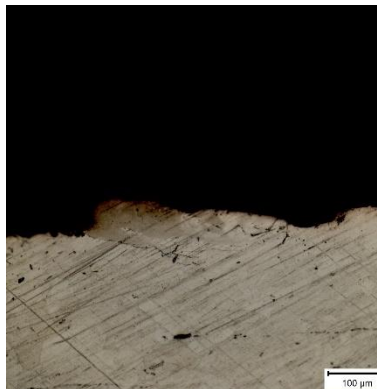


H) 90W-900 mm/s

# APPENDIX XII

Cubes to measure porosity. L-PBF
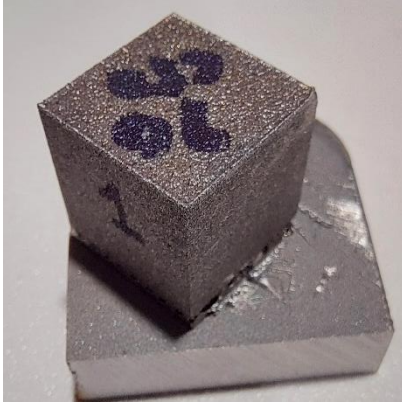


A) 90 W - 650 mm/s
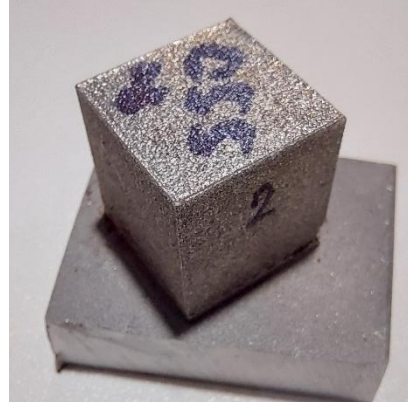


B) 90 W - 550 mm/s



C) 90W  - 800 mm/s
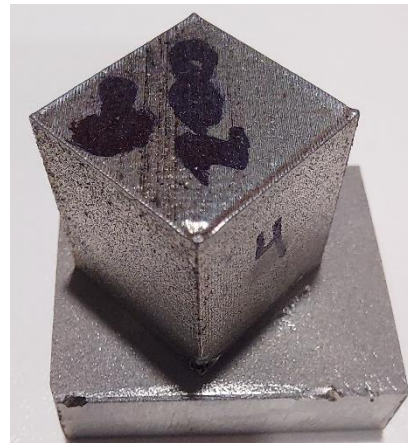


D) 80 W – 200 mm/s
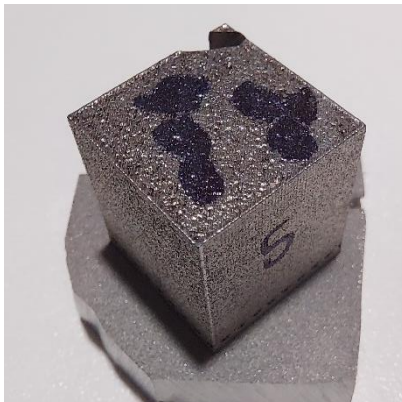


E) 80 W – 400 mm/s



F) 60 W – 800 mm/s
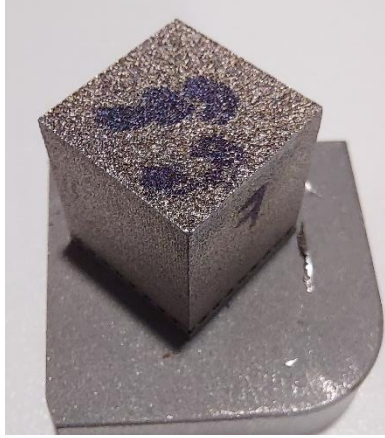
A) 60 W – 600 mm/s
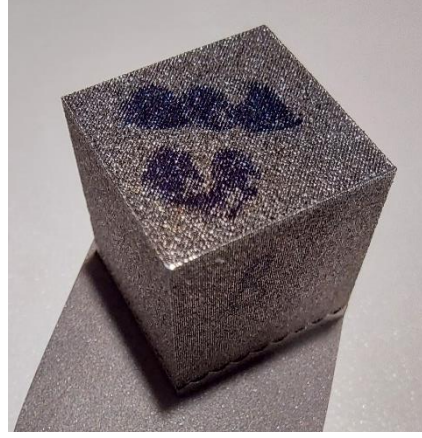


B) 50 W – 200 mm/s
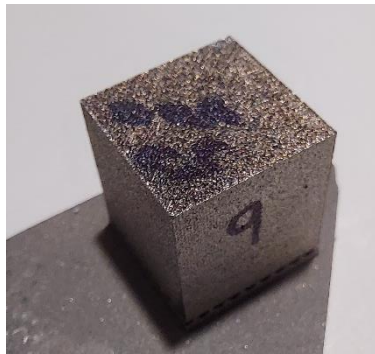


C) 50 W – 300 mm/s
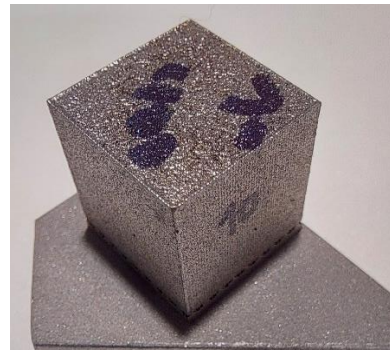


D) 70 W – 450 mm/s

# APPENDIX XIII

Cross-section of L-PBF samples at 12.5x
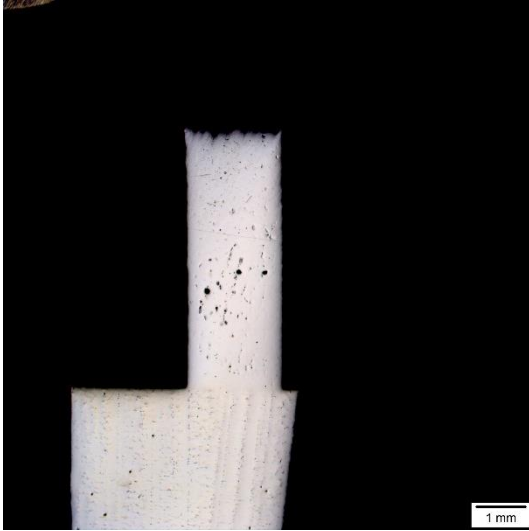


A)  50-200-0-A
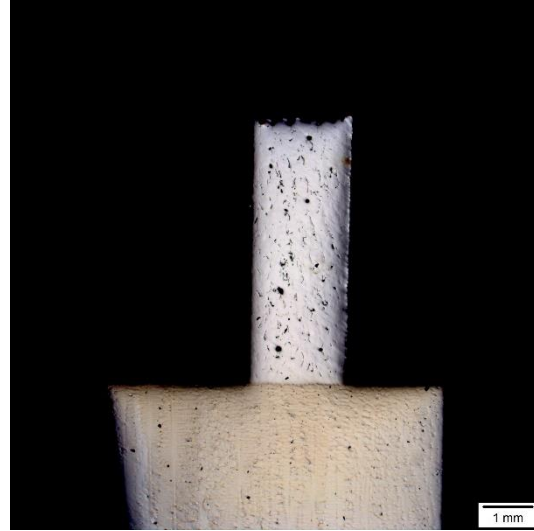


B) 50-200-0-B
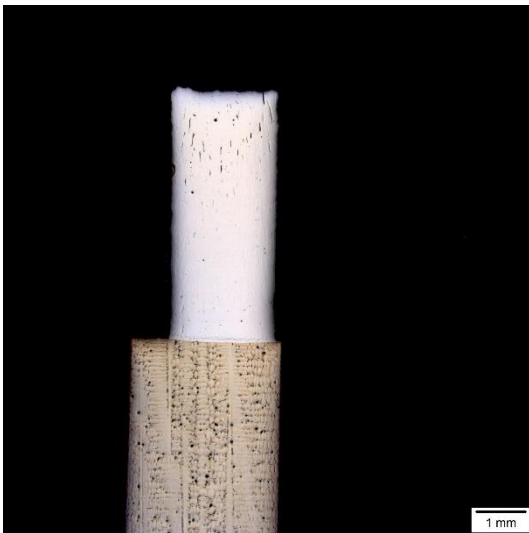


C) 50-200-90-A
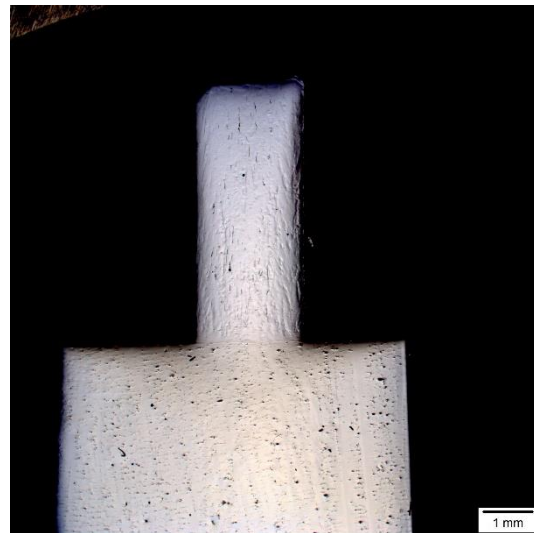


D) 50-200-90-B
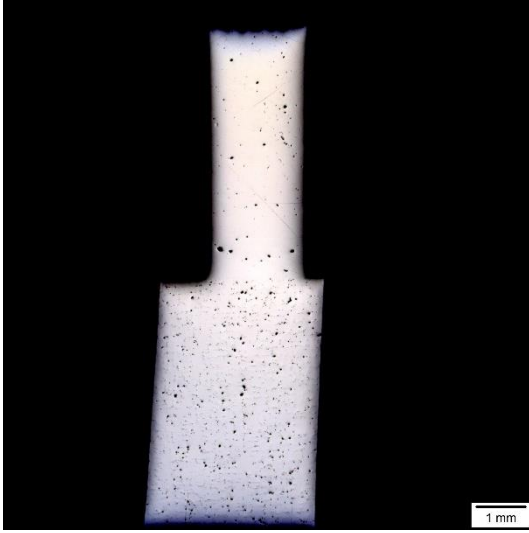
E)  50-400-0-A
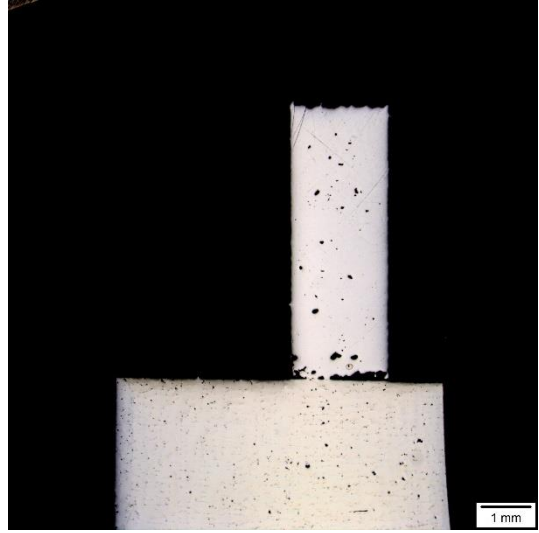


F)  50-400-0-B
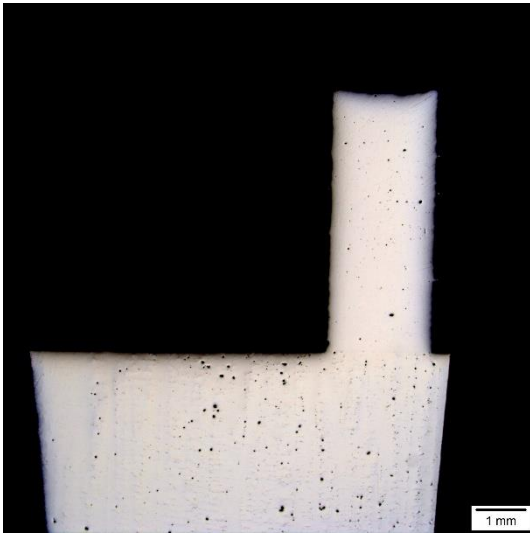


G)  50-400-90-A
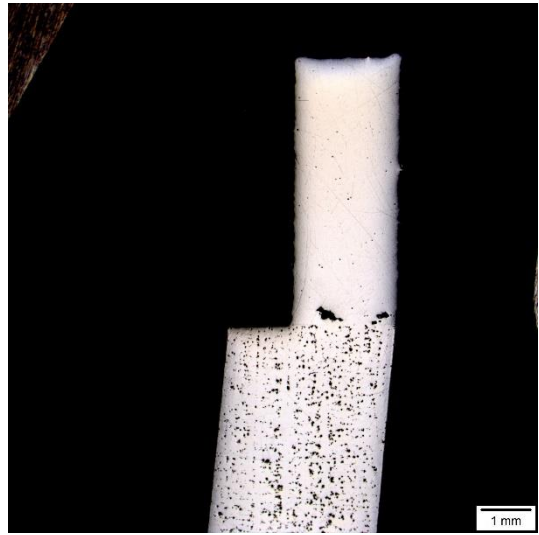


H)  50-400-90-B
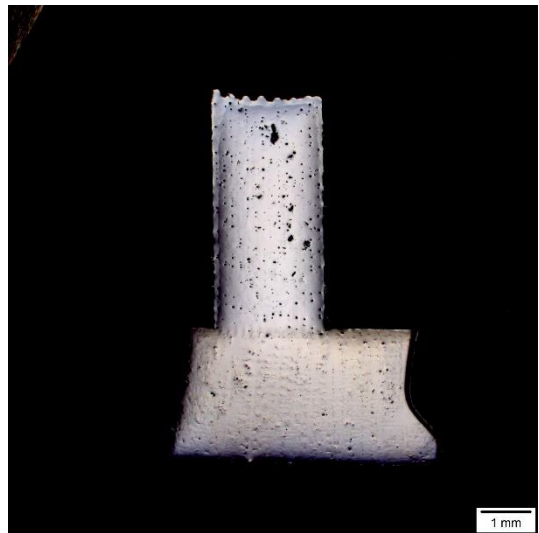
I)  80-200-0-A
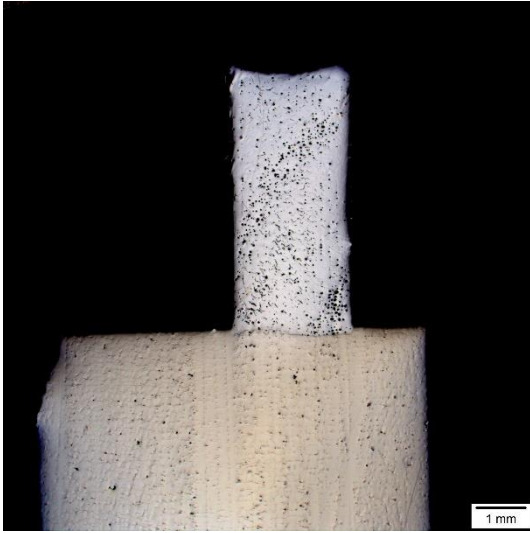
J)  80-200-0-B
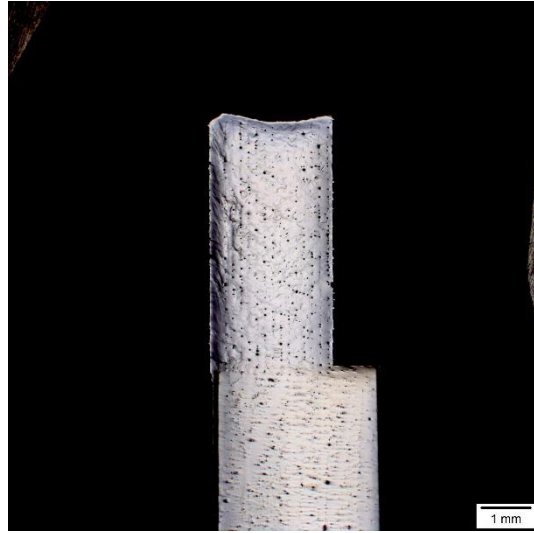
K)  80-200-90-A
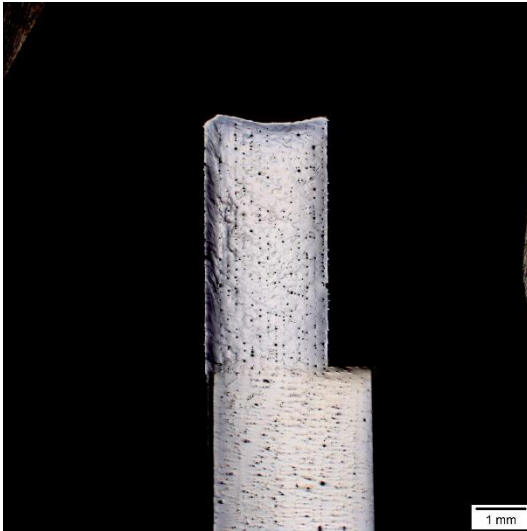
L)  80-200-90-B
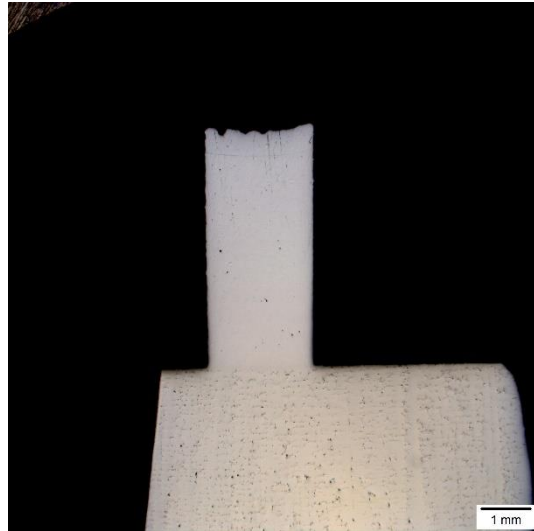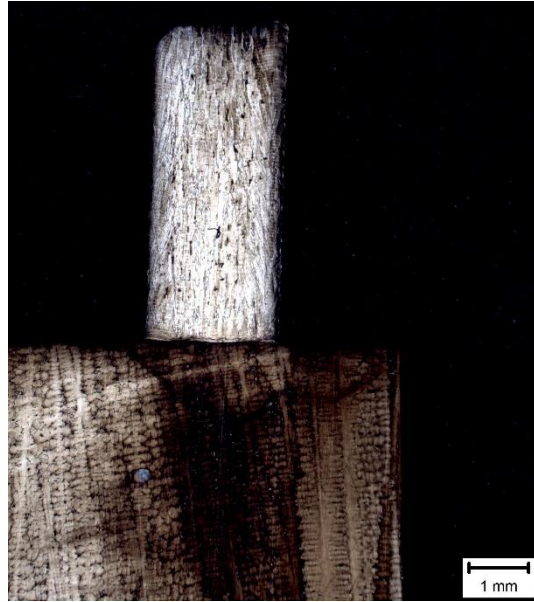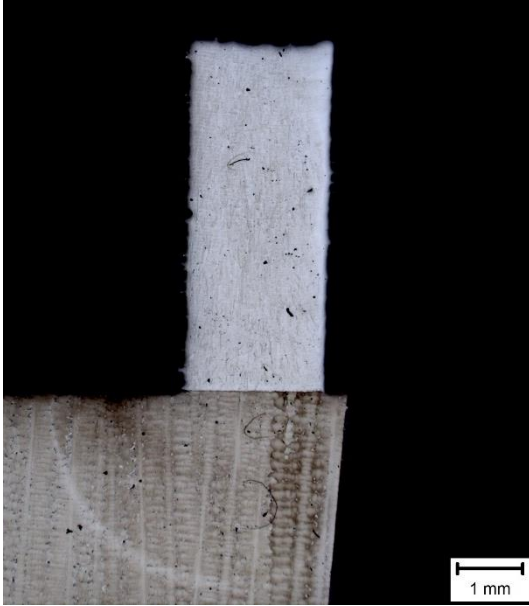
M)  80-400-0-A

N)  80-400-0-B
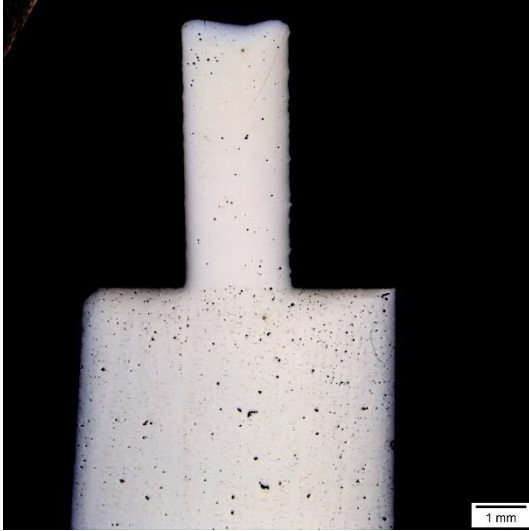
P) 80-400-90-A
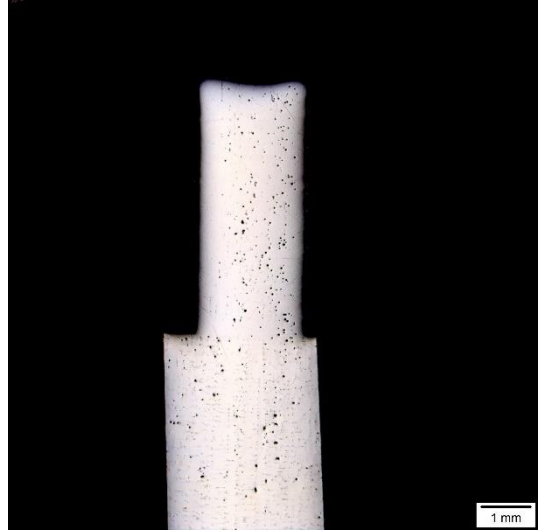


Q) 80-400-90-B

# APPENDIX XIV

Etched cross section of L-PBF samples at 12.5 X
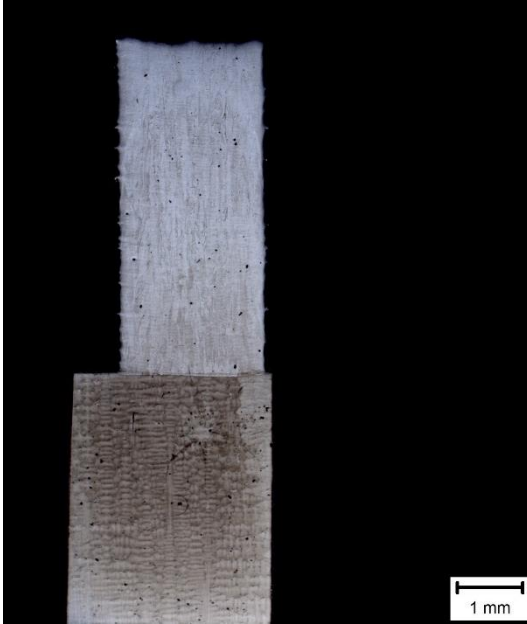


A) 50-200-90-A



B) 50-200-90-B



C) 50-200-0-A
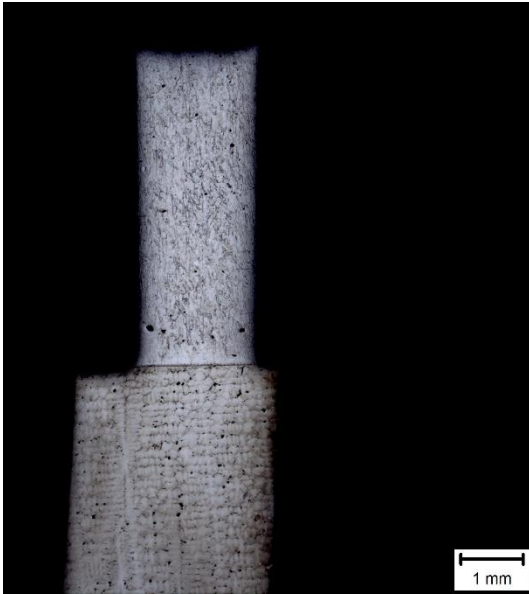


D) 50-400-0-B

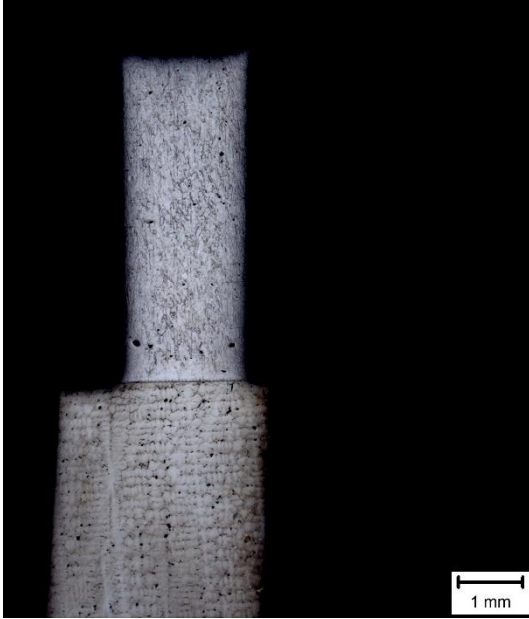E) 50-400-90-A



F) 50-400-90-B



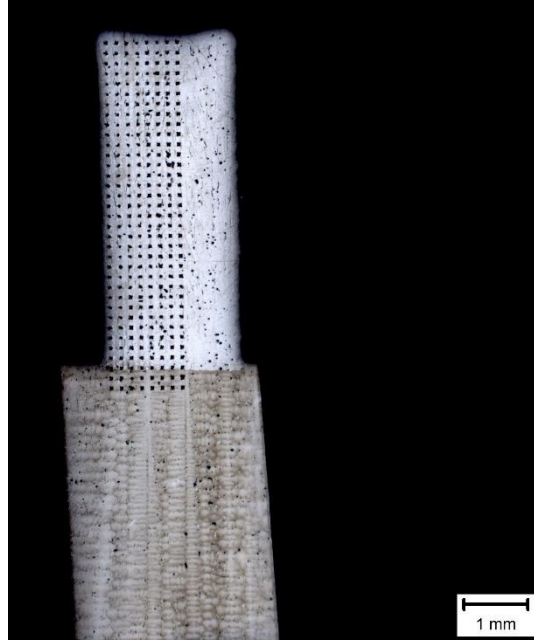G) 80-400-0-A



H) 80-400-0-B

I)   80-400-90-A                              J)   80-400-90-B

Etched cross section  of L-PBF samples at 50 X

# APPENDIX XV

Microstructure of L-PBF samples at 50x



A)  50-200-0-A



B)  50-200-90-A

C) 50-400-90-A

D) 80-400-0-A



E)  80-400-0-B